THESIS ON NATURAL AND EXACT SCIENCES B129

Photoelastic Tomography in Linear and Non-linear Approximation

ANDREI ERRAPART

TUT
PRESS

TALLINN UNIVERSITY OF TECHNOLOGY
Faculty of Sciences
Institute of Cybernetics, Laboratory of Photoelasticity

This dissertation was accepted for the defense of the degree of Doctor of Philosophy on Natural and Exact Sciences on 23th of April 2012.

Supervisor: Hillar Aben, DSc, Head, Laboratory of Photoelasticity, Institute of Cybernetics at Tallinn University of Technology

Opponents: Prof. Emmanuel Gdoutos, Corr. Member of the Academy of Athens, School of Engineering, Democritus University of Thrace, Greece

Dr. Jonathan Williams, Senior Technologist, NSG Group, United Kingdom

Defense of the thesis: 25th of May, 2012.

Declaration: Hereby I declare that this doctoral thesis, my original investigation and achievement, submitted for the doctoral degree at Tallinn University of Technology has not been submitted for any academic degree.

Andrei Errapart

ISSN 1406-4723
ISBN 978-9949-23-275-8 (publication)
ISBN 978-9949-23-276-5 (PDF)

LOODUS- JA TÄPPISTEADUSED B129

Fotoelastsustomograafia lineaarses ja mittelineaarses lähenduses

ANDREI ERRAPART

TTÜ
KIRJASTUS

Contents

Introduction

Development of non-destructive methods for the measurement of 3D stress fields is one of the ambitions of experimental mechanics. From all of the materials available to a man, control and measurement of internal stresses is most important in glass. This is because glass is so sharp when fractured, so dependent on internal stresses for strength, yet, so widely used one has to literally close his or her eyes to not see glass. The task is made infinitely simpler by a property of glass, photoelasticity, which in effect is artificial birefringence, proportional to the difference of principal stresses on the path of a light ray. This magnificient property permits quick and effective visualization of stresses in glass or in any other photoelastic material by observing the object in the simplest polariscope - a pair of crossed polaroids. However, the problem of complete determination of internal stress fields from the visual observations, either by eye or by camera, is in essence an ill-posed inverse problem, because the relationship between the stresses and the visualized interference fringes is a nonlinear one, and, therefore a difficult one to be solved.

The aim of this thesis is to further develop the established techniques of photoelastic tomography. The technology for analysis of residual stresses in the general 3D specimens is proposed. It is shown that the Abel inversion can be applied for the determination of axial and shear stress components of axisymmetric stress fields. The equations for determining radial and circumferential stress components in axisymmetric specimens are analysed for stability and new numerical algorithms for stress calculation are proposed. There are specimens for which linear approximation of integrated photoelasticity cannot be used; for stress analysis in those specimens the inverse problem of photoelasticity is solved with a differential evolution algorithm (a genetic algorithm).

Some of the results of this thesis have been implemented in the glass stress measurement technology marketed by GlasStress Ltd.

The thesis is organized as follows.

Chapter 1 covers the linear approximation in photoelastic tomography. Overview of the reconstruction methods is given, both for the general case of 3D stress fields and for the case of axisymmetric stress field; the latter including Abel inversion. Determination of radial and circumferential stress components in the case of axisymmetric stress field is covered in detail. Examples are given for all the cases - general 3D stress distribution, axisymmetric stress distribution in the case of residual stresses and in the case of external loads.

Chapter 2 extends the working range of photoelastic tomography of axisymmetric stress fields into the non-linear region by using an evolutionary algorithm. A practical example is shown.

The present thesis is based on the following papers:

I Aben, H., Ainola, L., Errapart, A. Application of the Abel inversion in case of a tensor field. *Inverse Problems in Science and Engineering*, 2010, **18**(2), 241-249.

II Errapart, A. On the technology of photoelastic tomography. *Experimental Techniques*, 2008, **32**(1), 31 - 35.

III Errapart, A. Determination of all stress components of axisymmetric stress state in photoelastic tomography. In *Advances in Experimental Mechanics VIII : Selected, peer-reviewed papers of the 8th International Conference on Advances in Experimental Mechanics: Integrating Simulation and Experimentation for Validation, (BSSM 2011), Sept. 7-9 2011, Edinburgh, Scotland* (Burguete R. L. et al., eds.). Trans Tech Publications, Durnten-Zuerich, 2011, 434-439.

IV Aben, H., Errapart, A. A non-linear algorithm of photoelastic tomography for the axisymmetric problem. *Experimental Mechanics*, 2007, **47**(6), 821 - 830.

Summary of authors contributions in basic publications

I Realization of the algorithm.

II Development of the measurement technology of photoelastic tomography.

III Mathematical analysis of the problem, development and implementation of the algorithm and experimental work.

IV Development and implementation of the algorithm and experimental verification of non-linear photoelastic tomography.

List of conference presentations

1. Aben, H. (speaker), A. Errapart, J. Sanko, and Anton J. A Non-linear Algorithm of Photoelastic Tomography for the Axisymmetric Problem. *Photomechanics 2006: International Conference on Full-field Measurement Techniques and their Applications in Experimental Solid Mechanics*. Clermont-Ferrand, France, 2006.
2. Aben H. (speaker), Anton J., Errapart A. Modern Photoelasticity for Residual Stress Measurement in Glass. *13th International Conference on Experimental Mechanics*, Alexandroupolis, Greece, July 1-6, 2007.
3. Errapart, A., Oldenbourg, R., Kurkjian, R., Aben, H. (speaker). Application of integrated photoelasticity for the measurement of residual stress in locally plastically deformed glass. *Photomechanics 2008 - International conference on full-field measurement techniques and their applications in experimental solid mechanics*, Loughborough, UK, 7th - 9th July 2008.

4. Aben, H. (speaker), Ainola, L., Errapart, A. Photoelastic tomography as hybrid mechanics. *Symposium on Recent Advances in Mechanics*, Athens, Greece, 17-19 September, 2009.
5. Aben H. (speaker), Errapart A., Ainola L. Photoelastic tomography with linear and non-linear algorithms. *2010 SEM Annual Conference & Exposition on Experimental and Applied Mechanics*, Indianapolis, USA.
6. Errapart A. (speaker) Photoelastic residual stress measurement in non-axisymmetric glass containers. *14th International Conference on Experimental Mechanics*, Poitier, France, July 4 - 9, 2010.
7. Errapart, A. (speaker), Aben, H., Ainola, L., Anton, J. Photoelastic tomography for the measurement of thermal and residual stresses in glass. *9th International Congress on Thermal Stresses 2011 with Naotake Noda Symposium*, Budapest, Hungary, June 5-9, 2011.
8. Errapart, A. (speaker) Determination of all stress components of axisymmetric stress state in photoelastic tomography. *8th International Conference on Advances in Experimental Mechanics: Integrating Simulation and Experimentation for Validation (BSSM 2011)*, Edinburgh, Scotland, Sept. 7-9 2011
9. Errapart, A. (speaker), Aben, H. Photoelastic tomography in the axisymmetric and non-axisymmetric case. *FVR 2011 : Forum on recent developments in volume reconstruction techniques applied to 3D fluid and solid mechanics*, Poitiers, France, November 29th - December 1st, 2011.

Acknowledgements

I express my gratitude to my supervisor DSc. Hillar Aben. Without his support at key moments this thesis would have never materialized. I am truly thankful for his excellent example of a scientist.

My colleague Johan Anton, who has a wonderful knack for mechanics and with whom I have had quite a few fruitful discussions, deserves many thanks. Most of the topics were on the practical matters regarding construction of the polariscopes, however, a fair share were theoretical ones, too.

Professor Chuck Kurkjian at the Rutgers University, USA, initiated the analysis of stresses in the fibers indented by spheres. The data was kindly provided by prof. Satoshi Yoshida at the Shiga Prefecture University, Japan, and prof. Rudolf Oldenbourg at the Marine Biological Laboratory, USA. This data enabled the work on the algorithms for determining the radial and circumferential stress components in the case of stresses due to external loads.

I am thankful to my relatives for their support.

Financial support from the Estonian Science Foundation is acknowledged.

1 Photoelastic tomography in linear approximation

1.1 Classical tomography

Tomography is a powerful method for the analysis of the internal structure of different objects, from human bodies to parts of atomic reactors [18,20]. In tomography, some radiation (x rays, protons, acoustic waves, light, etc.) is passed through a section of the object in many directions, and properties of the radiation after it has passed the object (intensity, phase, deflection, etc.) are measured on many rays (Fig. 1). Experimental data $g(l,\beta)$ for different values of the angle β are called projections.

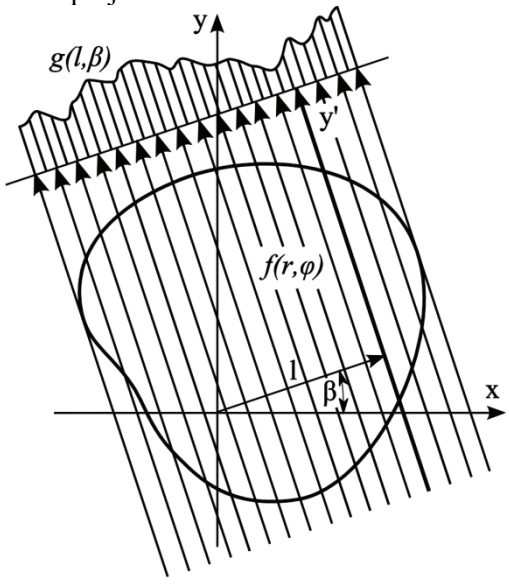

Fig. 1: Tomographic measurements.

If $f(r,\varphi)$ is the function, which determines distribution of certain parameter of the field, experimental data for a real pair l,θ can be expressed by the Radon transform of the field

$$g(l,\beta)=\int_{-\infty}^{+\infty} f(r,\varphi)\mathrm{d}y'. \tag{1}$$

When projections for many values of β have been recorded, the function $f(r,\varphi)$ is determined from the Radon inversion

$$f(r,\varphi)=\frac{1}{2\pi^2}\int_0^{\pi}\mathrm{d}\beta\int_{-E}^{E}\frac{\partial g(l,\beta)}{\partial l}\frac{\mathrm{d}l}{r\cos(\beta-\varphi)-l}. \tag{2}$$

Many numerical algorithms for solving Eq. (2) have been elaborated[18,20].

The question arises, is it possible to determine tomographically also stress fields in 3D objects. This problem is not trivial due to the following reason. Classical tomography considers only determination of scalar fields, i.e., every point of the field is characterized by a single number (the coefficient of attenuation of the X-rays, acoustical or optical index of refraction, etc.). Since stress is a tensor, in stress field tomography every point of the field is characterized by six numbers. Thus the problem is much more complicated in principle. Let us mention that while a huge number of publications is devoted to scalar field tomography, there is only a single book, written by Sharafutdinov[24], devoted to mathematical problems of the tensor field tomography.

1.2 Photoelastic tomography in linear approximation

It has been shown[6] that in linear approximation an inhomogeneous birefringent medium can be considered optically equivalent to a birefringent plate. It is possible to measure the parameter of the isoclinic φ and optical retardation Δ on every light ray that passes the specimen with conventional polariscopes. In practice, in order to avoid refraction of the light, the test object is placed in an immersion tank with matching immersion liquid (Fig. 2).

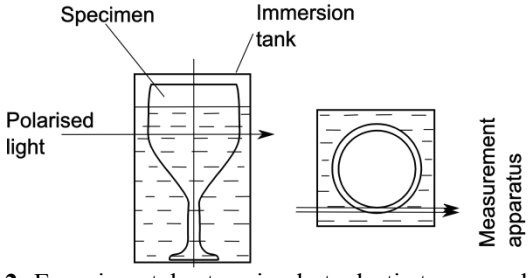

Fig. 2: Experimental set-up in photoelastic tomography.

Let us assume that in two parallel sections, the main section ($z = z_0$) and the auxiliary section ($z = z_0 + \Delta z$) of an arbitrary 3D specimen tomographic photoelastic measurements, rotating the specimen around the z axis, have been carried out and the integrals V_1 and V_2 have been measured for many azimuths β (Fig. 3) for light rays, parallel to y':

$$V_1 = \Delta \cos 2\varphi = C \int (\sigma_{x'} - \sigma_{z'}) dy' , \quad (3)$$

$$V_2 = \Delta \sin 2\varphi = 2C \int \tau_{x'z'} dy', \quad (4)$$

where Δ is optical retardation, φ is the parameter of the isoclinic and C is photoelastic constant. In the auxiliary section, these integrals are denoted as V_1'

and V_2'. Location of the light ray y' is determined by the value of its x' coordinate l and the angle β.

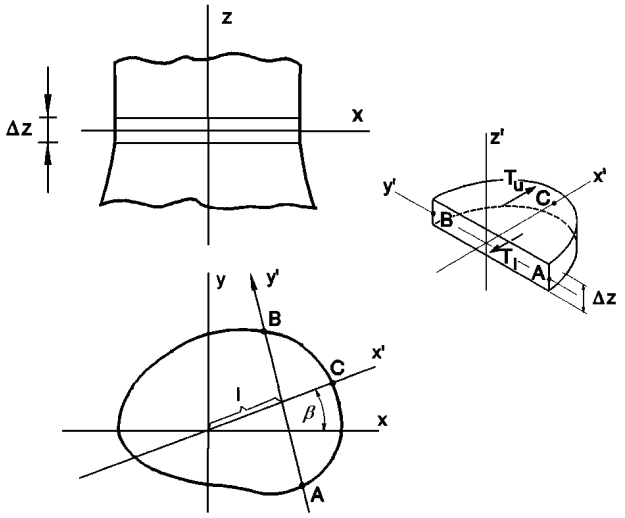

Fig. 3: Tomographic measurement scheme.

Equations (3) and (4) are valid if birefringence is weak (optical retardation is less than about 1/3 of the wavelength) or the rotation of the principal stress axes is small (less than about $\pi/6$)[6]. If no rotation of the principal stress axes is present, Eqs. (3) and (4) are valid for arbitrary birefringence.

Sharafutdinov suggested the following method for the measurement of the distribution of the axial stress σ_z [24,25]. Besides the measurement of the functions V_1 and V_2, the value of the axial stress σ_z is to be measured on the boundary of the cross section. Applying to the functions V_1 and V_2 the transverse ray transform [24], the σ_z field is determined from the boundary value problem for a Poisson equation. Sharafutdinov has shown that the solution of this tomographic problem is unique and that only the distribution of σ_z can be determined in this way [24,25].

The drawback of this method is that, in addition to tomographic photoelastic measurements, the boundary values of σ_z must be measured. That is possible only in the case when the boundary of the cross section is described by a convex curve. Besides, the transverse ray transform is rather complicated. The tomographic algorithm of Sharafutdinov has not been applied in practice, although it is important from the point of view of the theory of photoelastic tomography.

Another algorithm of the photoelastic tomography in linear approximation is the following. Let us assume that photoelastic tomographic measurements have been carried out in two parallel sections, a distance Δz apart from each other,

rotating the specimen around the z axis (Fig. 3). The values of the functions V_1 and V_2 in the auxiliary section we denote by V_1' and V_2'. Considering the equilibrium of the three-dimensional segment ABC in the direction of the x' axis (Fig. 3), we may write

$$\Delta z \int_A^B \sigma_{x'} \mathrm{d}y' = T_u - T_l, \tag{5}$$

where T_u and T_l are the shear forces on the upper and lower surfaces of the segment, respectively:

$$T_u = \frac{1}{2C} \int_l^C V_2' \mathrm{d}x', \quad T_l = \frac{1}{2C} \int_l^C V_2 \mathrm{d}x'. \tag{6}$$

Taking into consideration relationships (5) and (6), Eq. (3) reveals

$$\int_A^B \sigma_z \mathrm{d}y' = \frac{2}{2C\Delta z} \left(\int_l^C V_2' \mathrm{d}x' - \int_l^C V_2 \mathrm{d}x' \right) - \frac{V_1}{C}. \tag{7}$$

Since tomographic photoelastic measurement data can be obtained for all the light rays y' (for many values of l and β), Eq. (7) expresses the Radon transform of the field of the stress σ_z. Thus we have reduced a problem of tensor field tomography to a problem of scalar field tomography for a single stress component σ_z. The field of σ_z can be determined using any of the well-known Radon inversion techniques[18,20]. Rotating the specimen by tomographic measurements around the axes x and y, the fields of σ_z and σ_y can also been determined.

In the case of an axisymmetric stress field, the problem is reduced to a problem of one-dimensional tomography [12]. In this case the distribution of σ_z is determined from the Eq. (7) with Abel inversion [13]. In linear approximation, photoelastic tomography has been used for residual stress measurement in axisymmetric glass articles [2,5,15].

Let us mention that we consider photoelastic tomography, which is based on the measurement on every light ray of the parameter of the isoclinic φ and *relative optical retardation* Δ. Photoelastic tomography with interferometric measurement of *absolute optical retardations* has not lead to positive results [23]. By formulating the problem of photoelastic tomography it is important to distinguish between these two formulations. Otherwise one may reach erroneous results[3].

1.3 Reconstruction of the axial component in the general 3D case

Since the Radon transform of the axial stress σ_z is determined through the measurement data according to Eq. (7), any method of Radon inversion can be used to determine the field of σ_z. In this chapter, a method proposed by Cormack[11], in which the stress field is approximated with two-dimensional polynomials, is described.

The cross-section of a specimen is assumed to be located inside the circle of radius R (Fig. 4) and the stress field is expressed in polar coordinates as a Fourier series

$$\sigma_z(\rho,\varphi) = f_0(\rho) + \sum_{m=1}^{M} (f_m(\rho)\cos m\varphi + g_m(\rho)\sin m\varphi), \tag{8}$$

$$\rho = \frac{r}{R}, \tag{9}$$

where M is the number of terms. Higher value of M gives better approximation along the angular coordinate.

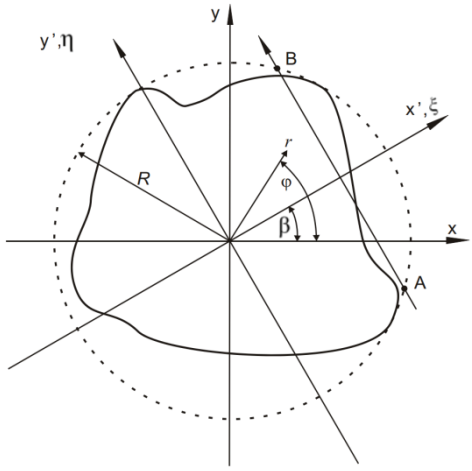

Fig. 4: Investigation of a section of an object.

The values of line integrals $I(\xi,\beta)$ are defined as

$$I(\xi,\beta) = \int_A^B \sigma_z \mathrm{d}y', \tag{10}$$

$$\xi = \frac{x'}{R}, \tag{11}$$

and can be experimentally determined from the right hand side of Eq. (7). When these line integrals are expressed as Fourier series,

$$\frac{I(\xi,\beta)}{R} = F_0(\xi) + \sum_{m=1}^{M} (F_m(\xi)\cos m\beta + G_m(\xi)\sin m\beta), \tag{12}$$

the Cormack transform reveals a relationship between $f_m(\rho)$ and $F_m(\xi)$,

$$F_m(\xi) = 2\int_{\xi}^{1} \frac{f_m(\rho)T_m(\xi/\rho)\rho \mathrm{d}\rho}{\sqrt{\rho^2+\xi^2}}, \tag{13}$$

where $T_M(\xi/\rho)$ are the Chebyshev polynomials of the first kind[19]. Similar relationship applies for $g_m(\rho)$ and $G_m(\xi)$.

When the functions $F_m(\xi)$ and $f_m(\rho)$ ($G_m(\xi)$ and $g_m(\rho)$) are orthogonal polynomials in the interval (0,1), Eq. (13) can be solved analytically. Cormack has used the following related orthogonal polynomials

$$f_m(\rho) = \sum_{l=0}^{L} a_m^l (m+2l+1) Z_p^l(\rho), \tag{14}$$

$$F_m(\xi) = 2\sum_{l=0}^{L} a_m^l U_{m+2l+1}(\xi). \tag{15}$$

where $Z_m^l(\rho)$ are first order Zernicke polynomials [9], $U_m(\xi)$ are Chebyshev polynomials of the second kind, a_m^l are coefficients and L is the number of terms. Higher value of L gives better approximation along the radial coordinate. The same can be written for the polynomials $G_m(\xi)$ and $g_m(\rho)$ (b_m^l are coefficients)

$$g_m(\rho) = \sum_{l=0}^{L} b_m^l (m+2l+1) Z_m^l(\rho), \tag{16}$$

$$G_m(\xi) = 2\sum_{l=0}^{L} b_m^l U_{m+2l+1}(\xi). \tag{17}$$

Determination of σ_z is divided into three steps:

1. Calculation of values of functions $F_m(\xi)$ and $G_m(\xi)$ from Eq. (12) at every point of measurement i ($i = 1 \ldots N$) by using the discrete Fourier transform; here N denotes the number of measurements on the radius.
2. Approximation of $F_m(\xi)$, $G_m(\xi)$ with polynomials (15), (17) and determination of the coefficients a_m^l, b_m^l using the least squares method.
3. Calculation of σ_z using Eq (8).

The Zernicke polynomial can be calculated using the formula

$$Z_m^l(\rho) = \sum_{s=0}^{l} \frac{(-1)^3 (m+2l-s)!\, r^{m+2l-2s}}{s!\,(m+l-1)!\,(l-s)!}. \tag{18}$$

The Chebyshev functions of the second kind are defined as

$$U_m(\xi) = \sin(m \arccos \xi). \tag{19}$$

1.4 Reconstruction of axial and shear components of an axisymmetric stress field

1.4.1 Abel inversion

The Abel transform of an axisymmetric function $f(r)$, assumed to be located inside the circle of radius R (Fig. 5), is a line integral along AB [44]

$$F(x) = 2\int_x^R \frac{f(r) r \mathrm{d}r}{\sqrt{r^2 - x^2}}. \tag{20}$$

The corresponding Abel inversion is

$$f(r) = -\frac{1}{\pi}\int_r^R \frac{\mathrm{d}F}{\mathrm{d}x} \frac{\mathrm{d}x}{\sqrt{x^2 - r^2}}. \tag{21}$$

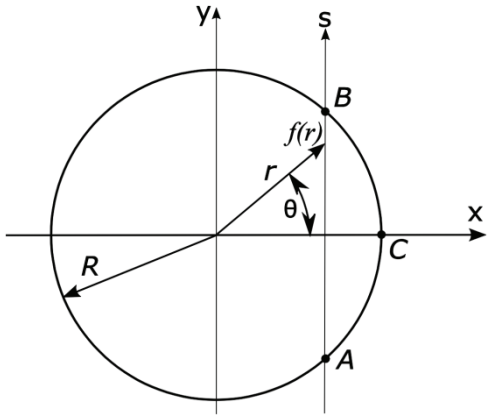

Fig. 5: Line integral of an axisymmetric function $\boldsymbol{f(r)}$.

Value of the line integral of the axial stress component σ_z along AB can be obtained from Eq. (7),

$$I(x) = \frac{2}{2C\Delta z}\left(\int_x^C V_2' \mathrm{d}x' - \int_x^C V_2 \mathrm{d}x'\right) - \frac{V_1}{C}. \tag{22}$$

From the values of $I(x)$ obtained from Eq. (22), distribution of the axial stress can be determined using the Abel inversion as

$$\sigma_z(r) = -\frac{1}{\pi}\int_r^R \frac{\mathrm{d}I(x)}{\mathrm{d}x}\frac{\mathrm{d}x}{\sqrt{x^2 - r^2}}. \tag{23}$$

The value V_2 in Eq. (4) can be written as a function of x, and, in terms of shear stress τ_{rz} as follows

$$V_2(x) = \Delta \sin 2\varphi = 2C\int_A^B \tau_{rz}\cos\theta\,\mathrm{d}y. \tag{24}$$

or

$$\frac{V_2(x)}{x} = 2C\int_A^B \tau_{rz}\mathrm{d}y. \tag{25}$$

From Eq. (25), distribution of the shear stress can be determined using the Abel inversion

$$\tau_{rz}(r) = -\frac{r}{2\pi C}\int_r^R \frac{\mathrm{d}(V_2(x)/x)}{\mathrm{d}x}\frac{\mathrm{d}x}{\sqrt{x^2 - r^2}}. \tag{26}$$

Numerical algorithms for the Abel inversion and comparision with the onion peeling method can be found in [12].

1.4.2 Onion peeling

In the onion peeling method [14], the stress field in an axisymmetric specimen is modelled with N concentric layers, each of thickness Δr and in each of which the stress state is considered to be constant (Fig. 6). The stress components of this discrete model are denoted $\sigma_{z,i}$, $\sigma_{r,i}$, $\sigma_{\theta,i}$ and $\tau_{rz,i}$, where i is the number of the layer, with innermost layer numbered 1 and the outermost N. Distributions of the axial and shear stress components are determined in a manner similar to peeling of an onion - starting from the outermost layer and finishing with the innermost layer. Details can be found in [8].

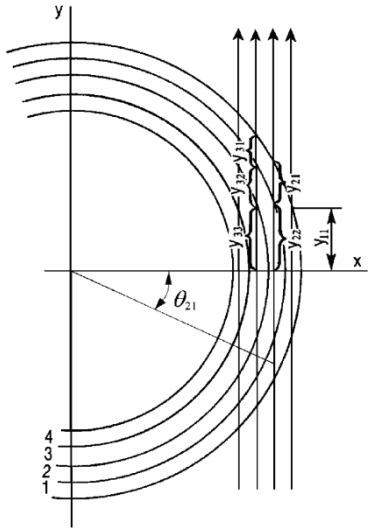

Fig. 6: Layered model of an axisymmetric specimen.

1.5 Determination of radial and circumferential stress components of the axisymmetric stress field

In the case of axisymmetric stress field, equations from the theory of elasticity and the theory of thermoelasticity can be used to determine the remaining stress components, the radial and axisymmetric stress. The employed equations are different for the case of residual stresses and for the case of stresses due to external loading, therefore, these cases are handled separately.

1.5.1 The case of external loads

In the case of external loads, the remaining stress components, σ_r and σ_θ, are determined using the equilibrium equation

$$\frac{\partial \sigma_r}{\partial r} + \frac{\sigma_r - \sigma_\theta}{r} + \frac{\partial \tau_{rz}}{\partial z} = 0, \tag{27}$$

and the compatibility equation

$$\frac{\partial}{\partial r}[\sigma_\theta - \nu(\sigma_r + \sigma_z)] - (1+\nu)\frac{\sigma_r - \sigma_\theta}{r} = 0. \tag{28}$$

Multiplying the equilibrium Eq. (27) by $1+\nu$ and adding to the compatibility equation (28) gives

$$\frac{\partial \sigma_r}{\partial r} + \frac{\partial \sigma_\theta}{\partial r} + (1+\nu)\frac{\partial \tau_{rz}}{\partial z} - \nu\frac{\partial \sigma_z}{\partial r} = 0. \tag{29}$$

Multiplying the equilibrium equation (27) by $\nu - 1$ and adding to the compatibility equation (28) gives

$$-\frac{\partial \sigma_r}{\partial r} + \frac{\partial \sigma_\theta}{\partial r} - 2\frac{\sigma_r - \sigma_\theta}{r} + (\nu - 1)\frac{\partial \tau_{rz}}{\partial z} - \nu\frac{\partial \sigma_z}{\partial r} \tag{30}$$

Rewriting equations (29) and (30) in new terms σ_a, σ_b,

$$\sigma_a = \sigma_r + \sigma_\theta, \tag{31}$$
$$\sigma_b = \sigma_r - \sigma_\theta, \tag{32}$$

gives

$$\frac{\partial \sigma_a}{\partial r} + (1 + \nu)\frac{\partial \tau_{rz}}{\partial z} - \nu\frac{\partial \sigma_z}{\partial r} = 0, \tag{33}$$
$$-\frac{\partial \sigma_b}{\partial r} - \frac{2}{r}\sigma_b + (\nu - 1)\frac{\partial \tau_{rz}}{\partial z} + \nu\frac{\partial \sigma_z}{\partial r} = 0. \tag{34}$$

Integration of Eq. (33) reveals

$$\sigma_a = \nu\sigma_z - (1 + \nu)\int_{r_0}^{r} \frac{\partial \tau_{rz}}{\partial z}\,\mathrm{d}r + C_1 \tag{35}$$

where C_1 is an integration constant.

Numerical integration of Eq. (34) should be done in the direction in which the differential equation is stable or asymptotically stable. Solutions of an ordinary differential equation in the form

$$\frac{\mathrm{d}x}{\mathrm{d}t} = a(t)x + b(t) \tag{36}$$

are asymptotically stable when $a < 0$ for all values of t, stable when $a \leq 0$ for all t and for positive values of a stability cannot be established[17].

Rewriting Eq. (34) in a form similar to Eq. (36), we obtain

$$\frac{\mathrm{d}\sigma_b}{\mathrm{d}r} = -\frac{2}{r}\sigma_b + (\nu - 1)\frac{\partial \tau_{rz}}{\partial z} - \nu\frac{\partial \sigma_z}{\partial r}, \tag{37}$$

from which it follows that $a = -\frac{2}{r} < 0$ for all values of r and therefore solutions of Eq. (34) are asymptotically stable. Thus, numerical integration of Eq. (34) should start at the axis and proceed along the positive direction of the radial axis. A graphical example of integration in the positive direction of the radial axis (Fig. 7) demonstrates quick convergence, thus confirming the analysis. Solutions to the system of Eqs. (27), (28) are linear functions of σ_a, σ_b,

$$\sigma_r = 0.5(\sigma_a + \sigma_b), \tag{38}$$
$$\sigma_\theta = 0.5(\sigma_a - \sigma_b), \tag{39}$$

therefore, the preferred direction of integration is along the positive direction of the radial axis for them, too.

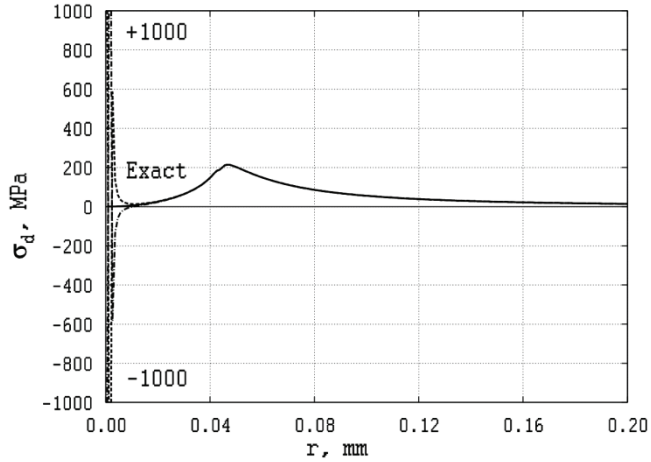

Fig. 7: Three distributions of $\boldsymbol{\sigma_\theta}$ corresponding to three initial values differing by steps of 1000 when integrating along the positive direction of the radial axis.

In the case of a hollow specimen, the initial values of the radial stress at the internal surface, σ_r, can be determined directly from the value of the stress at the internal surface, $\sigma_s(0)$ as follows:

$$\sigma_r(0) = \sigma_s(r_0) \sin 2\beta, \tag{40}$$

where β is the angle of the normal to the internal surface.

In the case of solid specimens the initial values of the radial and circumferential stresses have to be determined so that experimentally determined boundary conditions at the external surface are satisfied. This is done by first performing trial integration of equations (33),(34) with the trial initial value of $\sigma_r(0) = \sigma_\theta(0) = 0$. The difference of boundary conditions and the stresses at the external surface, obtained by trial integration, is added to the initial value and integration is repeated. Different values of the integration constant C_1 in Eq. (35) correspond to different solutions.

The expressions for σ_r and σ_θ, equations (31) and (32), both contain the integration constant with the same factor of 0.5, thus, all solutions to equations (27), (28) differ by a constant value only. Any correction to the initial values changes the value of stress at the external surface by exactly the same amount. Therefore, only one correction is sufficient for obtaining the initial value by which the boundary conditions at the external surface are satisfied.

Let us use the discrete layered model introduced in chapter 1.4.2, i.e. denote the stress components as $\sigma_{z,i}$, $\sigma_{r,i}$, $\sigma_{\theta,i}$ and $\tau_{rz,i}$, where i is the number of the layer, with innermost layer numbered 1 and the outermost N. The numerical

algorithm for determining σ_r and σ_b can be obtained by rewriting (34) as a difference equation and (35) as follows

$$C_1 = \sigma_r(0) + \sigma_\theta(0) - \nu\sigma_z(0), \tag{41}$$

$$\sigma_{a,i} = \nu\sigma_{z,i} - (1+\nu)t_i + C_1, \tag{42}$$

$$\sigma_{b,1} = \sigma_r(0) - \sigma_\theta(0), \tag{43}$$

$$\sigma_{b,i} = \sigma_{b,i-1} + \Delta r\left(-\frac{2}{r_{i-1}}\sigma_{d,i-1} - (\nu-1)\frac{\partial\tau_{rz,i}}{\partial z} - \nu\frac{\partial\sigma_z}{\partial r}\right), \tag{44}$$

where

$$t_i = \sum_{j=0}^{i}\frac{\partial\tau_{rz,i}}{\partial z}\Delta r. \tag{45}$$

Circumferential and radial stress components can be obtained by using equations (38) and (39).

1.5.2 Numerical experiment on the Hertzian contact stress field

The analytical solution to the Hertzian contact problem, a stress field in a hemispace (given by Young's modulus E_2 and Poisson's constant ν_2) indented by a sphere (given by radius R_1, Young's modulus E_1 and Poisson's constant ν_1) with a force P, in cylindrical coordinates r, z, is[16]

$$\begin{aligned}\sigma_r = \frac{3}{2}\Bigg[&\frac{1-2\nu_2}{3}\frac{a^2}{r^2}\left(1-\left(\frac{z}{\sqrt{u}}\right)^3\right) + \left(\frac{z}{\sqrt{u}}\right)^3\frac{a^2u}{u^2+a^2z^2}\\ &+\frac{z}{\sqrt{u}}\left(u\frac{1-\nu_2}{a^2+u}\right.\\ &\left.+(1+\nu_2)\frac{\sqrt{u}}{a}\operatorname{atan}\left(\frac{a}{\sqrt{u}}\right)-2\right)\Bigg],\end{aligned} \tag{46}$$

$$\begin{aligned}\sigma_\theta = -\frac{3}{2}\Bigg[&\frac{1-2\nu}{3}\frac{a^2}{r^2}\left(1-\left(\frac{z}{\sqrt{u}}\right)^3\right)\\ &+\frac{z}{\sqrt{u}}\left(2\nu_2+u\frac{1-\nu_2}{a^2+u}\right.\\ &\left.-(1+\nu_2)\frac{\sqrt{u}}{a}\operatorname{atan}\left(\frac{a}{\sqrt{u}}\right)\right)\Bigg],\end{aligned} \tag{47}$$

$$\sigma_z = -\frac{3}{2}\left(\frac{z}{\sqrt{u}}\right)^3\frac{a^2u}{u^2+a^2z^2}, \tag{48}$$

$$\tau_{rz} = -\frac{3}{2}\frac{rz^2}{u^2+a^2z^2}\frac{a^2\sqrt{u}}{a^2+u}, \tag{49}$$

where the radius of the contact area a and the value u are

$$k = \frac{9}{16}\left[(1-\nu_1) + (1-\nu_2)\frac{E_2}{E_1}\right] \tag{50}$$

$$a = \sqrt[3]{\frac{4kPR_1}{3E_2}} \tag{51}$$

$$u = \frac{1}{2}\left[(r^2 + z^2 - a^2) + \sqrt{(r^2 + z^2 - a^2)^2 + 4a^2z^2}\right]. \tag{52}$$

The values of the parameters of the Hertzian contact problem used in this example are listed in Table 1. The axial and shear stress distribution in the main section, calculated from Eqs. (48),(49), is shown in Fig. 8. The numerical algorithm described by Eqs. (41)-(44) was used to determine radial and circumferential stress components in the main section and the results were compared with the components obtained from the analytical solution, Eqs. (46)-(47). The comparision in Fig. 9 exhibits a good match, thus confirming correctness of the numerical algorithm.

Table 1: Parameters of the Hertzian contact problem.

Parameter	**Value**	**Description**
R_1	2 mm	Radius of the indenter.
E_1	75 GPa	Young's modulus of the indenter.
ν_1	0.3	Poisson's constant of the indenter.
E_2	71.7 GPa	Young's modulus of the hemisphere.
ν_2	0.22	Poisson's constant of the hemisphere.
P	2.7 N	Loading force.
z_1	0.0010 mm	Z-coordinate of the main section.
z_2	0.0011 mm	Z-coordinate of the auxiliary section.

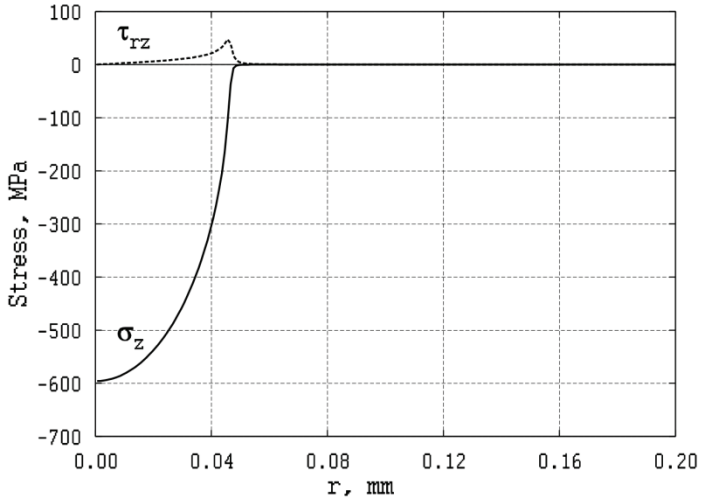

Fig. 8: Axial and shear stress components of the Hertzian contact stress field in the main section.

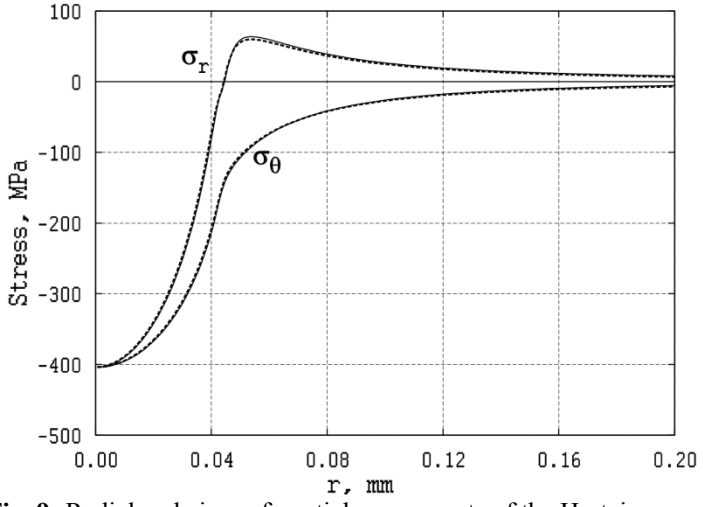

Fig. 9: Radial and circumferential components of the Hertzian contact stress field in the main section. Dashed lines correspond to the components from the analytical solution calculated from Eqs. (46)-(47). Solid lines correspond to the components determined with the numerical algorithm described by Eqs. (41)-(44).

1.5.3 The case of residual stresses in glass

In the case of residual stress in the glass, the compatibility equation cannot be used, since the residual stresses are incompatible. The remaining stress

components, σ_r and σ_θ, are determined using equations of the theory of elasticity. The stress components must satisfy the equation of equilibrium (27) and the generalized sum rule[1]:

$$\sigma_r + \sigma_\theta = \sigma_z - 2\int_{r_0}^{r} \frac{\partial \tau_{rz}}{\partial z} \mathrm{d}r + C_1 \tag{53}$$

where C_1 is an integration constant determined from the boundary conditions at the surfaces of the specimen. Substitution of σ_θ from the sum rule into the equilibrium Eq. (27) reveals a differential equation for the radial stress,

$$\frac{\mathrm{d}\sigma_r}{\mathrm{d}r} + \frac{1}{r}\left(2\sigma_r - \sigma_z + 2\int_{r_0}^{r} \frac{\partial \tau_{rz}}{\partial z} \mathrm{d}r - C_1\right) + \frac{\partial \tau_{rz}}{\partial z} = 0. \tag{54}$$

Rewriting Eq. (54) in a form similar to Eq. (36) gives

$$\frac{\mathrm{d}\sigma_r}{\mathrm{d}r} = -\frac{2}{r}\sigma_r + \frac{1}{r}\left(\sigma_z - 2\int_{r_0}^{r} \frac{\partial \tau_{rz}}{\partial z} \mathrm{d}r + C_1\right) - \frac{\partial \tau_{rz}}{\partial z}. \tag{55}$$

The negative sign of the factor for σ_r shows that the preferred direction of integration of this equation is in the positive direction of the radial axis, the same as for Eq. (34) in the case of stresses due to external loads. Integration in the negative direction of the radial axis is sensitive to small changes in the initial value. This is illustrated in Fig. 10a, where three calculated radial stress distributions corresponding to three initial values, differing only by 0.01, are shown. Stability of integration along the positive directionof the radial axis is illustrated in Fig. 10b.

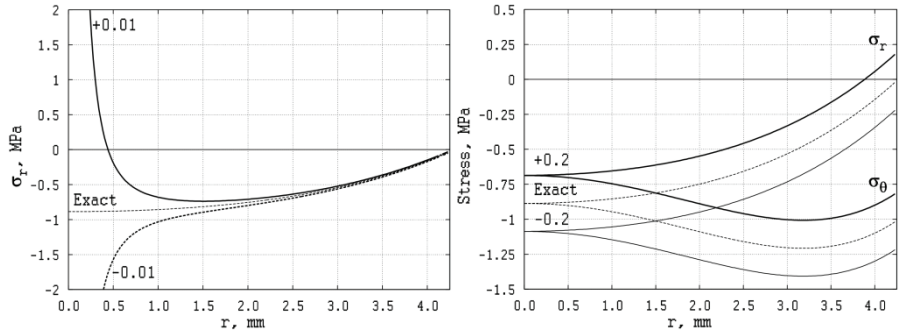

(a) (b)

Fig. 10: Three radial stress distributions corresponding to the three initial values differing by 0.01 when integrating along the negative direction of the radial axis (a) and three radial and circumferential stress distributions corresponding to the three initial values differing by steps of 0.2 when integrating along the positive direction of the radial axis (b).

In the case of solid specimens, the boundary conditions at the external surfaces can be satisfied in the same manner as in the case of the stresses due to external loads. It can be shown that one correction is sufficient for obtaining the initial value by which the boundary conditions at the external surface are satisfied. The integration constant C_1 in Eq. (53) is determined from the boundary conditions at the axis

$$C_1 = 2\sigma_r(0) - \sigma_z(0) \tag{56}$$

where $\sigma_z(0)$ and $\sigma_r(0)$ are the values of axial and radial stress on the axis. Let us define function $f(r)$ as follows:

$$f(r) = \frac{1}{r}\left(\sigma_z - 2\int_{r_0}^{r} \frac{\partial \tau_{rz}}{\partial z}\mathrm{d}r - \sigma_z(0)\right) - \frac{\partial \tau_{rz}}{\partial z} \tag{57}$$

Substitution of $f(r)$ and integration constant C_1 into Eq. (54) gives

$$\frac{\mathrm{d}\sigma_\mathrm{r}}{\mathrm{d}r} + \frac{2}{r}\sigma_r - \frac{2}{r}\sigma_r(0) = f(r). \tag{58}$$

Given that σ_r is a solution corresponding to the initial value $\sigma_r(0)$, we show that adding a constant value C_2 to it also gives a solution by substituting $\sigma_r' = \sigma_r + C_2$ into Eq. (58),

$$\frac{\mathrm{d}(\sigma_r + C_2)}{\mathrm{d}r} + \frac{2}{r}(\sigma_r + C_2) - \frac{2}{r}(\sigma_r(0) + C_2) = f(r). \tag{59}$$

Simplifying Eq. (59) leads back to Eq. (58). All possible solutions differ by a constant value equal to the differences in the initial values $\sigma_r(0)$; this is illustrated in Fig. 10b. Any correction to the initial value changes the value of stress at the external surface for exactly the same amount, thus, only one trial integration is required for obtaining the correct initial value of $\sigma_r(0)$.

In a manner similar to the one in chapter 1.5.1, the numerical algorithm for determining the radial stress distribution is obtained by rewriting Eq. (54) as a difference equation as follows:

$$\sigma_{r,1} = \sigma_r(0), \tag{60}$$

$$\sigma_{r,i} = \sigma_{r,i-1} - \Delta r\left(\frac{1}{r}\left(2\sigma_{r,i-1} - \sigma_{z,i} + 2t_i - C_1\right) + \frac{\partial \tau_{rz,i}}{\partial z}\right), \tag{61}$$

where t_i is defined by (45). Algorithm for determining the circumferential stress distribution is obtained by rewriting the generalized sum rule (53) as follows

$$\sigma_{\theta,i} = \sigma_{z,i} - 2t_i + C_1 - \sigma_{r,i}. \tag{62}$$

1.6 Experimental equipment

1.6.1 Automated transmission polariscope AP-07

The automated polariscope AP-07 (Fig. 11) has been developed for photoelastic measurements by GlasStress Ltd. in cooperation with the Institute of Cybernetics, Tallinn University of Technology. The computer-controlled polariscope permits application of different photoelastic measurement techniques. Recording of the measurement data is made with a CMOS camera and controlled by a laptop PC. Platform with digital indications enables one to measure the geometry of the specimen as well as to select the region of measurements. The polariscope can be configured to work both as a a light-field circular polariscope or a dark-field circular polariscope. The software "GlasStress", elaborated by the author, incorporates the phase-stepping method and algorithms for the determination of stresses in glass objects of various geometries.

The rotary stage (chapter 1.6.2) was constructed in order to permit automatic measurement of projections. The tomographic algorithms were realized in software.

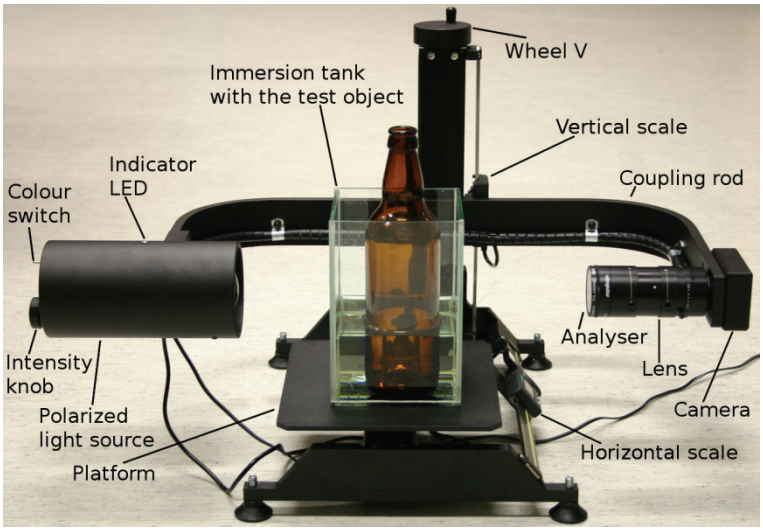

Fig. 11: Automated polariscope AP-07.

Main components of the polariscope:

Polarized light source – collimated LED, peak wavelengths $\lambda_R = 627$ nm (red) and $\lambda_G = 530$ nm (green), 12 VDC at 1A. Polarization is controlled by the program GLASSTRESS. Six possible states of polarization correspond to six

phase steps in the phase-stepping method. Intensity of the light can be changed by turning the knob; colour of the light can be changed by using the switch.

Analyser – dichroic polarizer between glass plates combined with an achromatic quarter-wave plate.

Camera Lens – Computar MLH-10X zoom lens (Fig. 12).

Camera – Lumenera Lu-175M, ½" monochrome CMOS with a resolution of 1024x1280 pixels (Fig. 12).

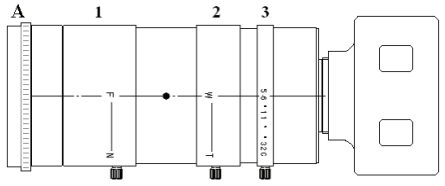

Fig. 12. CMOS camera module with lens. The focus, magnification and diaphragm of the lens system can be adjusted by turning the rings 1, 2 and 3, respectively. A – analyser.

Coupling rod – connects optical components of the polariscope. Using the wheel **V** it can be moved in vertical direction for reaching the measurement area. Range of displacement is 210mm with a resolution of 0.01 mm.

Platform is for supporting and horizontal positioning of the immersion tank with the specimen. Its digital scale can be used for measuring the resolution of the camera and the radius of the specimen. Various regions for stress measurement can be precisely selected by turning the wheel **H** on the right side of the polariscope. Range of displacement is 200 mm with a resolution of 0.01 mm.

1.6.2 Rotary stage

The rotary stage R-01 (Fig. 13) was constructed for rotating a small specimen while placed on the coordinate platform, above the immersion tank. The rotary stage is controlled by the automated polariscope, thus, in turn, controlled by a computer. The rotary stage can accomodate specimens up to 4.5cm in diameter; the minimum rotation step is 0.1 deg.

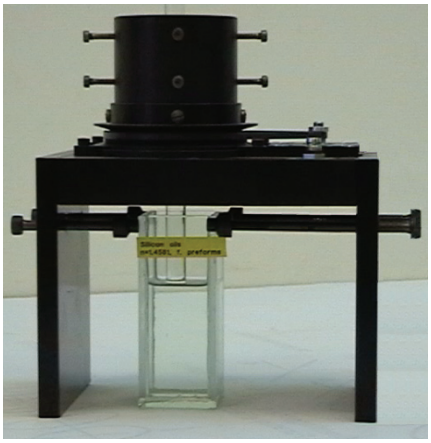

Fig. 13: Rotary stage R-01 with an immersion tank for small objects.

1.7 Examples

1.7.1 The general 3D case, a high-pressure lamp

We describe measurement of the normal stress distribution in section AB of the stem of a high-pressure electric lamp (Fig. 14) made of quartz glass with refraction index of 1.47 and photoelastic constant of $C = 3.40$ TPa^{-1}. In the axisymmetric middle part of the lamp stresses can be determined by approximating stresses with axisymmetric polynomials[5].

180 projections were recorded, with a step $\Delta\beta = 1$ deg. In addition to the photoelastic data, a photo of the specimen in a light-field circular polariscope was also recorded for every projection angle. Contour of the cross-section AB (Fig. 15) was obtained by using filtered backprojection method[18,20] in the program CTSim[22] on these photos. Projections of photoelastic data for stress field reconstruction were extracted in two sections, the main section being AB and the auxiliary section at 1 mm apart from it. Since processing of projections from theses sections were similar, only data for the main section will be shown. Projections of optical retardation Δ are shown in Fig. 16a and projections of the isoclinic angle φ (direction of σ_1) in section AB are shown in Fig. 16b. The electrode appears deformed in projections in Fig. 16 because it did not coincide with the rotation axis of the specimen.

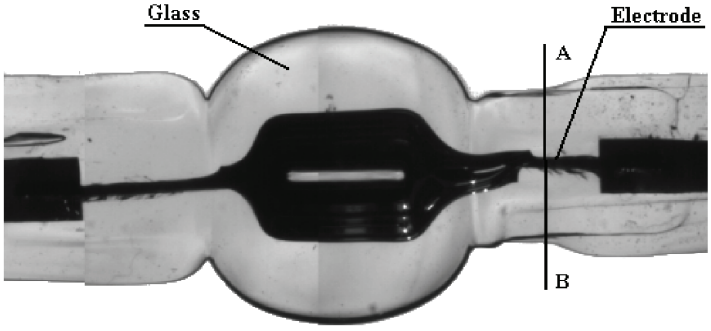

Fig. 14: Image of the high-pressure lamp in a light-field circular polariscope and the cross-section at the line AB.

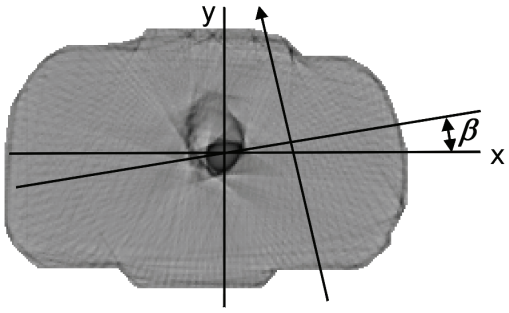

Fig. 15: Geometry of the cross-section AB.

Projections of $\Delta \cos 2\varphi$ and $\Delta \sin 2\varphi$ in section AB are shown in Fig. 17, which are directly used in Eqs. (3) and (4). Image of the electrode is straightened by shifting the projections for different angles β. Similar data was obtained for the auxiliary section of the stem.

On the basis of Fig. 17 and the contour from Fig. 15 the field of the normal stress σ_z (Fig. 18) was determined from the Fourier series of projections as in Eq. (12) with 16 terms along the radial coordinate and 16 terms along the angular coordinate. Distribution of σ_z on the x and y axes is shown in Fig. 19.

Since σ_z is a residual stress, theoretically its average value should be zero. The actual average value of σ_z in section AB is 0.2 MPa. That is about 5 percent of the maximum value of σ_z near the electrode.

Another possibility to check the precision of the results is comparison of measured experimental data with the data, calculated on the basis of the calculated stress field. Such a comparison of the distribution of $\Delta \cos 2\varphi$ (a) for the projection $\beta = 120$ deg is shown in Fig. 20.

Both checks permit to conclude that precision of tomographic measurement of the normal stress field is satisfactory.

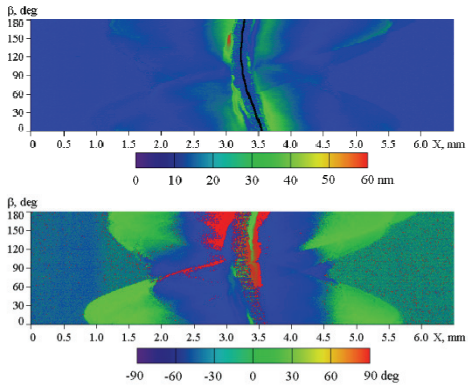

(a) (b)

Fig. 16: Projections of Δ (a) and φ (b) in section AB for β = 0 - 180 deg.

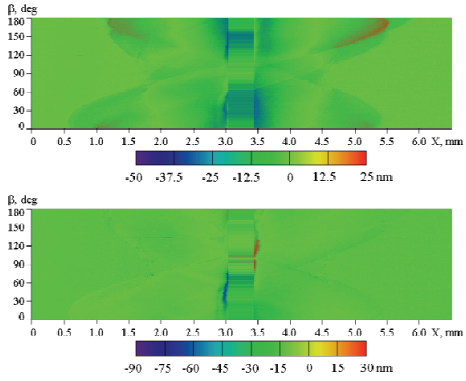

(a) (b)

Fig. 17: Projections of Δcos2φ (a) and Δsin 2φ (b) in section AB.

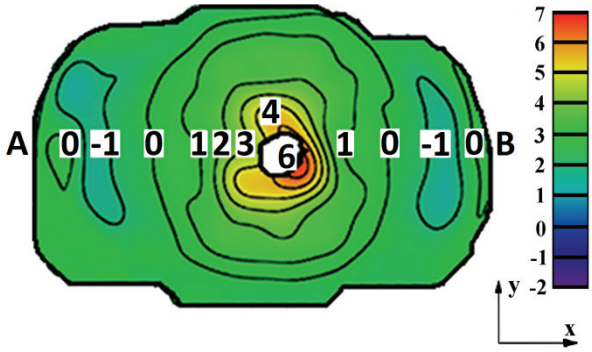

Fig. 18: Normal stress field in section AB.

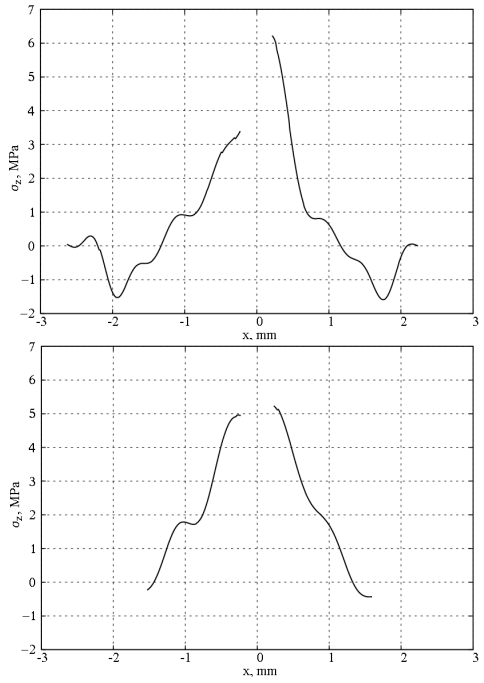

(a) (b)

Fig. 19: Normal stress σ_z distribution on the axes x (a) and y (b) in section AB.

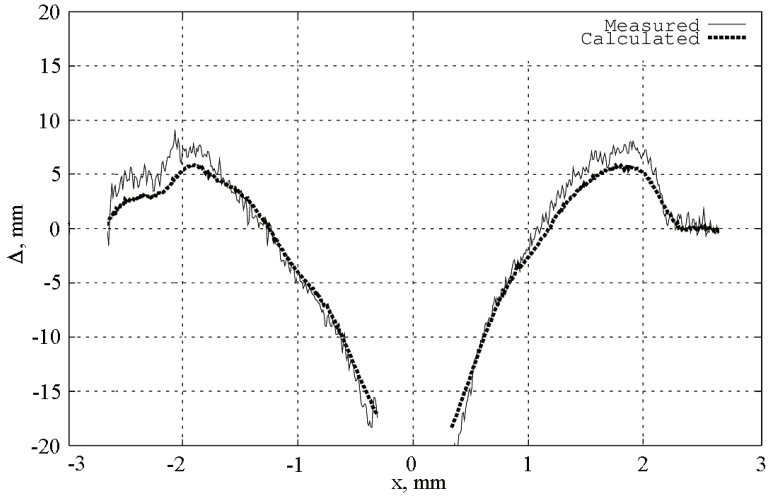

Fig. 20: Measured and calculated distribution of $\Delta\cos 2\varphi$ (a) for the projection $\beta = 120°$.

1.7.2 Axisymmetric case of external loads, a soda-lime optical fibre

As a practical example of the numerical algorithm for the case of stresses due to external loads, stresses were determined in a soda-lime fibre indented by a spherical indentor (Fig. 21). The fibre has a rectangular cross-section and it was positioned horizontally for the time of measurements. Dimensions of the fibre are much larger than the extent of the indentation, therefore stresses can be determined as if it was an axisymmetric specimen. Image of the fibre in a white-field circular polariscope is shown in Fig. 22. Distribution of stresses at the top surface of the soda-lime fibre are shown in Fig. 23.

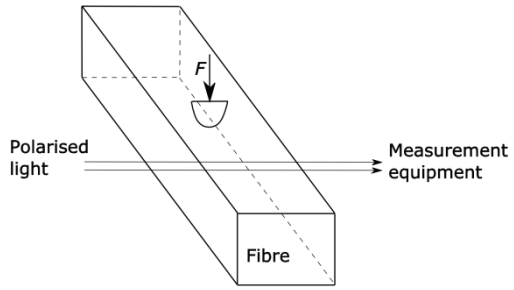

Fig. 21: Measurement scheme of stresses in a soda-lime optical fibre indented by a spherical indentor.

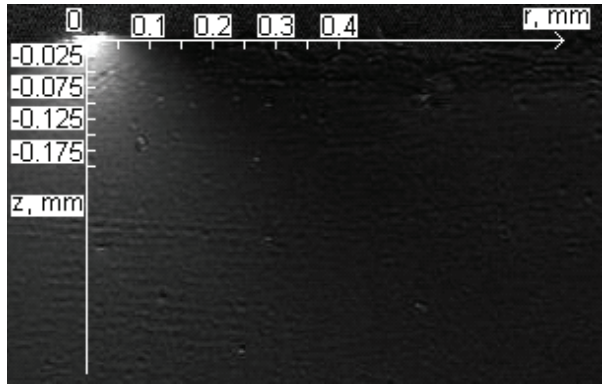

Fig. 22: Image of the soda-lime fibre under spherical indentor in a white-field circular polariscope.

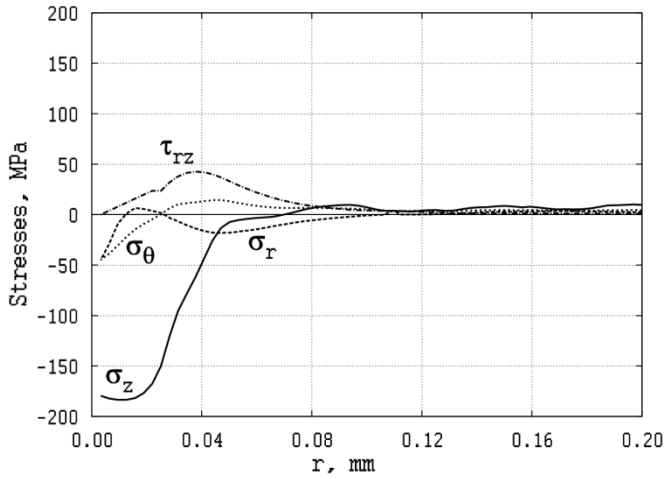

Fig. 23: Distribution of stresses due to spherical indentor at the top surface of the soda-lime fibre.

1.7.3 Axisymmetric case of residual stresses, a stem of a wine glass

As an experimental example for the case of residual stresses, stresses in the stem of a wine glass were determined. Geometry of the wine glass is shown in Fig. 24a and the fringe pattern in Fig. 24b. Results of stress determination in section 1 are shown in Fig. 25. As a verification of the precision of the algorithm, the birefringence, corresponding to the determined stress state, was calculated using the Jones matrix formalism[26] and compared with the measured birefringence (Fig. 26). The match is excellent.

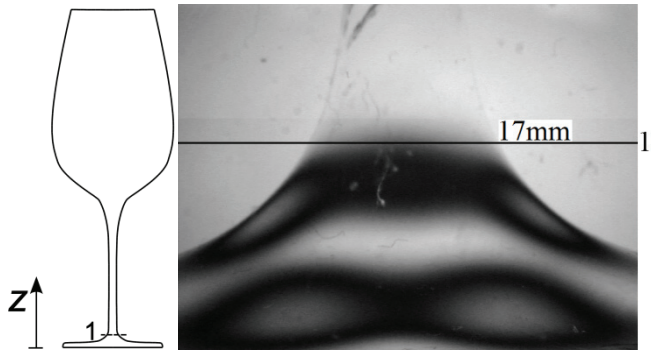

Fig. 24: Geometry of a wine glass (a) and fringe pattern in the bottom of the stem (b).

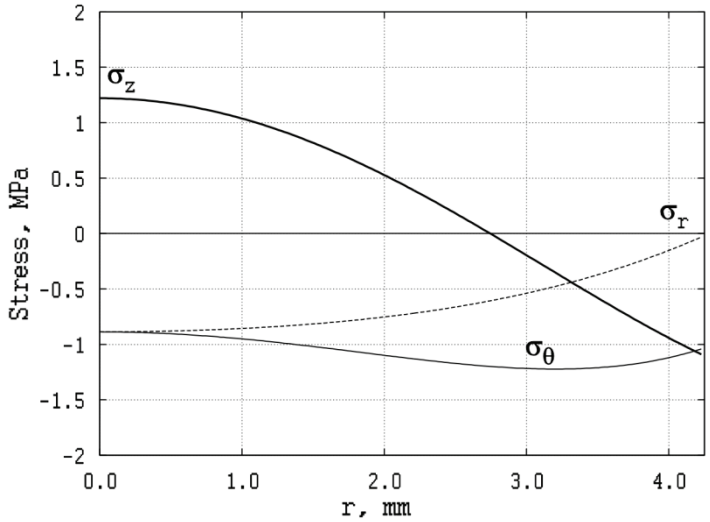

Fig. 25: Distribution of stress components in section 1.

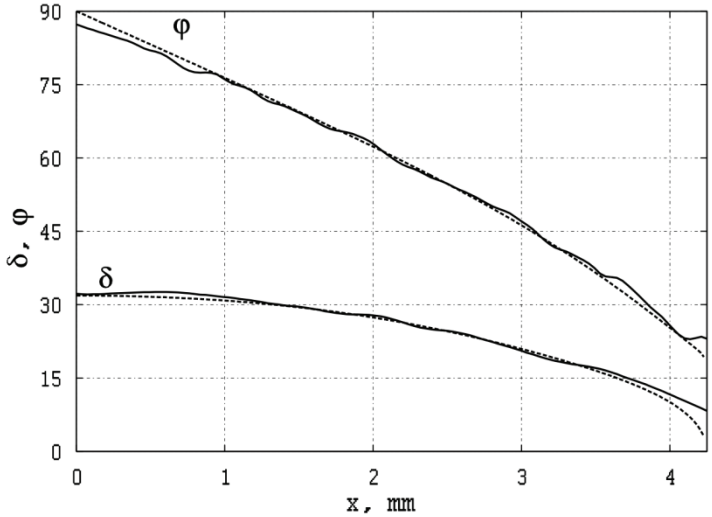

Fig. 26: Measured birefringence (solid line) and calculated birefringence corresponding to the determined stress state (dashed line).

2 Non-linear photoelastic tomography

In many cases assumptions of the linear approximation are not valid and the problem of photoelastic tomography is to be formulated in the general, non-linear form.

2.1 Expressions for stresses

We present stress components σ_r, σ_θ, σ_z and τ_{rz} in cylindrical coordinates r, θ, z, in the form of polynomials relative to the radial coordinate r:

$$\sigma'_r = \sum_{k=0}^{m} a'_{2k} r^{2k}, \qquad \sigma'_\theta = \sum_{k=0}^{m} b'_{2k} r^{2k}, \sigma'_z = \sum_{k=0}^{m} c'_{2k} r^{2k}, \qquad \tau'_{rz} = \sum_{k=1}^{m+1} d'_{2k-1} r^{2k-1} \tag{63}$$

where prime denotes the main section. In the auxiliary section, the stress components are expressed in the same way, distinguishing the coefficients with a double prime.

Our aim is to determine the coefficients a'_{2k}, b'_{2k}, c'_{2k}, d'_{2k-1}, a''_{2k}, b''_{2k}, c''_{2k}, and d''_{2k-1} on the basis of experimentally measured φ_i^m and Δ_i^m (i = 1, ... , n) in both sections.

The number of unknown coefficients can be reduced using equations of the theory of elasticity, boundary conditions and macrostatic equilibrium conditions. The stress components must satisfy the equation of equilibrium (27). In the case of residual stress in glass, the generalized sum rule, Eq. (53), is valid.

Using the equilibrum equation and the generalized sum rule, the stress components σ_r and σ_θ can be expressed as[7]

$$\sigma_r = -\int_{r_0}^{r} \frac{\partial \tau_{rz}}{\partial z} \mathrm{d}r + \frac{1}{r^2} \int_{r_0}^{r} r\sigma_z \mathrm{d}r + \frac{1}{2}\frac{1}{r^2} C_2 + C_4, \tag{64}$$

$$\sigma_\theta = \sigma_z - \int_{r_0}^{r} \frac{\partial \tau_{rz}}{\partial z} \mathrm{d}r - \frac{1}{r^2} \int_{r_0}^{r} r\sigma_z \mathrm{d}r - \frac{1}{2}\frac{1}{r^2} C_2 + C_4. \tag{65}$$

Constants C_2 and C_4 are determined from the boundary conditions.

Introducing expressions (63) into equations (64) and (65), stress components σ_r and σ_θ can be expressed as

$$\sigma_r' = -\sum_{k=1}^{m} \frac{1}{2k} \overline{d}_{2k-1} \left(\rho^{2k} - \rho_0^{2k}\right) + \sum_{k=0}^{m} \frac{2}{2k+2} c_{2k}' \left(\rho^{2k} - \rho_0^{2k}\right) + \frac{1}{2\rho^2} C_2' + C_4', \tag{66}$$

$$\sigma_\theta' = \sum_{k=0}^{m} c_{2k}' \rho^{2k} - \sum_{k=1}^{m} \frac{1}{2k} \overline{d}_{2k-1} \left(\rho^{2k} - \rho_0^{2k}\right) - \sum_{k=0}^{m} \frac{1}{2k+2} c_{2k}' \left(\rho^{2k} - \rho_0^{2k}\right) - \frac{1}{2\rho^2} C_2' + C_4'. \tag{67}$$

Here

$$\rho = \frac{r}{R}, \qquad \rho_0 = \frac{r_0}{R}, \qquad \overline{d}_{2k-1} = \frac{d_{2k-1}'' - d_{2k-1}'}{\Delta z} R', \tag{68}$$

and R and R' are the external radiuses of sections 1 and 2. Similar expressions are valid for the stress components σ_r'' and σ_θ'' in section 2. Thus all the stress components in sections 1 and 2 can be expressed through the coefficients c_{2k}', c_{2k}'', d_{2k-1}' and d_{2k-1}''.

The second equilibrium equation

$$\frac{\partial \sigma_z}{\partial z} + \frac{\partial \tau_{rz}}{\partial r} + \frac{1}{r} \tau_{rz} = 0 \tag{69}$$

permits to eliminate coefficients c_{2k}''. Let us call the coefficients c_{2k}', d_{2k-1}' and d_{2k-1}'' stress coefficients s_i (i = 1, ... l). They permit calculation of all the stress components. The set of the stress coefficients is named stress vector $\boldsymbol{S}$, which has l components.

2.2 The differential evolution algorithm

Our aim is to find the stress vector, which corresponds best to the measurement data. For that we use the differential evolution (DE) algorithm[21]. Differential evolution is a parallel direct research method for finding optimum values of the components of a vector. The initial population of the vectors is chosen randomly if nothing is known about the system. In case a preliminary solution is available, the initial population can be generated by adding normally distributed random deviations to the nominal solution. The crucial idea behind DE is a scheme for generating trial vectors. DE generates new vectors by adding a weighted

difference vector between two population members to a third member. If the resulting vector yields a lower objective function than a predetermined population member, the newly generated vector will replace in the following generation the vector, with which it was compared. The best vector is evaluated for every generation to keep track of the progress that is made during the minimization process. Extracting distance and direction information from the population to generate random deviations results in an adaptive scheme with excellent convergence properties.

For the determination of the stress vector $\boldsymbol{S}$, which corresponds best to the measurement data, the following method was used. First, the parameter of the isoclinic φ_i^m and optical retardation are measured in both main and auxiliary sections on n light rays. For every stress vector $\boldsymbol{S}$ it is possible to calculate for the same light rays i the parameters φ_i^c and Δ_i^c. For example, by modelling the test object on a light ray as a pile of birefringent plates, each of which is described by a Jones' vector[26]. The objective (penalty) function F

$$F = \frac{1}{n}\sum_{i=1}^{n}\left[\left(\frac{\Delta_i^c \cos 2\varphi_i^c - \Delta_i^m \cos 2\varphi_i^m}{\varepsilon}\right)^2 + \left(\frac{\Delta_i^c \sin 2\varphi_i^c - \Delta_i^m \sin 2\varphi_i^m}{\varepsilon}\right)^2\right] \tag{70}$$

characterizes how well the stress vector describes the real stress field. Here ε is the measurement error. The penalty function F takes into account all the measurement data on the n light rays.

General algorithm of the method is shown in Fig. 27 and the algorithm of DE in Fig. 28.

In practical application of the algorithm we generated the initial population of 100 stress vectors by adding normally distributed random deviations to the solution of linear photoelastic tomography.

According to Fig. 27, on the basis of the measurement data and of the generated stress vectors, the penalty function F_j for every generated stress vector is calculated. Most important is the smallest penalty function of the population, min F_j. If F_j is sufficiently small, one may have obtained a satisfactory solution, i.e., a stress field that corresponds to the real measurement data well enough. If not, using the differential evolution algorithm, a new population of stress vectors is generated, penalty functions for this population are calculated, etc.

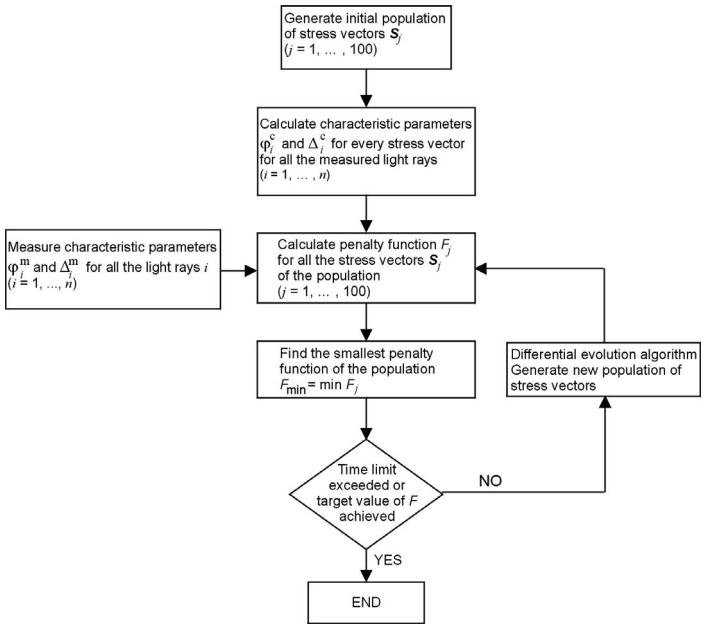

Fig. 27: General algorithm of non-linear photoelastic tomography.

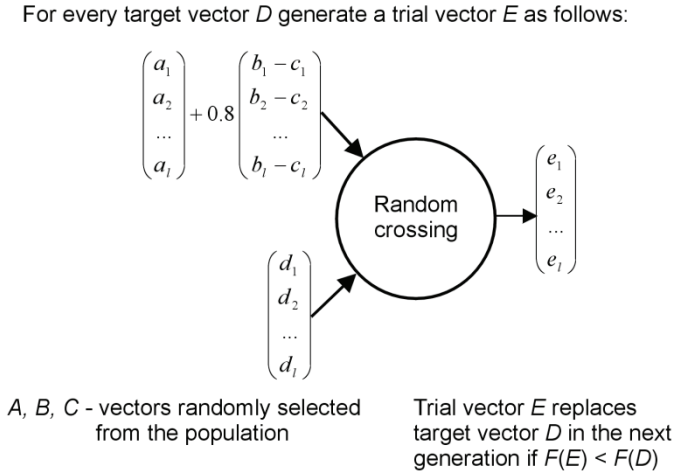

Fig. 28: Basic algorithm of differential evolution.

Modification of stress vectors $D(d_1, d_2, \dots d_i)$ of the initial population into stress vectors $E(e_1, e_2, \dots e_e)$ of the new generation, using other three stress vectors A, B, and C of the initial population, is shown in Fig. 28.

Random crossing (Fig. 28) was carried out as follows:

$$e_i = \begin{cases} a_i + 0.8(b_i - c_i) & \text{if} \quad r < p, \\ d_i & \text{if} \quad r \geq p, \end{cases} \tag{71}$$

where r is a random number between 0 and 1 and p is a parameter, which can be chosen by the operator. We used $p = 0.9$, which has proved to be efficient in practical applications[21].

The algorithm, shown in Fig. 27 and Fig. 28, was programmed in C++. Implemented on the computer IBM R50E, 400 iterations take 20 min.

2.3 Experiment

As an example of a non-linear photoelastic tomography, residual stresses near the rim in a rim-tempered drinking glass (Fig. 29) were investigated. In section 1 (z = 28.1 mm) optical retardation is less than 100 nm and therefore Eqs. (3) and (4) of the linear approximation are valid. Stresses in section 1 were determined with a linear algorithm of photoelastic tomography[4]. By approximating stresses, in Eqs. (63) we used m = 3. Thus the number of the coefficients of the stress vector was $l = 11$. Fig. 30 shows the measurement data as well as data that is calculated on the basis of obtained stress distribution, shown in Fig. 31. We see that experimentally measured and calculated data are very close. That indicates that in section 1 linear approximation of photoelastic tomography is valid. In section 1 we obtained $F(1) = 0.4$.

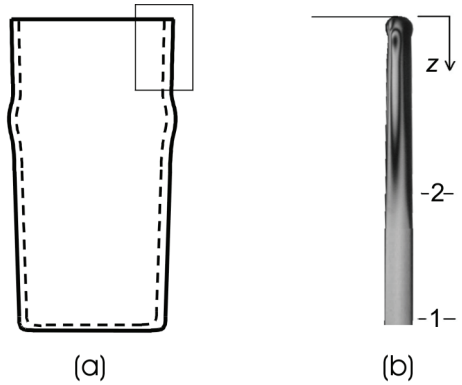

Fig. 29: Geometry of a rim-tempered glass (a) and integrated fringe pattern near the rim (b).

In section 2 (z = 16.8 mm) optical retardation reached 300 nm. In case of rotation of the principal stress axes that is somewhat more than allowed in linear photoelastic tomography, as mentioned before. Fig. 32 shows measured data in section 2.

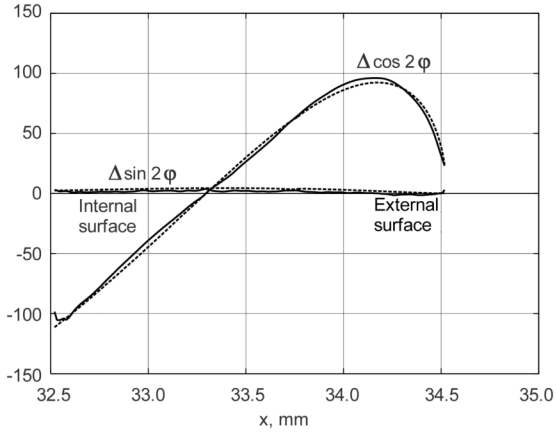

Fig. 30: Experimentally measured and calculated data in section 1: —— measured, – – – calculated.

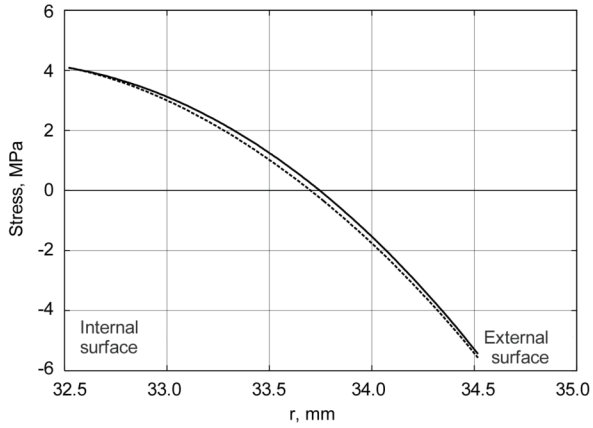

Fig. 31: Stresses $\boldsymbol{\sigma_z}$ (——) and $\boldsymbol{\sigma_\theta}$ (– – –) in section 1, determined with linear photoelastic tomography.

On the basis of the measurement data in section 2, stresses were calculated using the algorithm of linear photoelastic tomography[4](Fig. 33). Using measured stresses, theoretical measurement data were calculated (Fig. 32). Fig. 32 shows that the difference between measured and calculated data is much bigger than in section 1, especially for $\Delta \sin 2\varphi$. That is expressed also in the value of the penalty function: $F(2) = 59$. It is an indication that in section 2 the linear approximation is not valid.

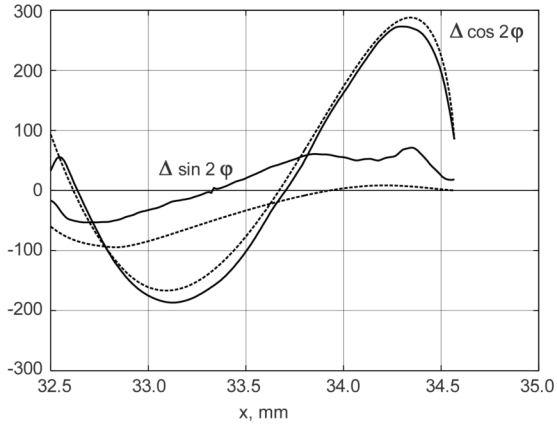

Fig. 32: Experimentally measured (——) and calculated (– – –) data in section 2.

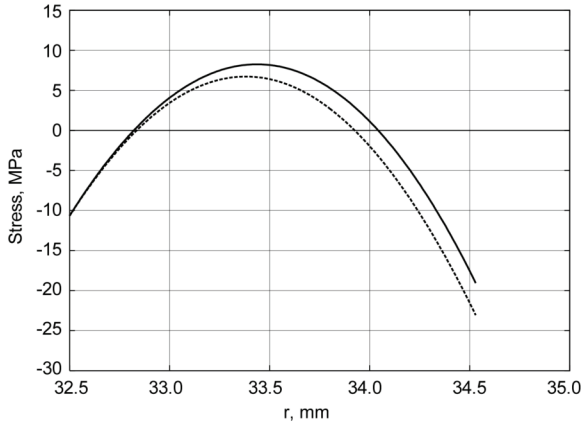

Fig. 33: Stresses $\boldsymbol{\sigma_z}$ (——) and $\boldsymbol{\sigma_\theta}$ (– – –) in section 2, determined with the linear algorithm.

Using the DE method, final stress distribution in section 2 was obtained (Fig. 34). In comparison with Fig. 33 the change of σ_θ is remarkable. The decrease of the penalty function F during the DE procedure is shown in Fig. 35. After the 150th generation the penalty function remains about constant, $F \cong 3$.

In Fig. 34 practically $\sigma_\theta \cong \sigma_z$. That was to be expected. In a cylindrical object with weak stress gradient in z direction the classical sum rule

$$\sigma_r + \sigma_\theta = \sigma_z, \tag{72}$$

is valid[5]. Since $\sigma_r \cong 0$, it follows from Eq. (72) that $\sigma_\theta \cong \sigma_z$.

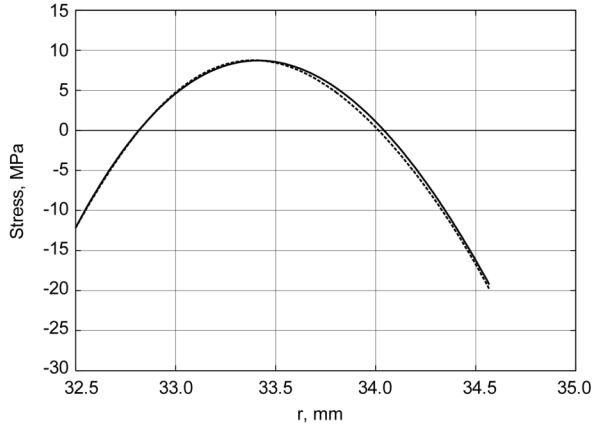

Fig. 34: Stresses $\boldsymbol{\sigma_z}$ (——) and $\boldsymbol{\sigma_\theta}$ (– – –) in section 2, determined with the non-linear algorithm.

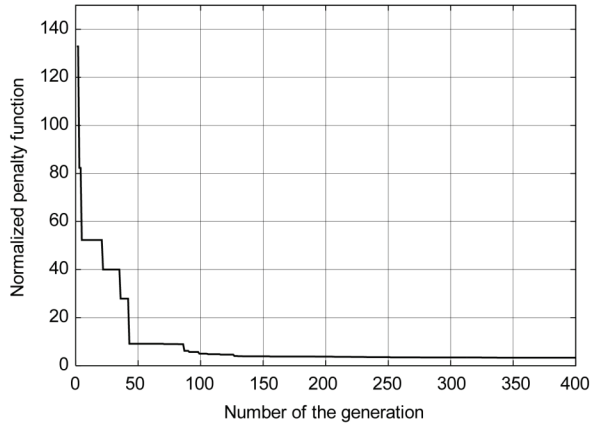

Fig. 35: Dependence of the penalty function on the number of generation in the DE process.

Fig. 36 shows a comparison of the experimentally measured and calculated, on the basis of the final stress distribution, data in section 2. Coincidence of the measured and calculated data is considerably better than that shown in Fig. 32, especially for the term $\Delta \sin 2\varphi$.

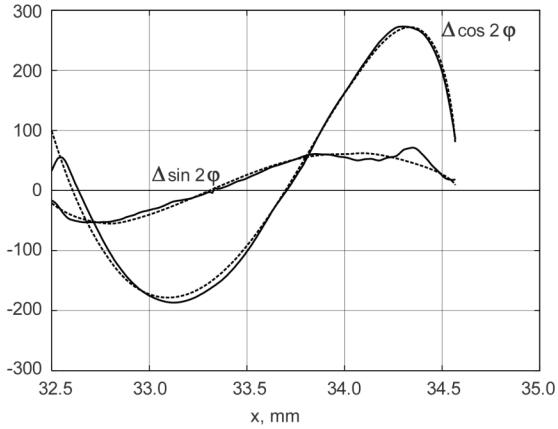

Fig. 36: Experimentally measured (——) and calculated (– – –), on the basis of the final stress distribution, data in section 2.

3 Conclusions

A measurement technology for photoelastic tomography in linear approximation for the determination of normal components of 3D stress fields is described.

In the case of axisymmetric stress fields, it has been shown that the Abel inversion, which is essentially a method for determining scalar fields, can also be applied for the determination of the axial and shear stress components.

The radial and circumferential components of axisymmetric stress field can be determined by using the equilibrium equation and the compatibility equation (in the case of external loads) or the generalized sum rule from the theory of thermoelasticity (in the case of residual stresses). The stability of solutions to these equations has been studied both analytically and numerically, and, the recommended direction of integration was determined to be along the positive direction of the radial axis. Numerical algorithms for the determination of radial and circumferential components have been elaborated. In the case of external loads, the results of the numerical algorithm have been shown to match the radial and circumferential components of the analytical solution to the Hertzian contact problem when the algorithm was working on the axial and shear stress components of the same field.

For the case when the linear approximation is no longer valid, an algorithm employing differential evolution (a genetic algorithm) has been elaborated for the determination of complete axisymmetric stress field. The algorithm seeks stress polynomials such that the corresponding birefringence distribution fits best with the measurement data. Due to the axial symmetry of the stress field the measurement data is exactly the same as in the case of linear algorithm.

Practical examples have been provided for all the cases.

References

1. Aben H., Ainola L., Anton J. Sum rules for photoelastic stress measurement in axisymmetric glass articles. In *Proc. International Conference on Advanced Technology in Experimental Mechanics ATEM'99*, Ube, Japan, 1999, **2**, 629-634.
2. Aben, H., Anton, J., Errapart, A. Modern photoelasticity for residual stress measurement in glass. *Strain*, 2008, **44**(1), 40 - 48.
3. Aben H., Errapart A., Ainola L. On real and imaginary algorithms of optical tensor field tomography. *Proc. Est Acad Sci Phys Math*, 2006, **55**, 112-127.
4. Aben H., Errapart A., Ainola L., Anton J. Photoelastic tomography for residual stress measurement in glass. *Opt Eng*, 2005, **44**, 1-8 (093601).
5. Aben H, Guillemet C. *Photoelasticty of Glass*. Springer, Berlin, 1993.

6. Aben H.K., Josepson J.I., Kell K-J. The case of weak birefringence in integrated photoelasticity. *Opt Lasers Eng*, 1989, **11**, 145-157.
7. Ainola L., Aben H. A new relationship for the experimental-analytical solution of the axisymmetric thermoelasticity problem. *ZAMM*, 2004, **84**, 211-215.
8. Anton J., Errapart A., Aben H., Ainola L. A Discrete Algorithm of Integrated Photoelasticity for Axisymmetric Problems. *Exp Mech*, 2008, **48**, 613-620.
9. Born, M., Wolf, E. *Principles of Optics*. Pergamon Press, New York, 1986.
10. Bracewell, R. *The Fourier Transform and its Applications*. McGraw-Hill, 1999.
11. Cormack, A.M. Representation of a Function by its Line Integrals, With Radiological Applications. *J Appl Phys*, 1963, **34**, 2722-2727.
12. Dash C.J. One-dimensional tomography: a comparison of Abel, onion-peeling and filtered backprojection methods. *Appl Opt*, 1992, **31**, 1146-1152.
13. Doyle J.F., Danyluk H.T. Integrated photoelasticity for axisymmetric problems. *Exp Mech* 1978, **18**, 156-220.
14. Drucker, D.C., Woodward, W.B. Interpretation of Photoelastic Transmission Patterns for a Three-Dimensional Model. *J Appl. Phys*. 1954, **25**, 510-512.
15. Errapart, A. On the technology of photoelastic tomography. *Experimental Techniques*, 2008, **32**(1), 31 - 35.
16. Fischer-Cripps, A.C. *Introduction to Contact Mechanics*. Springer, New York, 2007.
17. Hazewinkel M. *Encyclopaedia of Mathematics*. Kluwer Academic Publishers, London, 1998
18. Herman C. T. *Image Reconstruction from Projections*. Academic Press, New York, 1980.
19. Mason, J.C. *Chebyshev Polynomials*. Chapman & Hall/CRC Press, Roca Baton, FL, 2002.
20. Natterer F. *The Mathematics of Computerized Tomography*. Teubner, Stuttgart, 1986.
21. Price K.V., Storn R.M., Lampinen J.A. *Differential evolution, a practical approach to global optimisation*. Springer, Berlin, 2005.
22. Rosenberg, K. M. CTSim 3.5 User Manual, URL http://files.b9.com/ctsim/ctsim-manual-latest.pdf [accessed 27th of March, 2011]
23. Schupp, D. *Optische Tensortomographie zur Bestimmung räumlicher Spannungsverteilungen*. Tech Mess, 1999, **66**, 54-60.
24. Sharafutdinov V. A. *Integral Geometry of Tensor Fields*. VSP, Utrecht, 1994.

25. Sharafutdinov V. On integrated photoelasticity in case of weak birefringence. *Proc Est Acad Sci Phys Math*, 1989, **38**, 379-389.
26. Theocaris P.S., Gdoutos E.E. *Matrix theory of photoelasticity*. Springer, Berlin, 1979.

List of author's publications

1. Aben, H., Errapart, A. Photoelastic tomography with linear and non-linear algorithms (in press). Exp Mech, 2012. http://dx.doi.org/10.1007/s11340-011-9575-z.
2. Aben, H., Ainola, L., Errapart, A. Photoelastic tomography as hybrid mechanics. In *Recent Advances in Mechanics : Selected Papers from the Symposium, Academy of Athens, Athens, Greece, 17-19 September, 2009, Organised by the Pericles S. Theocaris Foundation in Honour of P. S. Theocaris, on the Tenth Anniversary of His Death* (Kounadis, A. N., Gdoutos, E. E., eds.). Springer, Heidelberg, 2011, 181-190.
3. Errapart, A., Aben, H., Ainola, L., Anton, J. Photoelastic tomography for the measurement of thermal and residual stresses in glass. In *Thermal Stresses 2011 [9th International Congress, June 5-9, 2011, Budapest] : with Naotake Noda Symposium*, Hungarian Academy of Sciences Budapest, Hungary, 2011.
4. Anton, J., Errapart, A., Paemurru, M., Lochegnies, D., Hödemann, S., Aben, H. In *On the inhomogeneity on residual stresses in tempered glass panels. Glass Performance Days [GPD 2011] : Conference Proceedings, 17 - 20 June, Tampere, Finland*. Glaston Finland OY, Tampere, 2011, 119-121.
5. Errapart, A. Determination of all stress components of axisymmetric stress state in photoelastic tomography. In *Advances in Experimental Mechanics VIII : Selected, peer-reviewed papers of the 8th International Conference on Advances in Experimental Mechanics: Integrating Simulation and Experimentation for Validation, (BSSM 2011), Sept. 7-9 2011, Edinburgh, Scotland* (Burguete R. L. et al., eds.). Trans Tech Publications, Durnten-Zuerich, 2011, 434-439.
6. Hödemann, S., Kikas, J., Aben, H., Anton, J., Errapart, A. Effects of ray bending in scattered light photoelasticity for tempered and annealed glass plates. In *Advances in Experimental Mechanics VIII : Selected, peer-reviewed papers of the 8th International Conference on Advances in Experimental Mechanics: Integrating Simulation and Experimentation for Validation, (BSSM 2011), Sept. 7-9 2011, Edinburgh, Scotland* (Burguete R. L. et al., eds.). Trans Tech Publications, Durnten-Zuerich, 2011, 440-445.
7. Errapart, A., Aben, H. Photoelastic tomography in the axisymmetric and non-axisymmetric case. In *FVR 2011 : Forum on recent developments in Volume Reconstruction techniques applied to 3D fluid and solid mechanics 2011, Futuroscope-Poitiers, France, November 29th - December 1st, 2011*. Institut P', Futuroscope, France, 2011, 127-130.

8. Errapart, A., Anton, J. Photoelastic residual stress measurement in nonaxisymmetric glass containers. *EPJ Web of Conferences*, 2010, **6**, 32008-1 - 32008-6.
9. Aben, H., Anton, J., Errapart, A., Hödemann, S., Kikas, J., Klaassen, H., Lamp, M. On non-destructive residual stress measurement in glass panels. *Estonian Journal of Engineering*, 2010, **16**(2), 150-156.
10. Aben, H., Ainola, L., Anton, J., Errapart, A. Photoelastic tomography as hybrid mechanics. In *Symposium on Recent Advances in Mechanics : Dedicated to the Late Academician - Professor Pericles S. Theocaris, September 17-19, 2009, Athens, Greece* (Kounandis A. N., Gdoutos E. E., eds.). Pericles S. Theocaris Foundation, Athens, 2009, 25-26.
11. Aben, H., Anton, J., Errapart, A., Hödemann, S., Kikas, J., Klaassen, H., Lamp, M. On complete non-destructive residual stress measurement in architectural glass panels and automotive glazing. In *Glass Performance Days : Conference Proceedings, Tampere, Finland, 12-15 June 2009*. Glaston Finland OY, Tampere, 2009, 923-925.
12. Aben, H., Ainola, L., Errapart, A. Application of the Abel inversion in case of a tensor field. - *Inverse Problems in Science and Engineering*, 2010, **18**(2), 241-249.
13. Anton J., Errapart A., Aben H., Ainola L. A Discrete Algorithm of Integrated Photoelasticity for Axisymmetric Problems. *Exp Mech*, 2008, **48**, 613-620.
14. Errapart, A. On the technology of photoelastic tomography. *Experimental Techniques*, 2008, **32**(1), 31 - 35.
15. Aben, H., Anton, J., Errapart, A. Modern photoelasticity for residual stress measurement in glass. *Strain*, 2008, **44**(1), 40 - 48.
16. Aben, H., Errapart, A. A non-linear algorithm of photoelastic tomography for the axisymmetric problem. Exp Mech, 2007, **47**(6), 821 - 830.
17. Aben, H., Anton, J., Errapart, A. Modern photoelasticity for residual stress measurement in glass. In *Experimental Analysis of Nano and Engineering Materials and Structures: Proceedings of the 13th International Conference on Experimental Mechanics, Alexandroupolis, Greece, July 1-6, 2007* (Gdoutos, E.E., ed.). Springer, Dordrecht, 2007, 8 p.
18. Aben, H., Errapart, A. Linear and non-linear algorithms of photoelastic tomography. In *Experimental Analysis of Nano and Engineering Materials and Structures: Proceedings of the 13th International Conference on Experimental Mechanics, Alexandroupolis, Greece, July 1-6, 2007* (Gdoutos, E.E., ed.).Springer, Dordrecht, 2007, 8 p.
19. Aben, Hillar, Anton, J. Errapart, A. Modern photoelasticity for residual stress measurement in glass. In *Experimental Analysis of Nano and Engineering Materials and Structures: Proceedings of the 13th*

International Conference on Experimental Mechanics, Alexandroupolis, Greece, July 1-6, 2007 (Gdoutos, E.E., ed.).Springer, Dordrecht, 2007, 3-4.

20. Aben, Hillar; Errapart, Andrei; Sanko, Jelena; Anton, Johan (2006). A non-linear algorithm of photoelastic tomography for the axisymmetric problem. In: Photomechanics 2006 : International Conference on Full-field Measurement Techniques and their Applications in Experimental Solid Mechanics, Clermont-Ferrand, France, July 10-12, 2006, Book of Abstracts: (Toim.) Grédiac, M.; Huntley, J.. Clermont-Ferrand:, 2006, 2 p..
21. Aben H., Errapart A., Ainola L. On real and imaginary algorithms of optical tensor field tomography. *Proc. Est Acad Sci Phys Math*, 2006, **55**, 112-127.
22. Aben H., Errapart A., Ainola L., Anton J. Photoelastic tomography for residual stress measurement in glass. *Opt Eng*, 2005, **44**, 1-8 (093601).
23. Errapart, A., Anton, J., Aben, H., (2005). On data-processing in photoelastic stress measurement in glass. In *Proceedings of ICEM05 : International Congress on Experimental Mechanics & 4th Asian Conference on Experimental Mechanics, 12th-14th September, 2005, New Delhi, India*. SEM, New Delhi, 2005, 6 p.
24. Aben, H.; Errapart, A. Photoelastic tomography: possibilities and limitations. In *12th International Conference on Experimental Mechanics, 29 August - 2 September, 2004*. Politecnico di Bari, Italy, 2004, 8 p.
25. Errapart, A., Aben, H., Ainola, L. Photoelastic tomography in linear approximation. In *Proceedings of the 2004 SEM X International Congress and Exposition on Experimental and Applied Mechanics, June 7 - 10, 2004*, SEM, Costa Mesa, California, 2004, 8 p.
26. Anton, J., Errapart, A., Aben, H. Measurement of tempering stresses in axisymmetric glass articles. *International Journal Forming Processes*, 2004, **7**(4), 543 - 554.
27. Aben, H., Errapart, A., Ainola, L., Anton, J. Photoelastic tomography for residual stress measurement in glass. In *Optical Metrology in Production Engineering: Bellingham, Washington: SPIE, 2004*, Proceedings of SPIE, **5457**, 1-11.
28. Aben, H., Errapart, A., Ainola, L., Anton, J. Photoelastic tomography in linear approximation. In *Proceedings of ATEM'03 : International Conference on Advanced Technology in Experimental Mechanics 2003, September 10-12, 2003, Nagoya, Japan* (JSME No. 03-207). The Japan Society of Mechanical Engineers, Tokyo, 2003, Paper OS01W0036, 6 p.
29. Aben, H., Anton, J., Errapart, A. Automatic measurement of residual stress in glass articles of complicated shape. *Verre*, 2003, **9**(3), 44 - 49.

30. Aben, H., Anton, J., Errapart, A. Modern photoelastic technology for residual stress measurement in glass. In *XIX A.T.I.V. Conference "Quality and Process Control as Fundamental Means for the Improvement and Development of Glass Manufacturing", Parma (Italy), 26th September, 2003*, Italy, 2003, 88-97.
31. Aben, H., Anton, J., Errapart, A. Measurement of tempering stresses in axisymmetric glass articles. In *Modelling of Glass Forming and Tempering 2002 : Proceedings of the 2nd International Colloquium: Valenciennes, France, 23 - 24 - 25 January 2002*.Presses Universitaires de Valenciennes, Valenciennes, 2002, 276-282.
32. Aben, H., Anton, J., Errapart, A. Integrated photoelasticity for residual stress measurement in glass articles of complicated shape. *In 2002 Glass Odyssey: 6th ESG Conference: June 2-6, 2002*, Montpellier, France, 2002, 5-282.
33. Aben, H., Anton, J., Errapart, A. Automatic residual stress measurement in glass products of complicated shape. *International Glass Review*, 2002, **2**, 181-184.
34. Aben, H., Anton, J., Errapart, A. Residual stress measurement in axisymmetric glass articles. *Glass Technology*, 2002, **43C**, 278 - 282.
35. Aben, H., Ainola, L., Anton, J. Errapart, A. Integraalne fotoelastsusmeetod klaastoodete kvaliteedi kontrollimiseks. In *Teadusmõte Eestis : tehnikateadused* (Engelbrecht, J., Küttner, R., eds.). Eesti Teaduste Akadeemia., Tallinn, 2002, 9-13.
36. Aben, H., Ainola, L., Anton, J., Errapart, A. *Détermination des contraintes dans les préformes optiques à saut d'indice. In: Colloque Photomechanique 2001: Journées organisées les 24, 25 et 26 avril 2001 à Poitiers*. (Berthaud, Y, ed.). GAMAC, Poitiers, 2001, 71-78.
37. Aben, H., Anton, J., Errapart, A. Residual stress measurement in axisymmetric glass articles. In *[Proceedings] XIX International Congress on Glass: Extended Abstracts, Edinburgh, Scotland, 1-6 July 2001*. Edinburgh, 2001, 242-243.

Abstract

In this thesis, four new algorithms of photoelastic tomography, opening new possibilites for the determination of 3D stress fields, are described. Use of linear approximation assumes small values of the birefringence or small angles of rotation of principal stress axis along the light rays; the non-linear approach is free of these restrictions.

Practical realization of photoelastic tomography in linear approximation for reconstruction of normal components of 3D stress fields is described.

In the case of axisymmetric stress fields, it is shown that the Abel inversion can be used for the determination of axial and shear components of an axisymmetric stress field.

In order to determine the radial and circumferential stress component, the equilibrium equation and the compatibility equation from the theory of elasticity (in the case of external loads) or the generalized sum rule from the theory of thermoelasticity (in the case of residual stresses) are employed. The stability of solutions to these equations has been analysed both analytically and numerically, and, numerical algorithms for solving these equations have been elaborated. In the case of external loads, the numerical algorithm has been validated by using the analytical solution to the Hertzian contact problem.

A non-linear algorithm of photoelastic tomography for the measurement of axisymmetric stress fields has been elaborated. Stress components are presented in the form of power series along the radial coordinate. A differential evolution algorithm has been used for finding the stress field parameters, which fit the measurement data best.

Application of the described methods have been illustrated by practical examples.

Kokkuvõte

Selles väitekirjas kirjeldatakse fotoelastsustomograafia nelja uut algoritmi, mis avavad uusi võimalusi ruumiliste pingeväljade täielikuks määramiseks. Lineaarse lähenduse kasutamine eeldab väikeseid käiguvahesid või väikeseid peapingete pöördumisi valguskiirte teel; mittelineaarne lähenemine on nendest piirangutest vaba.

On kirjeldatud fotoelastsustomograafia lineaarse lähenduse praktilist realisatsiooni kolmemõõtmeliste pingeväljade määramiseks.

On näidatud, et Abeli inversiooni saab kasutada telgsümmeetriliste pingeväljade teljesihilise ja nihkepinge komponentide määramiseks.

Radiaal- ja rõngaspinge määramiseks telgsümmeetrilisel juhul kasutatakse elastsusteooriast tasakaaluvõrrandit ja kas pidevusvõrrandit (väliskoormuse juhul) või termoelastsuse teooriast üldistatud summareeglit (jääkpingete juhul). Analüütiliselt ja numbriliselt on uuritud nende võrrandite lahendite stabiilsust ja on välja töötatud numbrilised algoritmid nende võrrandite lahendamiseks. Numbrilist algoritmi väliskoormuse juhul on kontrollitud Hertzi kontaktprobleemi analüütilise lahendi abil.

On välja töötatud mittelineaarne fotoelastsustomograafia algoritm telgsümmeetriliste pingeväljade määramiseks. Pingete komponendid on esitatud radiaalkoordinaadi sihilise astmerea kujul. Mõõteandmetega kõige paremini sobivate pingevälja parameetrite leidmiseks on kasutatud diferentsiaalse evolutsiooni algoritmi.

Kirjeldatud meetodite rakendust on illustreeritud praktiliste näidete varal.

Appendix 1: Publications

Paper I

Aben, H., Ainola, L., Errapart, A. Application of the Abel inversion in case of a tensor field. *Inverse Problems in Science and Engineering*, 2010, **18**(2), 241-249.

Inverse Problems in Science and Engineering
Vol. 18, No. 2, March 2010, 241–249

Taylor & Francis
Taylor & Francis Group

Application of the Abel inversion in case of a tensor field

Hillar Aben*, Leo Ainola and Andrei Errapart

Institute of Cybernetics, Tallinn University of Technology, 21 Akadeemia tee, 12618 Tallinn, Estonia

(*Received 13 February 2009; final version received 4 November 2009*)

Abel's integral equations arise in many areas of natural science and engineering, particularly in plasma diagnostics. The axisymmetric physical field is determined using the Abel inversion. Until now, the Abel inversion has been applied almost exceptionally for the determination of scalar fields, i.e. fields, which at a point are characterized by a scalar. In several areas of engineering, the need to determine axisymmetric tensor fields arises, for example by measuring residual stress in axisymmetric glass articles with photoelasticity. In this article, we show how the Abel inversion can be used for the determination of an axisymmetric stress tensor field. The peculiarity in determining the tensor field is that on every ray two integrals of the field are measured and for complete determination of all the components of the stress tensor, equations of the theory of elasticity are used. The method is illustrated by an example.

Keywords: Abel inversion; tensor field; photoelasticity; stress analysis; residual stress

1. Introduction

Abel inversion is a popular technique by which various axisymmetric physical fields are investigated, particularly in plasma diagnostics [1–3]. This technology has been applied almost without exception for the determination of scalar fields. At the same time, in physics and engineering, the problem of measuring axisymmetric tensor fields often arises.

In particular cases of photoelastic stress analysis, some stress tensor components can be directly determined with the Abel inversion; for example, by stress measurement in a cylindrical body with no stress gradient in axial direction [4,5]. This problem is important by assessing the quality of optical fibres. The basic equation of photoelasticity can be written as

$$\Delta = C_0(\sigma_1 - \sigma_2)t, \tag{1}$$

where C_0 is the photoelastic constant, σ_1 and σ_2 are principal stresses in the plane perpendicular to the polarized light beam, t is the thickness of the specimen and Δ is optical retardation between light vibrations along the directions of σ_1 and σ_2.

Let us consider passing of polarized light through the cross-section of a cylindrical body with no stress gradient in the direction of its z-axis (Figure 1). In cylindrical

*Corresponding author. Email: aben@cs.ioc.ee

ISSN 1741 5977 print/ISSN 1741 5985 online

DOI: 10.1080/17415970903545124
http://www.informaworld.com

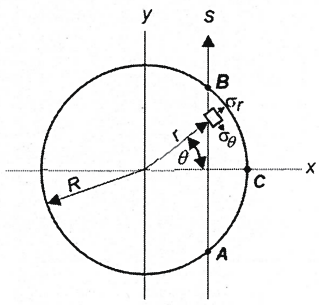

Figure 1. Passing light through the cylinder parallel to the y-axis.

coordinates, stress in the cylinder is determined by three stress components: σ_r, σ_θ and σ_z. Due to the photoelastic effect, the cylinder becomes birefringent. One principal birefringence direction (and principal stress direction) is in the radial direction and the other is parallel to the z-axis.

If the polarized light is passed through the cylinder parallel to the y-axis (Figure 1, ray s), optical retardation $\Delta(x)$ can be expressed as

$$\Delta(x) = C_0 \int_A^B (\sigma_z - \sigma_r \cos^2\theta - \sigma_\theta \sin^2\theta)\mathrm{d}y. \tag{2}$$

Equation (2) follows from Equation (1) using notations

$$\sigma_1 = \sigma_z, \quad \sigma_2 = \sigma_x = \sigma_r \cos^2\theta + \sigma_\theta \sin^2\theta. \tag{3}$$

From the condition of equilibrium of the three-dimensional segment ABC of the thickness h, we have the following:

$$h \int_A^B (\sigma_r \cos^2\theta + \sigma_\theta \sin^2\theta)\mathrm{d}y = 0. \tag{4}$$

Equation (4) was first derived by Poritsky [6]. Physically, Equation (4) means that since the external boundary of the cylinder is free of loads, due to the equilibrium condition in the x direction, integral of the stress σ_x along the line AB must be equal to zero.

Now from Equation (2) follows

$$\Delta(x) = C_0 \int_A^B \sigma_z \,\mathrm{d}y. \tag{5}$$

Since $\mathrm{d}y$ can be expressed as

$$\mathrm{d}y = \frac{r\,\mathrm{d}r}{\sqrt{r^2 - x^2}}, \tag{6}$$

Equation (5) can be written in the form

$$\Delta(x) = 2C_0 \int_x^R \frac{\sigma_z(r) r}{\sqrt{r^2 - x^2}} \mathrm{d}r. \tag{7}$$

The solution of this integral equation is given by

$$\sigma_z(r) = -\frac{1}{\pi C_0}\int_r^R \frac{\frac{\mathrm{d}}{\mathrm{d}x}\Delta(x)}{\sqrt{x^2 - r^2}}\mathrm{d}x. \tag{8}$$

Thus, radial distribution of one component of the stress tensor, $\sigma_z(r)$, can be determined directly with Abel inversion.

The problem of measuring stress in cylindrical bodies arises by investigating residual stress in glass cylinders, fibres and fibre preforms. In this case, the so-called sum rule [4,7]

$$\sigma_z = \sigma_r + \sigma_\theta \tag{9}$$

is valid.

On the basis of the sum rule and of the equation of equilibrium,

$$\frac{\mathrm{d}}{\mathrm{d}r}(r\sigma_r) - \sigma_\theta = 0, \tag{10}$$

the other stress components can be determined [8], i.e.

$$\sigma_r(r) = \frac{1}{r^2}\int_0^r \sigma_z(r) r\,\mathrm{d}r, \tag{11}$$

$$\sigma_\theta(r) = \sigma_z(r) - \sigma_r(r). \tag{12}$$

Thus, all the stress tensor components have been determined. This method has been widely used by measuring stress in optical fibres and fibre preforms [8–10].

If the specimen has general axisymmetric shape and the stresses vary along the z-axis, Abel inversion cannot be applied directly. In this case, the stresses are usually approximated by certain functions (e.g. polynomials), the unknown coefficients of which are directly calculated from the experimental data [11,12]. The aim of this article is to show that also in the general case of the measurement of axisymmetric stress with integrated photoelasticity [13,14], the Abel inversion can be applied.

2. The general case of axisymmetric stress distribution

Let us consider determination of the stresses in an axisymmetric transparent object in the case when stresses vary in the direction of the z-axis. The state of stress in a section $z = z_0$ is determined by the stress tensor components σ_r, σ_θ, σ_z and τ_{rz}. Let us assume that photoelastic measurements are carried out in two parallel cross-sections of the test object, at $z = z_0$ and $z = z_0 + h$ (Figure 2). The value of h depends on the stress gradient in the direction of the z-axis and on the precision of the measurements. It is important to reveal information about the stress gradient along the z-axis with sufficient precision.

In the case of the absence of stress gradient in the z direction, by photoelastic measurements, only optical retardation $\Delta(x)$ is recorded since one of the principal directions is parallel to the z-axis, and therefore the principal stress directions are constant on the light ray. In the general case, when the shear stress τ_{rz} is present, the principal stress directions on the ray s are not constant and actually a rotation of the principal stress directions along the light ray takes place. Due to that optical phenomena are complicated and they are considered in integrated photoelasticity [13,14].

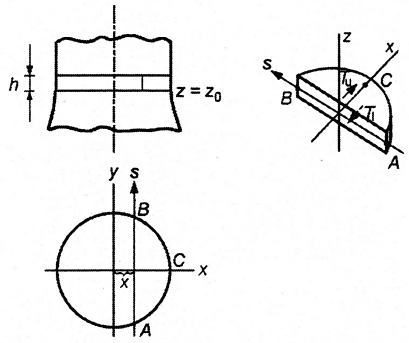

Figure 2. Investigating an axisymmetric test object in the general case.

Let us assume that the birefringence of the test object is weak. In this case, optical phenomena can be treated in a simplified way [15,16]. By weak birefringence we mean the case when optical retardation $\Delta(x)$ is less than about a third of the wavelength. In the case of weak birefringence, the refraction indices n_1 and n_2 in the direction of the principal stresses σ_1 and σ_2 are close to each other ($n_1 - n_2 \lesssim 10^{-3}$). It has been shown [15] that in this case by photoelastic measurements in section $z = z_0$ on every light ray, the parameter of the isoclinic $\varphi(x)$ and optical retardation $\Delta(x)$ can be measured and they are related to the integrals of the components of the stress tensor as

$$V_1(x) = \Delta \cos 2\varphi = C_0 \int_A^B (\sigma_z - \sigma_x) \mathrm{d}y, \tag{13}$$

$$V_2(x) = \Delta \sin 2\varphi = 2C_0 \int_A^B \tau_{zx} \, \mathrm{d}y. \tag{14}$$

Let us mention that the main area of the application of integrated photoelasticity is the measurement of residual stress in glass [16]. Due to low photoelastic constant C_0 of glass, in glass articles often the birefringence is weak.

Measurements are also carried out in the auxiliary section $z = z_0 + h$. We denote by $V_1'(x)$ and $V_2'(x)$ the measurement data in the auxiliary section.

Let us consider equilibrium of the three-dimensional segment ABC (Figure 2) in the direction of the x-axis. We may write

$$h \int_A^B \sigma_x \mathrm{d}y = T' - T, \tag{15}$$

where T' and T are shear forces on the upper and lower surfaces of the segment, respectively,

$$T' = \frac{1}{2C_0} \int_x^R V_2' \mathrm{d}x, \quad T = \frac{1}{2C_0} \int_x^R V_2 \mathrm{d}x. \tag{16}$$

Taking into consideration the relationships (15) and (16), Equation (13) reveals that

$$C_0 \int_A^B \sigma_z \, dy = V_1 + \frac{1}{2h}\left(\int_x^R V_2' \, dx - \int_x^R V_2 \, dx\right) = I(x). \tag{17}$$

From Equation (17), the distribution of the axial stress can be determined using the Abel inversion as

$$\sigma_z(r) = -\frac{1}{\pi C_0} \int_r^R \frac{\frac{d}{dx} I(x)}{\sqrt{x^2 - r^2}} dx. \tag{18}$$

Equation (14) can be written in the form

$$V_2(x) = \Delta \sin 2\varphi = 2C_0 \int_A^B \tau_{rz} \cos\theta \, dy. \tag{19}$$

or

$$\frac{V_2(x)}{x} = 2C_0 \int_A^B \frac{\tau_{rz}}{r} dy. \tag{20}$$

From Equation (20), the distribution of the shear stress can be determined using the Abel inversion

$$\tau_{rz} = -\frac{r}{2\pi C_0} \int_r^R \frac{\frac{d}{dx}\left(\frac{V_2(x)}{x}\right)}{\sqrt{x^2 - r^2}} dx. \tag{21}$$

If σ_z and τ_{rz} are known, the stress components σ_r and σ_θ can be determined from the equation of equilibrium

$$\frac{\partial \sigma_r}{\partial r} + \frac{\sigma_r - \sigma_\theta}{r} + \frac{\partial \tau_{rz}}{\partial z} = 0 \tag{22}$$

and from the generalized sum rule [17,18]

$$\sigma_r + \sigma_\theta = \sigma_z - 2 \int_0^r \frac{\partial \tau_{rz}}{\partial z} dr + D, \tag{23}$$

where D is an integration constant. Equation (23) is to be used when measuring residual stress in glass. If stresses are caused by a mechanical load, instead of Equation (23) the compatibility equation

$$\frac{\partial}{\partial r}[\sigma_\theta - \mu(\sigma_z + \sigma_r)] - (1 + \mu)\frac{\sigma_r - \sigma_\theta}{r} = 0 \tag{24}$$

is to be used. Here μ is the Poisson coefficient.

Thus in the general case of the axisymmetric stress tensor field, the axial stress σ_z and shear stress τ_{zz} distributions are determined from the measurement data with Abel inversion. The other stress components σ_r and σ_θ are determined from the equations of the theory of elasticity. However, in order to use the Abel inversion for the calculation of the stress tensor components, the direct measurement data are to be modified and data from two parallel sections are to be used.

Let us mention that the onion-peeling method [19], a numerical algorithm equivalent to the Abel inversion, can also be used by measuring axisymmetric stress tensor fields [20,21].

3. Example

Let us consider measurement of the residual stress in the lower part of the stem of a wine glass (Figure 3). Figure 4 shows distribution of the optical retardation $\Delta(x)$ and azimuth of the first principal stress $\varphi(x)$ in the section B–B, which is located at $z = 16.61$ mm from the lower end of the wine glass. Auxiliary section of photoelastic measurements was located at $z + h = 17.61$ mm.

Figure 5 shows distribution of the axial stress σ_z, obtained with Abel inversion from Equation (18), using the onion-peeling method. For comparison, distribution of σ_z,

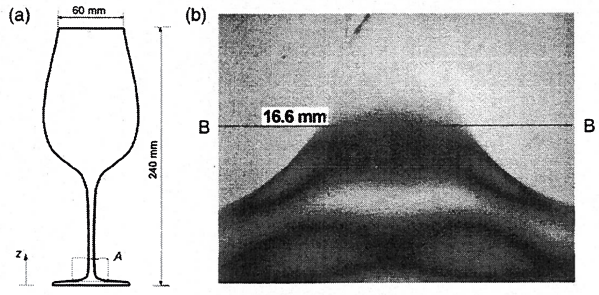

Figure 3. (a) Geometry of the wine glass and (b) and fringe pattern in the area A.

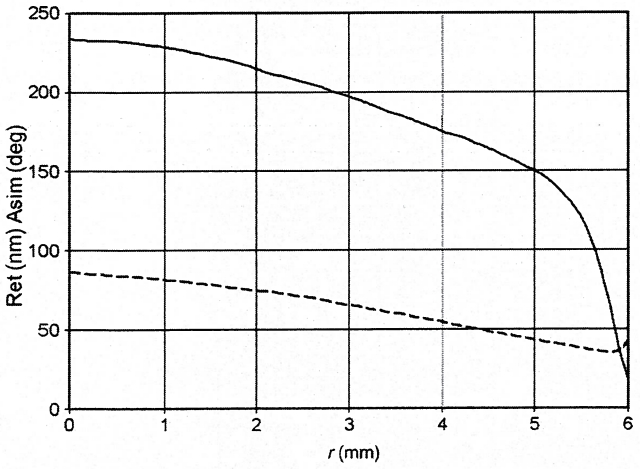

Figure 4. Radial distribution of optical retardation $\Delta(x)$ (——) and azimuth of the first principal stress $\varphi(x)$ (– – –) in section $z = 16.61$ mm.

obtained with standard technology of integrated photoelasticity [13,16], is also shown (σ_z has been approximated as a polynomial with three terms). Distribution of stress components σ_r and σ_θ was determined using the equilibrium equation (22) and the generalized sum rule (23) (Figure 6). All stress components are approximated as polynomials with three terms.

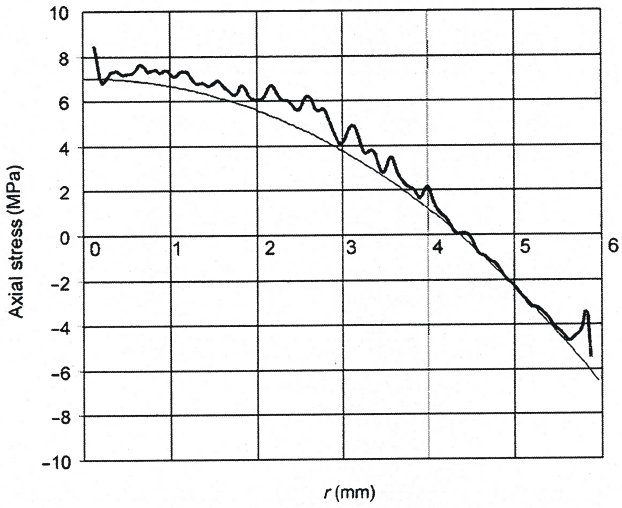

Figure 5. Axial stress σ_z distribution, obtained with the onion-peeling method (—) and with polynomial approximation (——).

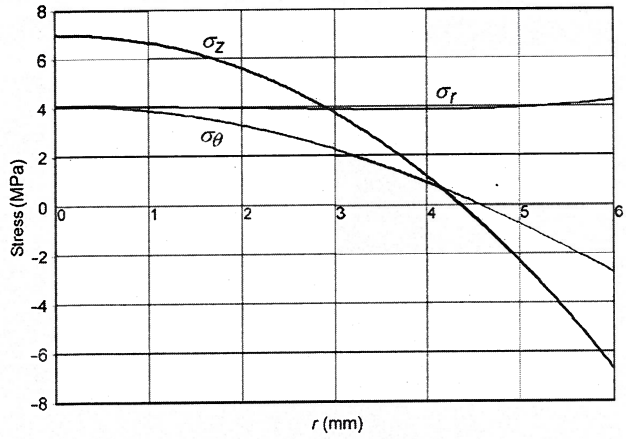

Figure 6. Normal stress components in section B–B.

In the case of residual stresses, the average stress in any section should be zero. The average value of the axial stress σ_z, shown in Figure 6, is 0.27 MPa. That makes less than 4% of the maximum value of σ_z. That is an indication of precision of determining the axial stress.

4. Conclusions

It has been shown that the Abel inversion, which is essentially the method for determining scalar fields, can also be applied by investigating tensor fields. The particular case of residual stress measurement in an axisymmetric glass article with integrated photoelasticity has been considered. In this case, on every light ray, two integrals of the stress tensor components can be measured and measurements are to be carried out in two parallel sections. From these measurement data, the Abel integral equations (18) and (21) for the axial stress and shear stress can be constructed. A peculiarity of the tensor field measurement, in this particular case, is the possibility to use equations of the theory of elasticity as *a priori* information. Due to that, the stress tensor field can be completely determined. The developed algorithm is illustrated by measuring residual stresses in the stem of a wine glass. An area of application of the generalized Abel inversion is residual stress measurement in axisymmetric glass articles with integrated photoelasticity.

Acknowledgements

The authors appreciate the support of the Estonian Science Foundation (grant No. 7840).

References

[1] H.R. Griem, *Plasma Spectroscopy*, McGraw-Hill, New York, 1964.
[2] K. Bockasten, *Transformation of observed radiances into radial distribution of the emission of a plasma*, J. Opt. Soc. Am. 51(9) (1961), pp. 913–947.
[3] R.K. Paul, J.T. Andrews, K. Bose, and P.K. Barhai, *Reconstruction errors in Abel inversion*, Plasma Devices Oper. 13(4) (2005), pp. 281–289.
[4] R.C. O'Rourke and A.W. Saenz, *Quenching stresses in transparent isotropic media and the photoelastic method*, Quart. Appl. Math. 8(3) (1950), pp. 303–311.
[5] P.M. Sutton, *Stress measurement in circular cylinders*, J. Am. Ceram. Soc. 41(3) (1958), pp. 103–109.
[6] H. Poritsky, *Analysis of thermal stresses in sealed cylinders and the effect of viscous flow during anneal*, Physics 5(12) (1934), pp. 406–411.
[7] R.C. O'Rourke, *Three-dimensional photoelasticity*, J. Appl. Phys. 22(7) (1951), pp. 872–878.
[8] W. Urbańczyk and K. Pietraszkiewicz, *Measurements of stress anisotropy in fiber perform: Modification of the dynamic spatial filtering technique*, Appl. Opt. 27(19) (1988), pp. 4117–4122.
[9] P.L. Chu and T. Whitbread, *Measurement of stresses in optical fiber and perform*, Appl. Opt. 21(23) (1982), pp. 4241–4245.
[10] B.E. Briley, *An Introduction to Fiber Optics System Design*, North-Holland, Amsterdam, 1988.
[11] J.F. Doyle and H.T. Danyluk, *Integrated photoelasticity for axisymmetric problems*, Exp. Mech. 18(6) (1978), pp. 215–220.
[12] J.F. Doyle, *Closed-form inversion of the axisymmetric integrated photoelasticity equations*, J. Appl. Mech. 47(6) (1980), pp. 431–433.
[13] H. Aben, *Integrated Photoelasticity*, McGraw-Hill, New York, 1979.

[14] H. Aben, *Characteristic directions in optics of twisted birefringent media*, J. Opt. Soc. Am. A3(9) (1986), pp. 1414–1421.
[15] H.K. Aben, J.E. Josepson, and K.-J.E. Kell, *The case of weak birefringence in integrated photoelasticity*, Optics Lasers in Eng. 11(3) (1989), pp. 145–157.
[16] H. Aben and C. Guillemet, *Photoelasticity of Glass*, Springer, Berlin, 1993.
[17] L. Ainola and H. Aben, *Hybrid mechanics for axisymmetric thermoelasticity problems*, J. Therm. Stresses 23(7) (2000), pp. 685–697.
[18] L. Ainola and H. Aben, *A new relationship for the experimental-analytical solution of the axisymmetric thermoelasticity problem*, ZAMM 84(3) (2004), pp. 211–215.
[19] C.J. Dash, *One-dimensional tomography: a comparison of Abel, onion-peeling, and filtered backprojection methods*, Appl. Opt. 31(8) (1992), pp. 1146–1152.
[20] J. Anton, A. Errapart, H. Aben, and L. Ainola, *A discrete algorithm of integrated photoelasticity for axisymmetric problems*, Exp. Mech. 48(5) (2008), pp. 613–620.
[21] J. Anton and A. Errapart, *Generalized Onion-Peeling Method in Integrated Photoelasticity of Axisymmetric Problems*, in *Proceedings of 13th International Conference on Experimental Mechanics*, E.E. Gdoutos, ed., Springer, Alexandroupolis, 2007, pp. 95–96.

Paper II

Errapart, A. On the technology of photoelastic tomography. *Experimental Techniques*, 2008, **32**(1), 31 - 35.

ON THE TECHNOLOGY OF PHOTOELASTIC TOMOGRAPHY

One of the ambitions of experimental mechanics has been the development of nondestructive methods for the measurement of three-dimensional (3D) stress fields. Certain possibilities for that opens the photoelastic scattered light method.[1,2] However, due to complicated apparatus and difficulties with interpreting the measurement results, this method has had rather limited application. Integrated photoelasticity[3] has been applied almost exceptionally for the measurement of axisymmetric stress fields[4,5] because in the general case solution of the inverse problem is mathematically complicated. Application of traditional tomographic techniques[6,7] in stress analysis is not possible (at least not directly) since stress is a tensor and tensor field tomography is not sufficiently developed. Sharafutdinov[8,9] has shown that using a linearized solution of the equations of integrated photoelasticity, it is possible to construct a tomographic algorithm for the measurement of the normal stress distribution in a 3D stress field. This method was further developed and practically implemented by Aben et al.[10–13] In this article, practical realization of photoelastic tomography is described. Application of this technology is illustrated by stress measurement in a high-pressure electric lamp.

LINEAR APPROXIMATION IN PHOTOELASTIC TOMOGRAPHY

Let us consider passing of polarized light through a 3D photoelastic specimen parallel to the y'-axis (Fig. 1). We assume that in two parallel sections, main section at $z = z_0$ and auxiliary section at $z = z_0 + \Delta z$, the parameter of the isoclinic φ and the integrated optical retardation Δ have been measured for many azimuths β (Fig. 1). Let us define integrals of stress components on the optical path, V_1 and V_2, as functions of Δ, φ as follows:

$$V_1 = \Delta\cos 2\varphi = C\int (\sigma_{x'} - \sigma_{z'})\mathrm{d}y', \tag{1}$$

$$V_2 = \Delta\sin 2\varphi = 2C\int \tau_{x'z'}\mathrm{d}y'. \tag{2}$$

The values of V_1 and V_2 in the auxiliary section $z = z_0 + \Delta z$, we denote V_1 and V'_1.

It is assumed that for tomographic measurements, the specimen is rotated around the z-axis.

Equations 1 and 2 express the solution of the equations of integrated photoelasticity in linear approximation.[4,9,14] Linear approximation is valid if birefringence is weak (optical retardation is less than about one third of the wavelength) or the rotation of the principal stress axes is small. If no rotation of the principal stresses is present, Eqs. 1 and 2 are valid for arbitrary birefringence. These formulas have been widely used by measuring stress in axisymmetric glass articles.[4,5]

The problem of tensor field tomography can be reduced to a problem of scalar field tomography for a single stress component σ_z as follows.[4,10,11] Considering the equilibrium of the 3D segment ABC in the direction of the x'-axis (Fig. 1), we may write

$$\Delta z\int_A^C \sigma_{x'}\mathrm{d}y' = T_\mathrm{u} - T_\mathrm{l}, \tag{3}$$

where T_u and T_l are the shear forces on the upper and lower surfaces of the segment, respectively:

$$T_\mathrm{u} = \frac{1}{2C}\int_l^B V'_2\ \mathrm{d}x',\ T_\mathrm{l} = \frac{1}{2C}\int_l^B V_2\mathrm{d}x'. \tag{4}$$

Taking into consideration relationships Eqs. 3 and 4, Eq. 1 reveals that

$$\int_A^C \sigma_z\mathrm{d}y' = \frac{1}{2C\Delta z}\left(\int_l^B V'_2\mathrm{d}x' - \int_l^B V_2\mathrm{d}x'\right) - \frac{V_1}{C}. \tag{5}$$

Since tomographic photoelastic measurement data can be obtained for all the light rays y', Eq. 5 expresses the Radon transform[6,7] of the field of the stress σ_z. The field of σ_z can be determined using any of the well-known Radon inversion techniques.[6,7] Rotating the specimen by tomographic measurements around the axes x and y, fields of σ_x and σ_y can also been determined.

Let us sum up essential features of the photoelastic tomography in linear approximation:

(1) Determination of the stress field is decomposed to the measurement of a single stress component at a time.
(2) For the measurement of the field of a single stress component, the specimen is rotated around only one axis.
(3) Distribution of the normal stress in a section of the specimen is determined with the method of scalar field tomography using Radon inversion.
(4) By tomographic photoelastic measurements, the parameter of the average isoclinic φ and the integral optical retardation Δ are to be measured in two parallel sections. Thus, the photoelastic measurements are similar to those used by investigating 2D problems.
(5) The main difference of the tomography of a single component of the stress tensor from the scalar field tomography is in the following. In classical tomography, the Radon transform of the field is directly measured. In case of the stress field tomography, the Radon transform of the normal stress σ_z in Eq. 5 is calculated using photoelastic measurement data in two parallel sections.

A. Errapart is a researcher in the Laboratory of Photoelasticity, Institute of Cybernetics, at Tallinn Technical University, Tallinn, Estonia.

doi: 10.1111/j.1747-1567.2007.00222.x

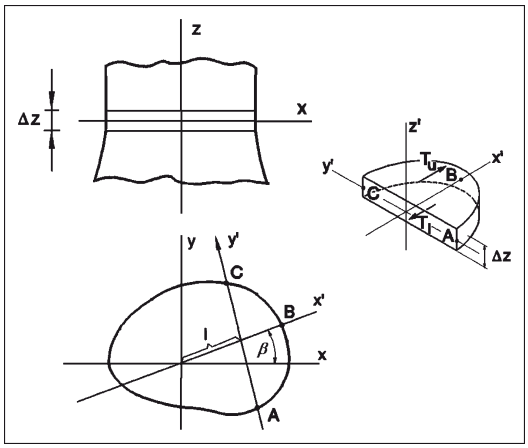

Fig. 1: Illustration, explaining the derivation of Eq. 5

RECONSTRUCTION OF THE STRESS FIELD

Since the Radon transform of the axial stress, σ_z, is determined through the measurement data according to Eq. 5, any method of Radon inversion can be used to determine the field of σ_z. It is necessary to measure the projection data for many values of the angle β over 180° (Fig. 1). Let us write Eq. 5 in the form:

$$\int_A^C \sigma_z \mathrm{d}y' = W(\xi,\beta), \tag{6}$$

where $W(\xi, \beta)$ is determined from Eq. 5.

It is assumed that the cross-section of the specimen is located inside a unit circle. Following the method proposed by Cormack,[15] $W(\xi, \beta)$ is expressed in the form of the Fourier series as follows:

$$W(\xi,\beta) = F_0(\xi) + \sum_{m=1}^{M} \left(F_m^c(\xi)\cos m\beta + F_m^s(\xi)\sin m\beta \right). \tag{7}$$

The distribution of the axial stress, σ_z, is also expressed as a Fourier series as follows:

$$\sigma_z = f_0(\rho) + \sum_{m=1}^{M} \left(f_m^c(\rho)\cos m\theta + f_m^s(\rho)\sin m\theta \right), \tag{8}$$

where M is the number of terms. Higher value of M gives better approximation along the angular coordinate.

Now the Cormack transform reveals that

$$F_m^{c,s}(\xi) = 2\int_\xi^1 \frac{f_m^{c,s}(\rho)T_m(\xi/\rho)\rho \mathrm{d}\rho}{\sqrt{\rho^2-\xi^2}}, \tag{9}$$

where $T_m(\xi/\rho)$ are the Chebyshev polynomials[16] of the first kind.

If the functions $F_m^{c,s}$ and $f_m^{c,s}$ are orthogonal polynomials in the interval (0, 1), it is possible to avoid integration in Eq. 9. Cormack[15] has used the following related pair of orthogonal polynomials as follows:

$$f_m(\rho) = \sum_{l=0}^{L} a_m^l (m+2l+1) Z_m^l(\rho), \tag{10}$$

$$F_m(\xi) = 2\sum_{l=0}^{L} a_m^l \sin[(m+2l+1)\arccos\xi], \tag{11}$$

where $Z_m^l(\rho)$ is a modification of the Zernicke polynomials[17] in the following form:

$$Z_m^l(\rho) = \sum_{s=0}^{l} \frac{(-1)^s (m+2l-s)! r^{m+2l-2s}}{s!(m+l-s)!(l-s)!}, \tag{12}$$

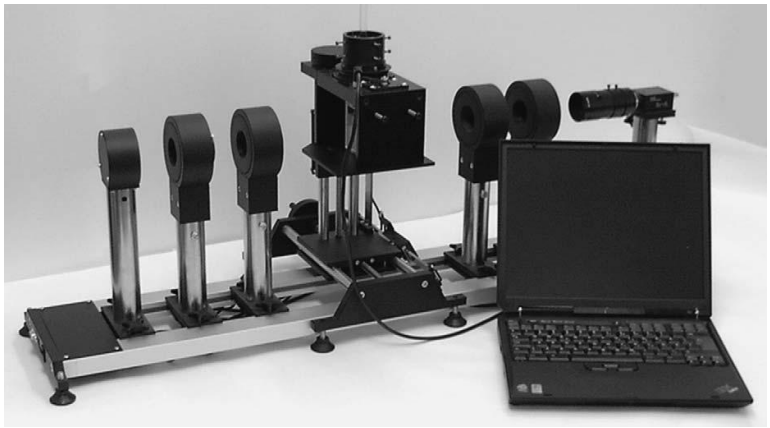

Fig. 2: Computer-controlled polariscope AP-04 SM. In the middle is the rotary stage with an optical fiber preform

and L is the number of terms. Higher value of L gives better approximation along the radial coordinate.

Determination of σ_z is divided into three steps:

(1) Determination of functions $F_m^{c,s}$ from Eq. 7 for every point of measurement i ($i = 1 \ldots N$) by using the discrete Fourier transform; here, N denotes the number of measurements on the radius.
(2) Approximation of $F_m(\xi)$ with a polynomial (Eq. 11) and determination of the coefficients a_m^l using the least squares method.
(3) Calculation of σ_z using Eqs. 8 and 10.

EXPERIMENTAL TECHNIQUE

Photoelastic measurements were carried out with an automatic polariscope AP-04 SM (Fig. 2) manufactured at the Laboratory of Photoelasticity of the Institute of Cybernetics of the Tallinn University of Technology (Tallinn, Estonia). As light source, light-emitting diodes of $\lambda = 640$ nm have been used. Polariscope contains two polaroids and two quarter-wave plates that all are controlled by stepper motors. Optical information is recorded by a charge coupled device (CCD) camera. The polariscope can be used as a dark-field or light-field circular polariscope, and it permits measurements of optical retardation and parameter of the isoclinic with the phase-stepping method.[18,19] Polariscope AP-04 SM is controlled by an IBM Thinkpad (Armonk, NY).

For automatic rotation of specimens of small size, a rotary stage has been constructed (Fig. 3). Rotation is accomplished with a stepper motor, which permits rotation of the specimen with a precision of 0.1°. The specimen is fixed to the rotary stage so that the part of the specimen, which is investigated, is placed in an immersion tank. Immersion liquid provided by Cargille-Sacher Laboratories Inc. (Cedar Grove, NJ) is recommended because of its relative safety when compared to alpha-bromonaphtalene and fast mixing when compared to silicon oils.

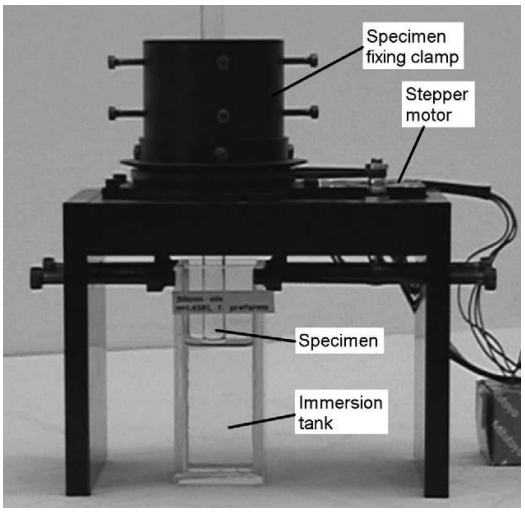

Fig. 3: Rotary stage for automatic rotation of small test objects

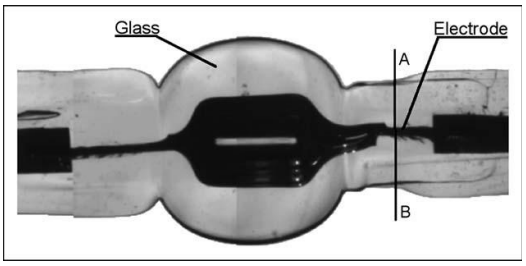

Fig. 4: Geometry of the high-pressure electric lamp

Photoelastic measurements with the phase-stepping method for one projection take about 15 s. For every projection, from 40 to 100 measurement points per millimeter are obtained.

A menu-driven program SIGMAZ has been elaborated that implements the following:

- control of the polariscope AP-04 SM, including the CCD camera and the rotary stage,
- determination of the direction of the first principal stress σ_1 and the optical retardation with the phase-stepping method[18,19] for many values of the angle β over 180° with optional recording of photos of the specimen in the light-field circular polariscope,
- extraction of projection data in selected main and auxiliary section,
- extraction of projection data from the photos of the specimen in the format suitable for program CTSim,[20]
- removal of the wobbling of the specimen axis,
- stress field reconstruction algorithm described previously, and
- plotting of color-coded stress field with the optional application of contour masks.

EXAMPLE

As an example, we describe measurement of the normal stress distribution in section AB of the stem of a high-pressure electric lamp made of quartz glass with refraction index of 1.47 and $C = 3.40$ TPa^{-1} (Fig. 4). In the axisymmetric middle part of the lamp stresses can be determined with conventional integrated photoelasticity.[3]

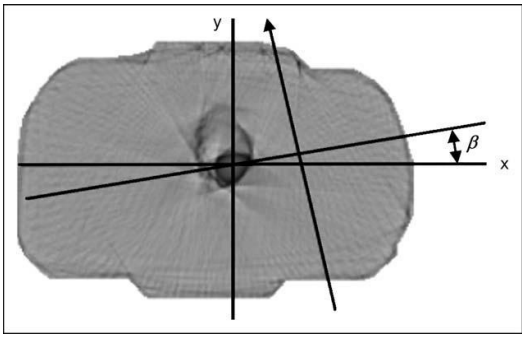

Fig. 5: Geometry of the cross-section AB

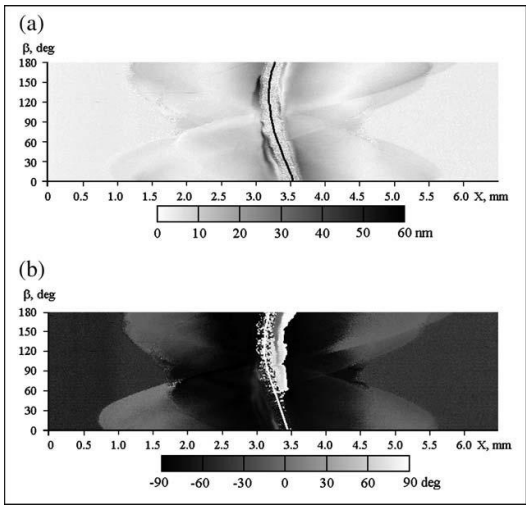

Fig. 6: Projections of (a) Δ and (b) φ in section AB for β = 0–180°

Refraction index of the immersion liquid was also 1.47 to avoid refraction. One hundred eighty projections were recorded, with a step $\Delta\beta = 1°$. In addition to the photoelastic data, a photo of the specimen in a light-field circular polariscope was also recorded for every projection angle. Contour of the cross-section AB (Fig. 5) was obtained by using filtered backprojection method[6,7] in the program CTSim[20] on these photos. Projections of photoelastic data for stress field reconstruction were extracted in two sections, the main section being AB and the auxiliary section at 1 mm apart from it. Since processing of projections from theses sections were similar, only data for the main section will be shown. Figure 6a shows projections of optical retardation Δ, and Fig. 6b projections of the isoclinic angle φ (direction of σ_1) in section AB. The electrode looks deformed in Fig. 6a and b because it did not coincide with the rotation axis of the specimen.

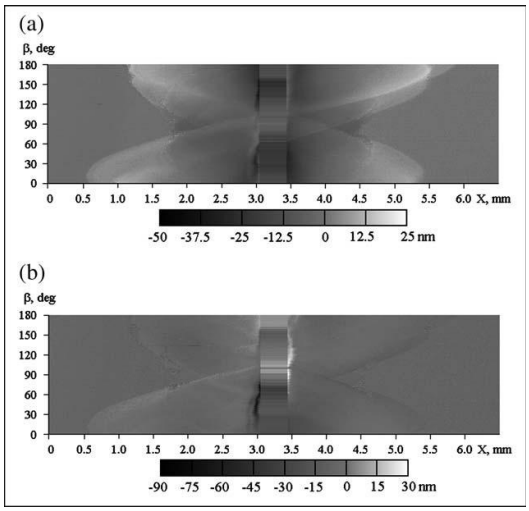

Fig. 7: Projections of (a) Δcos 2φ and (b) Δsin 2φ in section AB

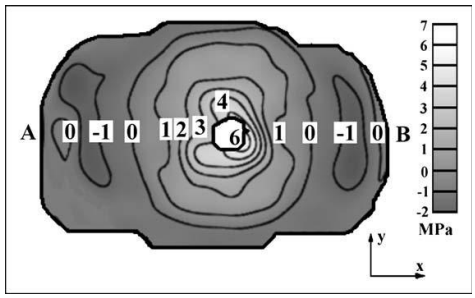

Fig. 8: Normal stress field in section AB

Figure 7 shows projections of Δcos 2φ and Δsin 2φ in section AB, which are directly used in Eqs. 1 and 2. Image of the electrode is straightened by shifting the projections for different angles β. Similar data were obtained for the auxiliary section of the stem.

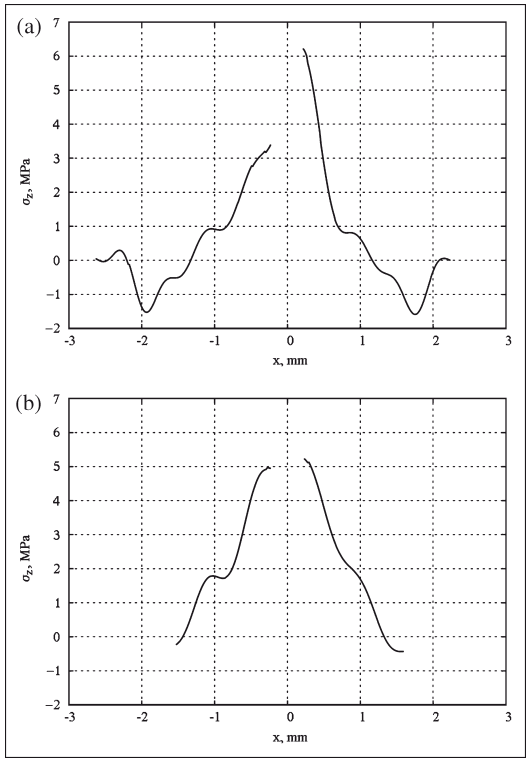

Fig. 9: Normal stress σ_z distribution on the (a) *x*-axis and (b) *y*-axis in section AB

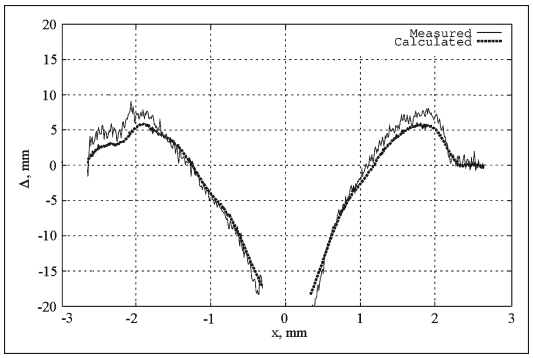

Fig. 10: Measured and calculated distribution of $\Delta\cos 2\varphi$ for the projection $\beta = 120^\circ$

On the basis of Figs. 6 and 7 and the contour from Fig. 5, the field of the normal stress σ_z (Fig. 8) was determined using the function $W(\xi, \beta)$ with 16 terms along the radial coordinate and 16 terms along the angular coordinate. Distribution of σ_z on the x- and y-axes is shown in Fig. 9.

Since σ_z is residual stress, theoretically its average value should be zero. Actually, the average value of σ_z in section AB is 0.2 MPa. That is about 5% of the maximum value of σ_z near the electrode.

Another possibility to check the precision of the results is comparison of actually measured experimental data with the data, calculated on the basis of the calculated stress field. Such a comparison of the distribution of $\Delta\cos 2\varphi$ (a) for the projection $\beta = 120^\circ$ is shown in Fig. 10.

Both checks permit to conclude that precision of tomographic measurement of the normal stress field is satisfactory.

CONCLUSION

A measurement technology for photoelastic tomography in linear approximation is described, and its application is demonstrated by measuring stress distribution in a stem of a high-pressure electric lamp. An estimation of the precision of the measurements has been given.

ACKNOWLEDGMENT

The author gratefully acknowledges the support of the Estonian Science Foundation under the grant no. 6881.

References

1. Srinath, L.S., *Scattered Light Photoelasticity*, Tata McGraw-Hill, New Delhi (1983).

2. Kuske, A., and Robertson, G., *Photoelastic Stress Analysis*, John Wiley and Sons, London, UK (1974).

3. Aben, H., *Integrated Photoelasticity*, McGraw-Hill, New York (1979).

4. Aben, H., and Guillemet, C., *Photoelasticity of Glass*, Springer-Verlag, Berlin, Germany (1993).

5. Aben, H., Anton, J., and Errapart, A., "Automatic Measurement of Residual Stress in Glass Articles of Complicated Shape," *Verre* **9**:30–35 (2003).

6. Herman, C.T., *Image Reconstruction from Projections*, Academic Press, New York (1980).

7. Natterer, F., *Mathematics of Computerized Tomography*, Teubner, Stuttgart (1986).

8. Sharafutdinov, V., "On Integrated Photoelasticity in Case of Weak Birefringence," *Proc Estonian Acad Sci Phys Math* **38**: 379–389 (1989, in Russian).

9. Sharafutdinov, V.A., *Integral Geometry of Tensor Fields,* VSP, Utrecht, The Netherlands (1994).

10. Aben, H., Idnurm, S., and Puro, A., "Integrated Photoelasticity in Case of Weak Birefringence," *Proceedings of the 9th International Conference on Experimental Mechanics*, Volume 2, Copenhagen, 867–875 (1990).

11. Aben, H., Idnurm, S., Josepson, J., Kell, K.-J., and Puro, A., "Optical Tomography of the Stress Tensor Field," Levin, G., (ed), *Analytical Methods for Optical Tomography, Proc. SPIE* **1843**, SPIE Press, Bellingham, WA, 220–229 (1991).

12. Aben, H., Errapart, A., Ainola, L., and Anton, J., "Photoelastic Tomography in Linear Approximation," *Proceedings International Conference on Advanced Technology in Experimental Mechanics ATEM'03,* Nagoya, Japan, CD ROM, p. 6 (2003).

13. Aben, H.K., Errapart, A., Ainola, L., and Anton, J. "Photoelastic Tomography for Residual Stress Measurement in Glass," *Opt Eng* **44**:093601 (2005).

14. Aben, H.K., Josepson, J.I., and Kell, K.-J., "The Case of Weak Birefringence in Integrated Photoelasticity," *Opt Lasers Eng* **11**: 145–157 (1989).

15. Cormack, A.M., "Representation of a Function by its Line Integrals, With Radiological Applications," *J Appl Phys* **34**: 2722–2727 (1963).

16. Mason, J.C., *Chebyshev Polynomials*, Chapman & Hall/CRC Press, Roca Baton, FL (2002).

17. Born, M., and Wolf, E., *Principles of Optics*, Pergamon Press, New York (1986).

18. Haake, S.J., Wang, Z.F., and Patterson, E.A., "Evaluation of Full-Field Automated Photoelastic Analysis Based on Phase-Stepping," *Experimental Techniques* **17**:19–25 (1993).

19. Aben, H., Ainola, L., and Anton, J., "Half-Fringe Phase-Stepping With Separation of the Principal Stress Directions," *Proc Estonian Acad Sci Eng* **5**:198–211 (1999).

20. Rosenberg, K.M., "CTSim—The Open Source Computed Tomography Simulator," URL http://www.ctsim.org/ [accessed 15 February 2007]. ■

Paper III

Errapart, A. Determination of all stress components of axisymmetric stress state in photoelastic tomography. In *Advances in Experimental Mechanics VIII : Selected, peer-reviewed papers of the 8th International Conference on Advances in Experimental Mechanics: Integrating Simulation and Experimentation for Validation, (BSSM 2011), Sept. 7-9 2011, Edinburgh, Scotland* (Burguete R. L. et al., eds.). Trans Tech Publications, Durnten-Zuerich, 2011, 434-439.

Applied Mechanics and Materials Vol. 70 (2011) pp 434-439
Online available since 2011/Aug/18 at www.scientific.net

doi:10.4028/www.scientific.net/AMM.70.434

Determination of all stress components of axisymmetric stress state in photoelastic tomography

Andrei Errapart

Institute of Cybernetics, Tallinn University of Technology, Estonia

andreie@cs.ioc.ee

Keywords: photoelastic tomography; residual stress; glass; axisymmetric stress.

Abstract. In this paper we describe the application of photoelastic tomography for determining stresses in glass. The basic equations of linear approximation in photoelastic tomography are presented. Since these equations permit direct determination only of the axial and shear stress, a method for calculating the other stress components is described. In the case of the residual stresses, it uses the equilibrium equation and the generalized sum rule. In the case of stresses due to external loads, it uses the equilibrium and compatibility equations. It is shown, both graphically and analytically, that integration of these equations must start at the axis and proceed along the positive direction of the radial axis. As an example, residual stresses in the stem of a wine glass are determined. Results are verified by comparing the birefringence, calculated from the determined stress state, with measured birefringence. The numerical algorithm for the case of stresses due to external loads is verified by using the theoretical solution for a Hertzian contact stress problem.

Introduction

The strength of glass and its resistance to scratches can be increased by introducing compressive residual stresses onto its surface by tempering. In order to establish optimal an level of tempering, it is important to measure the value of the residual stresses. Photoelastic tomography permits quantitative measurements of residual stresses in glass articles of complicated shape.

In photoelastic tomography of axisymmetric objects the axial and shear stress distributions are directly determined from the measurement data [1,2]. The remaining stress components, the radial and circumferential stress, are determined using the equilibrium and compatibility equations when stresses are due to the external loads. In case of residual stresses, instead of the compatibility equation, the generalized sum rule is used [3].

By using the equilibrium equation and the compatibility equation and the generalized sum rule, discrete algorithms for calculating radial and circumferential stresses are described. Residual stresses in the stem of a wine glass have been determined. On the basis of the obtained stress field the corresponding birefringence is calculated using the Jones matrix formalism [4] and compared to the measured birefringence. Radial and circumferential stress components of the Hertzian contact stress field have been determined using the described algorithm and compared to the theoretical solution.

Photoelastic tomography in linear approximation

In photoelastic tomography [1,2] the test object is placed in an immersion tank with matching immersion liquid. A beam of polarized light is passed through the wall of the specimen (Fig. 1).

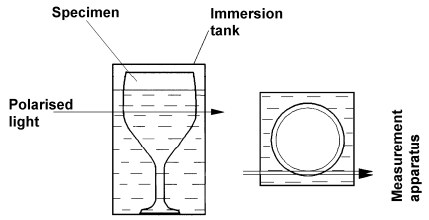

Fig. 1: Experimental set-up in photoelastic tomography.

In the case of an axisymmetric test object the transformation of the polarization of light in the specimen can be characterized by the parameter of the isoclinic φ and the optical retardation δ. These parameters can be measured on every light ray with conventional polariscopes. It has been shown that when optical retardation is less than a quarter of the wavelength or rotation of the principal stress directions is less than $\pi/6$, the components of the stress tensor are related to the birefringence with simple integral relationships [1,2,5]

$$\delta \cos 2\varphi = C\int (\sigma_z - \sigma_x)\mathrm{d}y\,, \tag{1}$$

$$\delta \sin 2\varphi = C\int \tau_{zx}\mathrm{d}y\,, \tag{2}$$

where C is the photoelastic constant, and σ_x, σ_z and τ_{zx} are components of the stress tensor in the plane perpendicular to the light ray y.

It has been shown that if the parameter of the isoclinic φ and optical retardation δ have been measured on many light rays in two parallel sections, perpendicular to the axis z of the axisymmetric specimen, then radial distribution of the axial stress σ_z and shear stress τ_{rz} can be determined either by approximating with the polynomials [2] or by using the generalized onion peeling method [6].

Determination of radial and circumferential stresses in the case of residual stresses in glass

The remaining stress components, σ_r and σ_θ, are determined using equations of the theory of elasticity. The stress components must satisfy the equation of equilibrium

$$\frac{\partial \sigma_r}{\partial r} + \frac{\sigma_r - \sigma_\theta}{r} + \frac{\partial \tau_{rz}}{\partial z} = 0\,. \tag{3}$$

and, in the case of residual stress in the glass, also the generalized sum rule [3]

$$\sigma_r + \sigma_\theta = \sigma_z - 2\int_{r_0}^{r} \frac{\partial \tau_{rz}}{\partial z}\mathrm{d}r + C_1\,, \tag{4}$$

where C_1 is an integration constant determined from the boundary conditions at the surfaces of the specimen. Substitution of σ_θ from the sume rule into Eq. (3) reveals the differential equation for the radial stress

$$\frac{\mathrm{d}\sigma_r}{\mathrm{d}r} + \frac{2\sigma_r - \sigma_z + 2\int_{r_0}^{r} \frac{\partial \tau_{rz}}{\partial z}\mathrm{d}r - C_1}{r} + \frac{\partial \tau_{rz}}{\partial z} = 0\,. \tag{5}$$

Numerical integration of Eq. (5) is required to be done in the direction in which the differential equation is stable or asymptotically stable. Solutions of an ordinary differential equation in the form

$$\dot{x} = a(t)x + b(t) \tag{6}$$

are *asymptotically stable* when $a < 0$ for all values of t, *stable* when $a \le 0$ for all t and for positive values of a stability cannot be established [7]. Rewriting Eq. (5) in the form similar to Eq. (6) gives

$$\dot{\sigma}_r = -\frac{2}{r}\sigma_r + \frac{\sigma_z - 2\int_{r_0}^{r} \frac{\partial \tau_{rz}}{\partial z}\mathrm{d}r - C_1}{r} + \frac{\partial \tau_{rz}}{\partial z}\,, \tag{7}$$

from which it follows that $a = -0.5/r < 0$ for all values of r and therefore solutions of the Eq. (5) are asymptotically stable. Thus, numerical integration of Eq. (5) should start at the axis and proceed along the positive direction of the radial axis. Integration in the negative direction of the radial axis is sensitive to small changes in the initial value. This is illustrated in Fig. 2a, where three calculated radial stress distributions corresponding to three initial values, differing only by 0.01, are shown.

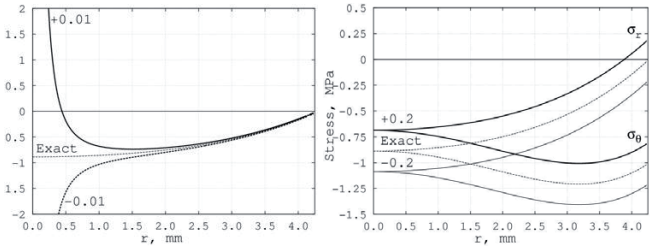

(a) (b)

Fig. 2: Three radial stress distributions corresponding to the three initial values differing by 0.01 when integrating along the negative direction of the radial axis (a) and three radial and circumferential stress distributions corresponding to the three initial values differing by steps of 0.2 when integrating along the positive direction of the radial axis (b).

In the case of a hollow specimen, the initial value of the radial stress at the internal surface, $\sigma_r(r_0)$, can be determined directly from the value of the stress at the internal surface, $\sigma_s(r_0)$, as follows:

$$\sigma_r(r_0) = \sigma_s(r_0)\sin^2\beta, \tag{8}$$

where β is the angle of the normal to the internal surface.

In the case of solid specimens the initial value of the radial stress has to be determined so that experimentally determined boundary conditions at the external surface are satisfied. This is done by first performing trial integration of Eq. (5) with the trial initial value of $\sigma_r(0)=0$. The difference of boundary conditions and the stresses at the external surface, obtained by trial integration, is added to the initial value and integration is repeated. It has been that one correction is sufficient for obtaining the initial value by which the boundary conditions at the external surface are satisfied. The integration constant C_1 in Eq. (5) is determined from the boundary conditions at the axis

$$C_1 = 2\sigma_r(0) - \sigma_z(0), \tag{9}$$

where $\sigma_z(0)$ and $\sigma_r(0)$ are the values of axial and radial stress on the axis. Let us define function $f(r)$ as follows

$$f(r) = \frac{\sigma_z - 2\int_0^r \frac{\partial \tau_{rz}}{\partial z}\mathrm{d}r - \sigma_z(0)}{r} + \frac{\partial \tau_{rz}}{\partial z}. \tag{10}$$

Substitution $f(r)$ and integration constant C_1 into Eq. (5) gives

$$\frac{\mathrm{d}\sigma_r}{\mathrm{d}r} + \frac{2}{r}\sigma_r - \frac{2}{r}\sigma_r(0) = f(r)\cdot \tag{11}$$

Given that σ_r is a solution corresponding to the initial value $\sigma_r(0)$, we show that adding a constant value C to it also gives a solution by substituting $\sigma_r^{'} = \sigma_r + C_2$ into Eq. (11)

$$\frac{\mathrm{d}(\sigma_r + C_2)}{\mathrm{d}r} + \frac{2}{r}(\sigma_r + C_2) - \frac{2}{r}(\sigma_r(0) - C_2) = f(r)\cdot \tag{12}$$

Simplifying Eq. (12) leads to Eq. (11). All possible solutions differ by a constant value equal to the differences in the initial values $\sigma_r(0)$; this is illustrated in Fig. 2b. Any correction to the initial value changes the value of stress at the external surface for exactly the same amount, thus, only one trial integration is required for obtaining the correct initial value of $\sigma_r(0)$.

Let us model the stress field in an axisymmetric specimen with N concentric layers, each of thickness Δr and in each of which the stress state may be considered constant. Let us denote stress components of this discrete model as $\sigma_{z,i}$, $\sigma_{r,i}$, $\sigma_{\theta,i}$ and $\tau_{rz,i}$, where i is the number of the layer, with innermost layer numbered 1 and the outermost N. The numerical algorithm for determining the radial stress is obtained by rewriting Eq. (10) as a difference equation as follows

$$\sigma_{r,1} = \sigma_r(r_0), \tag{13}$$

$$\sigma_{r,i} = \sigma_{r,i-1} - \Delta r\left(\frac{2\sigma_{r,i} - \sigma_{z,i} + 2t_i - C_1}{r_i} + \frac{\partial \tau_{rz,i}}{\partial z}\right), \tag{14}$$

where

$$t_i = \sum_{j=0}^{i} \frac{\partial \tau_i}{\partial z}\Delta r. \tag{15}$$

Algorithm for determining the circumferential stress distribution is obtained by rewriting Eq. (4) as

$$\sigma_{\theta,i} = \sigma_{z,i} - 2t_i + C_1 - \sigma_{r,i}. \tag{16}$$

Determination of radial and circumferential stresses in the case of external loads

In case of external loads, the remaining stress components, σ_r and σ_θ, are determined using the equilibrium equation (Eq. 8) and the compatibility equation

$$\frac{\partial}{\partial r}\left[\sigma_\theta - \nu(\sigma_r + \sigma_z)\right] - (1+\nu)\frac{\sigma_r - \sigma_\theta}{r} = 0. \tag{17}$$

Substituting $\frac{\partial \sigma_r}{\partial r}$ from the equation of equilibrium into Eq. (17) gives

$$\frac{\partial \sigma_\theta}{\partial r} + \nu\frac{\partial \tau_{rz}}{\partial z} - \nu\frac{\partial \sigma_z}{\partial r} - \frac{\sigma_r - \sigma_\theta}{r} = 0. \tag{18}$$

Numerical integration of the system of equations (3), (18) should be done in the direction in which the system is stable or asymptotically stable. Solutions of a system of ordinary differential equations in the form

$$\dot{x} = A(t)x + b(t) \tag{19}$$

are *stable* if $A(t)$ is diagonalizable and $\Re(\lambda_i) \le 0$ for all i,t, where $\lambda_i, i \in 1\ldots N$ are the eigenvalues of the $N \times N$ matrix $A(t)$ [7]. Rewriting Eqs. (3), (18) in the form similar to Eq. (19) gives

$$\begin{pmatrix} \dot{\sigma}_r \\ \dot{\sigma}_\theta \end{pmatrix} = A(r)\begin{pmatrix} \sigma_r \\ \sigma_\theta \end{pmatrix} + \begin{pmatrix} -\frac{\partial \tau_{rz}}{\partial z} \\ -\nu\frac{\partial \tau_{rz}}{\partial z} + \nu\frac{\partial \sigma_z}{\partial r} \end{pmatrix}, \tag{20}$$

where

$$A(r) = \begin{pmatrix} -\frac{1}{r} & \frac{1}{r} \\ \frac{1}{r} & -\frac{1}{r} \end{pmatrix}. \tag{21}$$

Eigenvalues of $A(r)$ are $\lambda_1 = 0$, $\lambda_2 = -2/r$. The diagonalized form of A can be found by using the matrix P composed of eigenvectors of A

$$P = \begin{pmatrix} \sqrt{0.5} & \sqrt{0.5} \\ \sqrt{0.5} & -\sqrt{0.5} \end{pmatrix}, \tag{22}$$

$$\text{diag } A = P^{-1}AP = \begin{pmatrix} 0 & 0 \\ 0 & -\frac{2}{r} \end{pmatrix}. \tag{23}$$

Thus, the system of Eqs. (8), (23) is *stable* and numerical integration should start at the axis and proceed along the positive direction of the radial axis.

The boundary conditions can be applied in a manner similar to the case of residual stresses. Given that σ_r, σ_θ is a solution, substituting $\sigma_r^{'} = \sigma_r + C_2$, $\sigma_\theta^{'} = \sigma_\theta + C_2$ into Eqs. (3),(18), where C_2 is a constant, will lead back to the Eqs. (3),(18) after simplifying.

Using the discrete model introduced in the previous chapter, the numerical algorithm for determining the radial and circumferential stress is obtained by rewriting Eq. (20) as a system of difference equation as follows

$$\sigma_{r,0} = \sigma_r(0), \tag{24}$$

$$\sigma_{\theta,0} = \sigma_\theta(0), \tag{25}$$

$$\sigma_{r,i+1} = \sigma_{r,i} + \Delta r\left(-\frac{1}{r_i}\sigma_{r,i} + \frac{1}{r_i}\sigma_{\theta,i} - \frac{\partial \tau_{rz,i}}{\partial z}\right), \tag{26}$$

$$\sigma_{\theta,i+1} = \sigma_{\theta,i} + \Delta r\left(\frac{1}{r_i}\sigma_{r,i} - \frac{1}{r_i}\sigma_{\theta,i} - \nu\frac{\partial \tau_{rz,i}}{\partial z}\right) + \nu(\sigma_{z,i+1} - \sigma_{z,i}). \tag{27}$$

Examples

As an experimental example, residual stresses in the stem of a wine glass were determined. Geometry of the wine glass is shown in Fig. 3a and the fringe pattern in Fig. 3b.

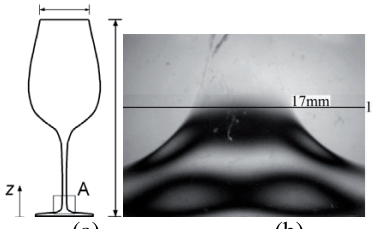

Fig. 3: Geometry of the wine glass (a) and fringe pattern in the area A (b).

Results of stress determination in section 1 are shown in Fig. 4a. As a verification of the precision of the algorithm, the birefringence, corresponding to the determined stress state, was calculated using the Jones matrix formalism [4] and compared with the measured birefringence (Fig. 4b). The match is excellent.

As a numerical example of the applicability of the numerical algorithm Eqs. (24)-(27), radial and circumferential stresses of the Hertzian contact stress field were determined and compared with the theoretical stress field (Fig. 5). The match confirms the correctness of the numerical algorithm.

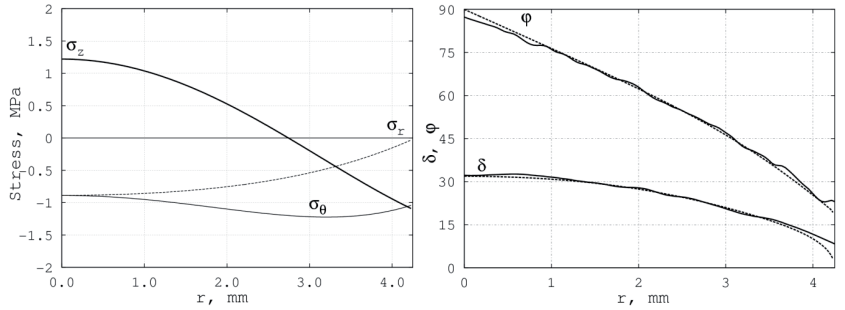

(a) (b)

Fig. 4: Distribution of stress components in section 1 (a) and Measured birefringence (*solid line*) and calculated birefringence corresponding to the determined stress state (*dashed line*) in section 1 (b).

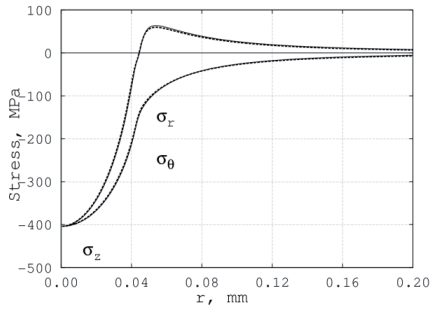

Fig. 5: Hertzian contact stress field at the depth 0.001 mm, corresponding to load P = 2.7N. Radial and circumferential stresses have been determined with the numerical algorithm Eqs. (24)-(27) (*solid line*). Theoretical stress field is given with *dashed lines*.

Conclusions

A linear algorithm of photoelastic tomography for complete determination of axisymmetric stresses in axisymmetric glass products has been elaborated. As a practical example, residual stresses in a section of the stem of a wine glass have been determined. Calculated birefringence, corresponding to the determined stress field, shows good agreement with measured birefringence, thus verifying the algorithm. In the case of the stresses due to external loads, results of the numerical algorithm have been shown to match the theoretical stress field in the case of the Hertzian contact problem.

Acknowledgement

This study was supported by the Estonian Science Foundation (grant ETF7840).

References

[1] H. Aben, A. Errapart, L. Ainola, J. Anton, in: Opt. Eng. Vol. 44 (2005), 1–8 (093601).
[2] H. Aben and C. Guillemet: *Photoelasticity of Glass* (Springer-Verlag, Berlin 1993).
[3] H. Aben, L.Ainola and J. Anton, in: Proc. Int. Conf. Adv. Technol. Exp. Mech. ATEM'99, Ube, Japan, Vol. 2 (1999), 629–634.
[4] P.S. Theocaris, E.E. Gdoutos: *Matrix theory of photoelasticity* (Springer, Berlin 1979).
[5] H. K. Aben, J. I. Josepson, and K.-J. Kell, in: Opt. Lasers Eng. Vol. 11 (1989), 145–157.
[6] J. Anton, A. Errapart, H. Aben and L. Ainola, in: Exp. Mech. Vol. 48 (2008), 613-620.
[7] M. Hazewinkel: *Encyclopaedia of Mathematics* (Kluwer Academic Publishers, London 1998).

Paper IV

Aben, H., Errapart, A. A non-linear algorithm of photoelastic tomography for the axisymmetric problem. *Experimental Mechanics*, 2007, 47(6), 821 - 830.

Experimental Mechanics (2007) 47:821–830
DOI 10.1007/s11340-007-9057-5

A Non-linear Algorithm of Photoelastic Tomography for the Axisymmetric Problem

H. Aben · A. Errapart

Received: 15 September 2006 / Accepted: 30 April 2007 / Published online: 24 May 2007

Abstract A non-linear algorithm of photoelastic tomography for the measurement of axisymmetric stress fields has been elaborated. It is free of any assumptions concerning the value of the birefringence or rotation of the principal stress axes along the light rays. The algorithm is based on the measurement of characteristic directions and phase retardation in two parallel sections of the test object. Stress components are presented in the form of power series along the radial coordinate. A differential evolution algorithm has been used for finding the stress field parameters, which fit the measurement data best. Application of the method is illustrated by residual stress measurement in a drinking glass.

Keywords Photoelastic tomography · Residual stress · Glass · Differential evolution algorithm

Introduction

Non-destructive measurement of 3D stress fields has been an ambition of experimental mechanics for a long time. In photoelasticity, the idea of a universal 3D stress measurement technology, the scattered light method, was published by Weller already more than half a century ago [1]. The classical version of the method [2, 3] as well as its modifications [4–7] have found certain applications in engineering practice by investigating 3D stress fields in general and contact stress problems in particular. However, comparatively complicated apparatus and measurement technology are evidently the reasons why this method has not obtained wider popularity.

One of the most powerful contemporary methods for the analysis of the internal structure of different objects, from human bodies to parts of atomic reactors, is tomography [8–10]. The question arises whether it is also possible to determine tomographically stress fields in 3D objects. This problem is not trivial for the following reason. Classical tomography considers only determination of scalar fields, i.e., every point of the field is characterized by a single number (the coefficient of attenuation of X-rays, the acoustical or optical scalar index of refraction, etc.). Since stress is a tensor, in stress field tomography every point of the field is characterized by six numbers. Thus the problem is much more complicated in principle. Let us mention that while a huge number of papers and about a hundred of books are devoted to scalar field tomography, there is only a single book, written by Sharafutdinov [11], devoted to mathematical problems of tensor field tomography.

Certain information about stresses in 3D transparent objects can be obtained with integrated photoelasticity [12]. In integrated photoelasticity, the transparent 3D specimen is placed in an immersion tank, and a beam of polarized light is passed through the specimen. The transformation of the polarization of light is measured on many light rays and for many azimuths of the light beam. This measurement data are related in a complicated way to the stress field.

It is natural to base photoelastic tomography on integrated photoelasticity. Unfortunately, the relationships of integrated photoelasticity, which relate measurement data to the stress field, are non-linear. This non-linearity is due to the fact that in a 3D stress field on a light ray both the values of the principal stresses as well as their directions are not constant. Principal stress directions in the plane x', z'

H. Aben (✉, SEM member) · A. Errapart
Institute of Cybernetics, Tallinn University of Technology,
21 Akadeemia tee, 12618 Tallinn, Estonia
e-mail: aben@ioc.ee
URL: http://ioc.ee

perpendicular to the light ray, are determined by the stress components $\sigma_{x'} - \sigma_{z'}$ and $\tau_{x'z'}$. If both of these vary along the light ray in an arbitrary manner, the principal stress axes are not constant. Actually a rotation of the principal stress axes on light rays takes place in inhomogeneous 3D stress fields. However, in case of weak birefringence or weak rotation of the principal stress axes, the theory of integrated photoelasticity can be linearized. Using this linear approximation, Sharafutdinov elaborated an algorithm of photoelastic tomography [11, 13]. A somewhat different linear algorithm is described in [14–16]. Linear approximation of photoelastic tomography has been mainly used for residual stress measurement in glass [16, 17].

In many cases of stress measurement neither the birefringence nor the rotation of the principal stress axes is weak, i.e., the assumptions of the linear approximation of photoelastic tomography are not valid. Such a situation often occurs, for example, by measuring residual stress in glass articles of complicated shape. The aim of the present paper is to develop an algorithm of photoelastic tomography for axisymmetric problems, which is free of any assumptions about the value of the birefringence or rotation of the principal stress axes.

To tackle the problem under investigation systematically, we first describe briefly the classical tomography and the linear approximation of photoelastic tomography. Then we give a review of the basic non-linear relationships of integrated photoelasticity. After that we describe in detail the non-linear algorithm of photoelastic tomography and the basic part of this algorithm, the method of differential evolution. We conclude the paper with an example of residual stress measurement in a rim-tempered drinking glass.

Classical Tomography

In tomography, some radiation (X-rays, protons, acoustic waves, light, etc.) is passed through a section of the object in many directions, and properties of the radiation after it has passed the object (intensity, phase, deflection, etc.) are measured on many rays (Fig. 1). Experimental data $g(l, \theta^*)$ for different values of the angle θ^* are called *projections*.

If $f(r, \varphi)$ is in the radial coordinates r, φ the function that determines the distribution of a certain parameter of the field, experimental data for a real pair l, θ^* can be expressed by the Radon transform of the field,

$$g\left(l,\theta^*\right) = \int_{-\infty}^{\infty} f\left[r\left(l,\theta^*,z\right),\varphi\left(l,\theta^*,z\right)\right]\mathrm{d}z. \tag{1}$$

When projections for many values of θ^* have been recorded, the function $f(r, \varphi)$ is determined from the Radon inversion

$$f(r,\varphi) = \frac{1}{2\pi^2}\int_0^{\pi}\mathrm{d}\theta^*\int_{-\infty}^{\infty}\frac{\partial g\left(l,\theta^*\right)}{\partial l}\frac{\mathrm{d}l}{r\cos\left(\theta^*-\varphi\right)-l}. \tag{2}$$

Many numerical algorithms for solving equation (2) have been elaborated [8, 9]. In classical tomography it is assumed that $f(r, \varphi)$ is a scalar function.

Photoelastic Tomography in Linear Approximation

It has been shown [18] that in linear approximation an inhomogeneous birefringent medium can be considered optically equivalent to a birefringent plate. It is possible to measure the parameter of the isoclinic φ and optical retardation Δ on every light ray that passes the specimen.

Let us assume that in two parallel sections $z=z_0$ and $z = z_0 + \Delta z$ of an arbitrary 3D specimen tomographic photoelastic measurements, rotating the specimen around the z axis, have been carried out and the integrals V_1 and V_2 have been measured for many azimuths β (Fig. 2) for light rays, parallel to y':

$$V_1 = \Delta\cos 2\varphi = C\int\left(\sigma_{x'} - \sigma_{z'}\right)\mathrm{d}y', \tag{3}$$

$$V_2 = \Delta\sin 2\varphi = 2C\int\tau_{x'z'}\mathrm{d}y', \tag{4}$$

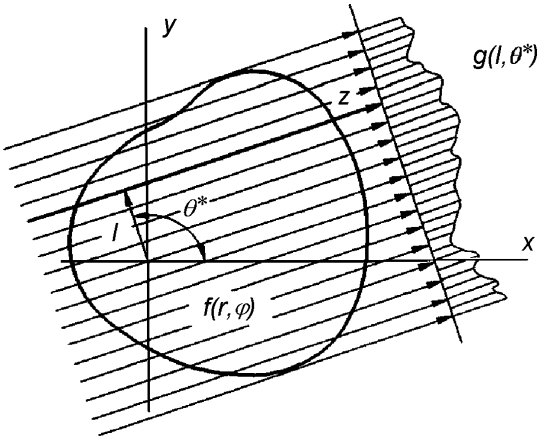

Fig. 1 Scheme of tomographic measurements

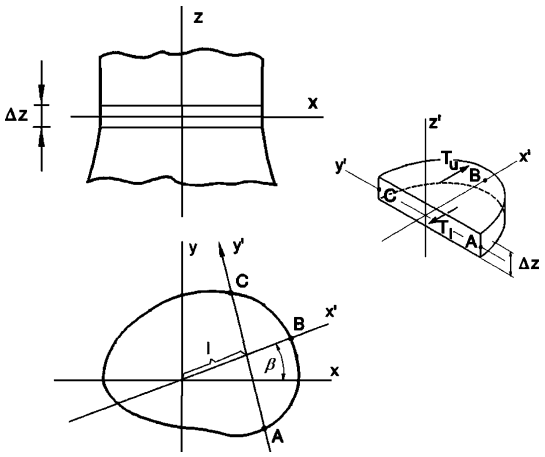

Fig. 2 Illustration explaining tomographic measurement scheme

where C is the photoelastic constant. Section $z=z_0$ is named "the main section" and the section $z = z_0 + \Delta z$ "the auxiliary section". Location of the light ray y' is determined by the value of its x' coordinate l and the angle β.

Equations (3) and (4) are valid if birefringence is weak (optical retardation is less than about one third of the wavelength) or the rotation of the principal stress axes is small (less than about $\pi/6$). If no rotation of the principal stress axes is present, equations (3) and (4) are valid for arbitrary birefringence.

Sharafutdinov suggested the following method for the measurement of the distribution of the axial stress σ_z [11, 13]. Besides the measurement of the functions V_1 and V_2, the value of the axial stress σ_z is to be measured on the boundary of the cross section. Applying to the functions V_1 and V_2 the transverse ray transform [11], the σ_z field is determined from the boundary value problem for a Poisson equation. Sharafutdinov has shown that the solution of this tomographic problem is unique and that only the distribution of σ_z can be determined in this way [11, 13].

The drawback of this method is that, in addition to tomographic photoelastic measurements, the boundary values of σ_z must be measured. That is possible only in the case when the boundary of the cross section is described by a convex curve. Besides, the transverse ray transform is rather complicated. The tomographic algorithm of Sharafutdinov has not been applied in practice, although it is important from the point of view of the theory of photoelastic tomography.

Another algorithm of the photoelastic tomography in linear approximation is the following. Let us assume that photoelastic tomographic measurements have been carried out in two parallel sections, a distance Δz apart from each other, rotating the specimen around the z axis (Fig. 2). The values of the functions V_1 and V_2 in the auxiliary section we denote by V_1' and V_2'. Considering the equilibrium of the three-dimensional segment ABC in the direction of the x' axis (Fig. 2), we may write

$$\Delta z \int_A^C \sigma_{x'} \mathrm{d}y' = T_u - T_l, \tag{5}$$

where T_u and T_l are the shear forces on the upper and lower surfaces of the segment, respectively:

$$T_u = \frac{1}{2C} \int_l^B V_2' \mathrm{d}x', \quad T_l = \frac{1}{2C} \int_l^B V_2 \mathrm{d}x'. \tag{6}$$

Taking into consideration relationships (5) and (6), equation (3) reveals

$$\int_A^C \sigma_z \mathrm{d}y' = \frac{1}{2C\Delta z} \left(\int_l^B V_2' \mathrm{d}x' - \int_l^B V_2 \mathrm{d}x' \right) - \frac{V_1}{C}. \tag{7}$$

Since tomographic photoelastic measurement data can be obtained for all the light rays y' (for many values of l and β), equation (7) expresses the Radon transform of the field of the stress σ_z. Thus we have reduced a problem of tensor field tomography to a problem of scalar field tomography for a single stress component σ_z. The field of σ_z can be determined using any of the well-known Radon inversion techniques [8, 9]. Rotating the specimen by tomographic measurements around the axes x and y, the fields of σ_x and σ_y can also been determined.

In case of an axisymmetric stress field, the problem is reduced to a problem of one-dimensional tomography [19]. In this case the distribution of σ_z is determined from equation (7) with Abel inversion [20]. In linear approximation, photoelastic tomography has been mainly used for residual stress measurement in axisymmetric glass articles [16, 17].

Let us mention that we consider photoelastic tomography, which is based on the measurement on every light ray of the parameter of the isoclinic φ and *relative optical retardation* Δ. Photoelastic tomography with interferometric measurement of *absolute optical retardations* has not lead to positive results [21]. By formulating the problem of photoelastic tomography it is important to distinguish between these two formulations. Otherwise one may reach erroneous results [22].

In many cases assumptions of the linear approximation are not valid and the problem of photoelastic tomography is to be formulated in the general, non-linear form.

Basic Non-linear Relationships of Integrated Photoelasticity

If polarized light passes a 3D specimen, the transformation of polarization can be described as [12]

$$\begin{pmatrix} E_x* \\ E_y* \end{pmatrix} = U \begin{pmatrix} E_{x_0} \\ E_{y_0} \end{pmatrix}, \tag{8}$$

where E_{x_0}, E_{y_0} are the components of the incident light vector and E_x*, E_y* describe polarization of the light that emerges from the specimen. The matrix U is a two-by-two unitary unimodular matrix, which in the general case can be written as

$$U = \begin{pmatrix} e^{i\xi}\cos\theta & e^{i\zeta}\sin\theta \\ -e^{-i\zeta}\sin\theta & e^{-i\xi}\cos\theta \end{pmatrix}, \tag{9}$$

where ξ, ζ, and θ are functions of the stress distribution between the points of entrance and emergence of light.

Analysis of the transformation matrix (9) has shown that there always exist two perpendicular directions of the polarizer at which the light emerging from the medium is linearly polarized. These directions of polarization of the incident and emerging light are called the primary and secondary characteristic directions. They are determined through the angles α_0 and $\alpha*$ as follows [12]:

$$\tan 2\alpha_0 = \frac{\sin(\zeta+\xi)\sin 2\theta}{\sin 2\xi\cos^2\theta - \sin 2\zeta\sin^2\theta}, \tag{10}$$

$$\tan 2\alpha* = \frac{\sin(\zeta-\xi)\sin 2\theta}{\sin 2\xi\cos^2\theta + \sin 2\zeta\sin^2\theta}. \tag{11}$$

Due to their exceptional physical properties, the characteristic directions can be measured experimentally. It is also possible to measure the characteristic optical retardation $\Delta*$ between the secondary characteristic vibrations:

$$\cos\Delta* = \cos 2\xi\cos^2\theta + \cos 2\zeta\sin^2\theta. \tag{12}$$

A number of manual or semiautomated methods for the measurement of the characteristic parameters are described in [12]. Most efficient for that are modifications of the classical phase-stepping method [23, 24].

If the characteristic parameters α_0, $\alpha*$, and $\Delta*$ are determined experimentally on a light ray, it is possible to calculate the parameters ξ, ζ, and θ of the transformation matrix U:

$$\tan\xi = \frac{\cos(\alpha_0+\alpha*)}{\cos(\alpha_0-\alpha*)}\tan\frac{\Delta*}{2}, \tag{13}$$

$$\tan\zeta = \frac{\sin(\alpha_0+\alpha*)}{\sin(\alpha_0-\alpha*)}\tan\frac{\Delta*}{2}, \tag{14}$$

$$\tan\theta = \frac{\cos\xi}{\cos\zeta}\tan(\alpha_0-\alpha*) = \frac{\sin\xi}{\sin\zeta}\tan(\alpha_0+\alpha*). \tag{15}$$

The algorithm of non-linear photoelastic tomography should be based on equations (10)–(15). Evidently such an algorithm would be most complicated. Non-linear formulation of the problem of photoelastic tomography has been considered by several authors [26–30]. In these papers the tomographic method is mostly described verbally. Neither convincing numerical nor physical experiments have been carried out to test the validity of the suggested algorithms.

In the following a non-linear algorithm of photoelastc tomography will be based on the differential evolution technique.

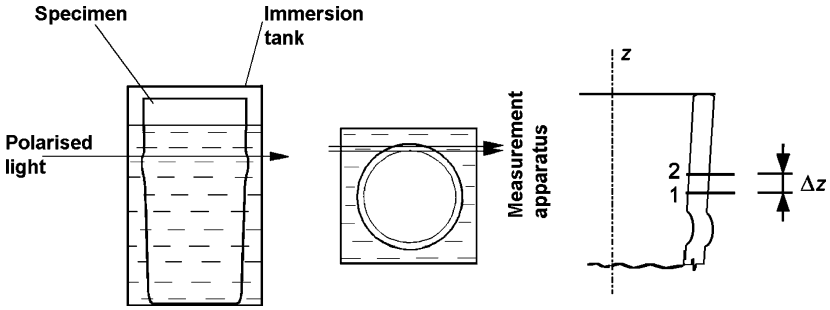

Fig. 3 The specimen is placed in an immersion tank and investigated by tangential incidence

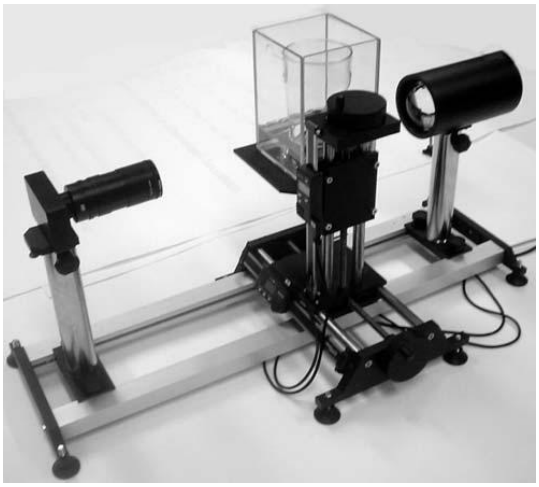

Fig. 4 Computer-controlled polariscope AP-06C with the specimen in the immersion bath

Non-linear Photoelastic Tomography

Technology of the Experiment

We assume that the stress field is axisymmetric. To avoid refraction of light, the specimen is placed in an immersion tank and investigated in a transmission polariscope with tangential incidence (Fig. 3). Figure 4 shows a photo of a computer-controlled polariscope AP-06C used in experiments. The light source is a light diode. The polariscope has a set of polaroids and quarter-wave plates to perform the phase-stepping method [25]. As an example, we consider residual stress measurement in hollow glassware.

Scanning the wall of the specimen in two parallel sections 1 and 2, the parameter of the isoclinic φ_i^m and optical retardation Δ_i^m are measured on n light rays (i=1, ..., n) in both sections (index "m" denotes experimentally measured values). In the axisymmetric case $\varphi=\alpha_0=\alpha^*$, where α_0 and α_* are the primary and secondary characteristic angles [12]. Measurement of φ_i^m and Δ_i^m in both sections at many points is the information on the basis of which we shall determine the stress field.

Since we assume that the stress field is axisymmetric, it is sufficient to pass polarized light through the wall of the test object parallel to only one direction as shown in Fig. 3. The number of light rays, for which φ_i^m and Δ_i^m are recorded, depends on the resolution of the CCD camera of the polariscope. In the polariscope, shown in Fig. 4, the resolution can be varied from 30 to 100 pixels per mm. We usually use measurement data from 30–50 light rays evenly distributed through the wall of the test object.

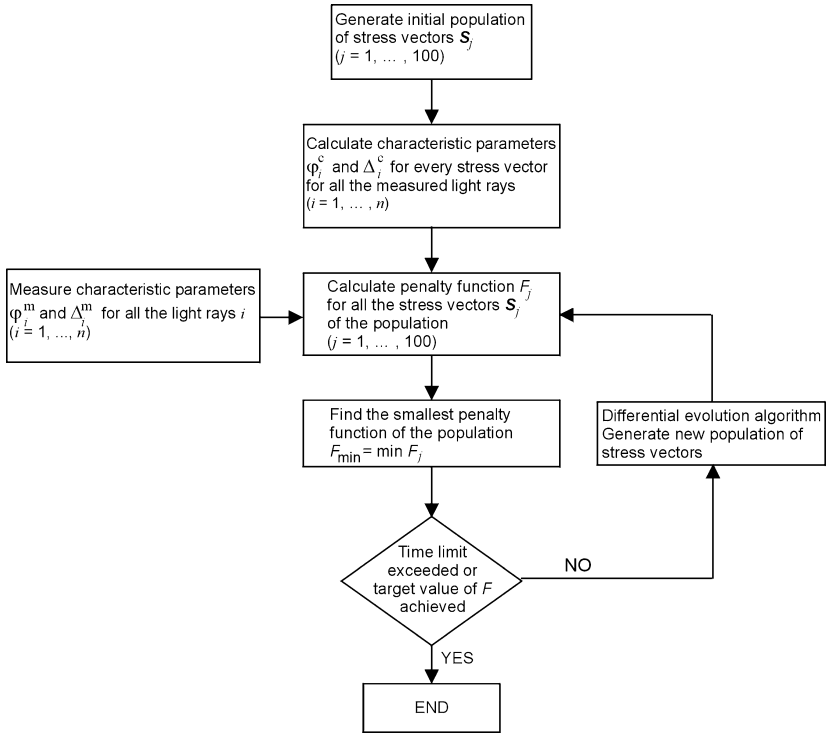

Fig. 5 General algorithm of non-linear photoelastic tomography

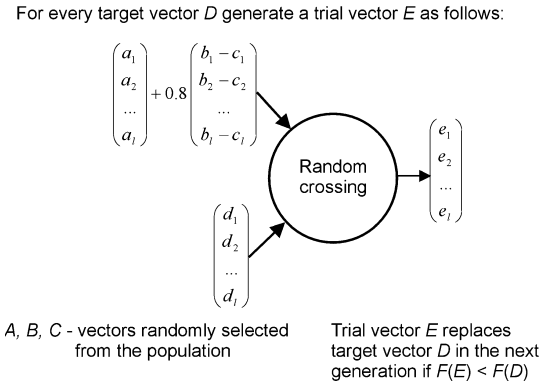

Fig. 6 Basic algorithm of differential evolution

For the measurement of φ_i^m and Δ_i^m we have used a modification of the classical phase-stepping method [25].

Expressions for Stresses

We present stress components σ_r, σ_θ, σ_z and τ_{rz} in cylindrical coordinates r, θ, z in the form of polynomials relative to the radial coordinate r:

$$\sigma_r = \sum_{k=0}^{m} a'_{2k} r^{2k}, \quad \sigma_\theta = \sum_{k=0}^{m} b'_{2k} r^{2k}, \tag{16}$$

$$\sigma_z = \sum_{k=0}^{m} c'_{2k} r^{2k}, \quad \tau_{rz} = \sum_{k=1}^{m+1} d'_{2k-1} r^{2k-1},$$

where prime denotes section 1. In section 2 stress components are expressed in the same way, distinguishing the coefficients with a double prime.

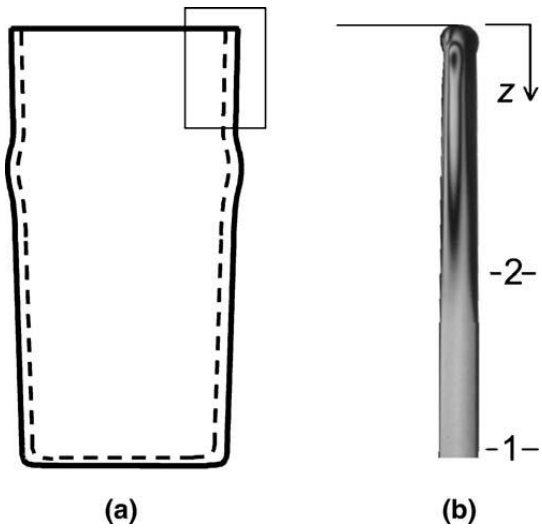

Fig. 7 Geometry of a rim-tempered glass (**a**) and integrated fringe pattern near the rim (**b**)

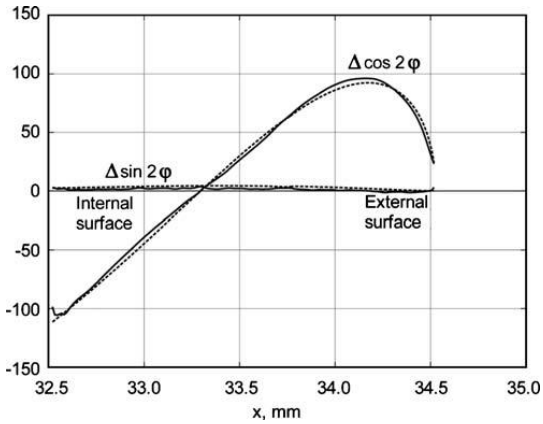

Fig. 8 Experimentally measured and calculated data in section 1: continuous lines, measured; dashed lines, calculated

Our aim is to determine the coefficients $a'_{2k}, b'_{2k}, c'_{2k}, d'_{2k-1}$, $a''_{2k}, b''_{2k}, c''_{2k}$ *and* d''_{2k-1} on the basis of experimentally measured φ_i^m and Δ_i^m (i=1, ... , n) in both sections.

The number of unknown coefficients can be reduced using equations of the theory of elasticity, boundary conditions and macrostatic equilibrium conditions. The stress components must satisfy the equation of equilibrium

$$\frac{\partial \sigma_r}{\partial r} + \frac{\sigma_r - \sigma_\theta}{r} + \frac{\partial \tau_{rz}}{\partial z} = 0. \tag{17}$$

In the case of residual stress in glass, the generalized sum rule [31, 32] is valid:

$$\sigma_r + \sigma_\theta = \sigma_z - 2 \int_{r_0}^{r} \frac{\partial \tau_{rz}}{\partial z} \mathrm{d}r + C_1, \tag{18}$$

where C_1 is an integration constant. Here r_0=0 in the case of a solid axisymmetric specimen. In the case of hollow glassware, r_0 is the radius of the internal surface.

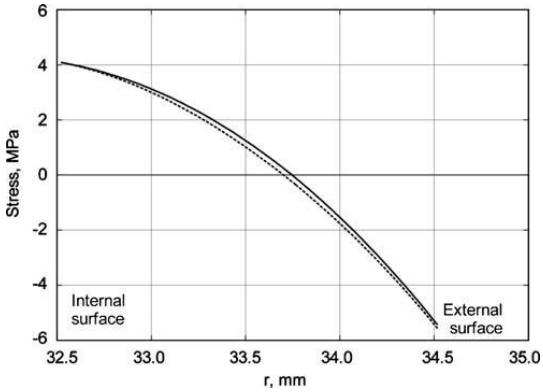

Fig. 9 Stresses σ_z (*continuous lines*) and σ_θ (*dashed lines*) in section 1, determined with linear photoelastic tomography

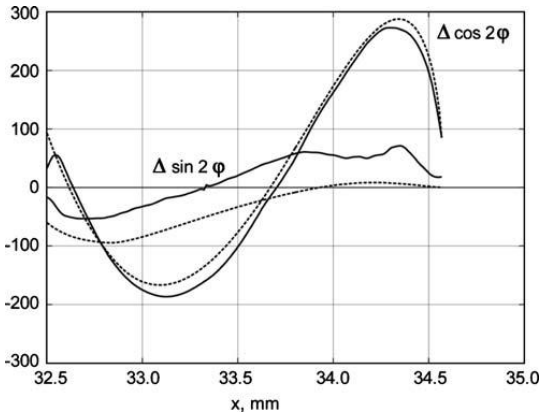

Fig. 10 Experimentally measured (*continuous lines*) and calculated (*dashed lines*) data in section 2

Using equations (17) and (18), the stress components σ_r and σ_θ can be expressed as [33]

$$\sigma_r = -\int_{r_0}^{r}\frac{\partial \tau_{rz}}{\partial z}\mathrm{d}r + \frac{1}{r^2}\int_{r_0}^{r} r\sigma_z \mathrm{d}r + \frac{1}{2}\frac{1}{r^2}C_2 + C_4, \tag{19}$$

$$\sigma_\theta = \sigma_z - \int_{r_0}^{r}\frac{\partial \tau_{rz}}{\partial z}\mathrm{d}r - \frac{1}{r^2}\int_{r_0}^{r} r\sigma_z \mathrm{d}r - \frac{1}{2}\frac{1}{r^2}C_2 + C_4. \tag{20}$$

Constants C_2 and C_4 are determined from the boundary conditions.

Introducing expressions (16) into equations (19) and (20), stress components σ_r and σ_θ can be expressed as

$$\sigma_r^{'} = -\sum_{k=1}^{m}\frac{1}{2k}\overline{d}_{2k-1}\left(\rho^{2k} - \rho_0^{2k}\right) + \sum_{k=0}^{m}\frac{1}{2k+2}c_{2k}^{'}\left(\rho^{2k} - \rho_0^{2k}\right) + \frac{1}{2\rho^2}C_2^{'} + C_4^{'}, \tag{21}$$

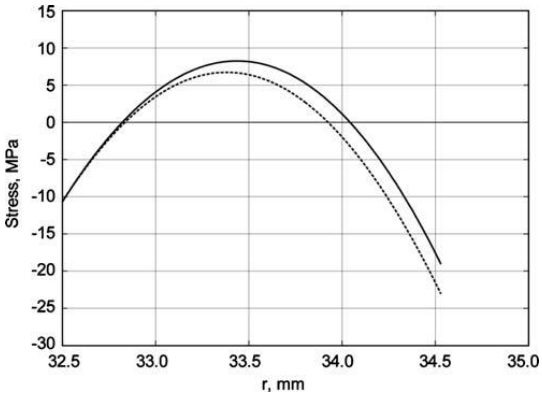

Fig. 11 Stresses σ_z (*continuous lines*) and σ_θ (*dashed lines*) in section 2, determined with the linear algorithm

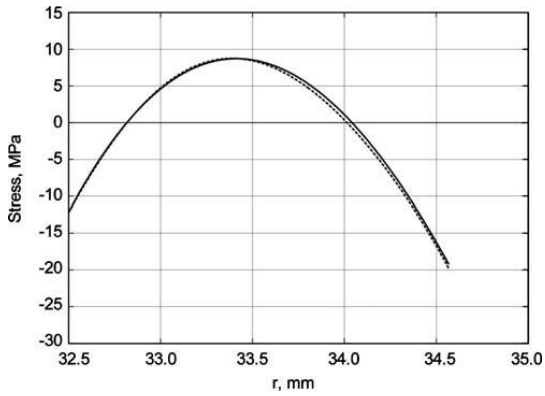

Fig. 12 Stresses σ_z (*continuous lines*) and σ_θ (*dashed lines*) in section 2, determined with the non-linear algorithm

$$\sigma_\theta^{'} = \sum_{k=0}^{m} c_{2k}^{'}\,\rho^{2k} - \sum_{k=1}^{m}\frac{1}{2k}\overline{d}_{2k-1}\left(\rho^{2k} - \rho_0^{2k}\right) - \sum_{k=0}^{m}\frac{1}{2k+2}c_{2k}^{'}\left(\rho^{2k} - \rho_0^{2k}\right) - \frac{1}{2\rho^2}C_2^{'} + C_4^{'}. \tag{22}$$

Here

$$\rho = \frac{r}{R}, \quad \rho_0 = \frac{r_0}{R}, \quad \overline{d}_{2k-1} = \frac{d_{2k-1}^{''} - d_{2k-1}^{'}}{\Delta z}R^{'}, \tag{23}$$

and R and R' are the external radiuses of sections 1 and 2. Similar expressions are valid for the stress components σ''_r and σ''_θ in section 2. Thus all the stress components in sections 1 and 2 can be expressed through the coefficients $c_{2k}^{'}, c_{2k}^{''}, d_{2k-1}^{'}$ and $d_{2k-1}^{''}$.

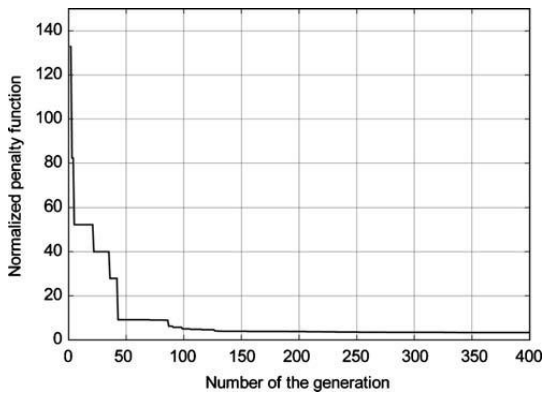

Fig. 13 Dependence of the penalty function on the number of generation in the DE process

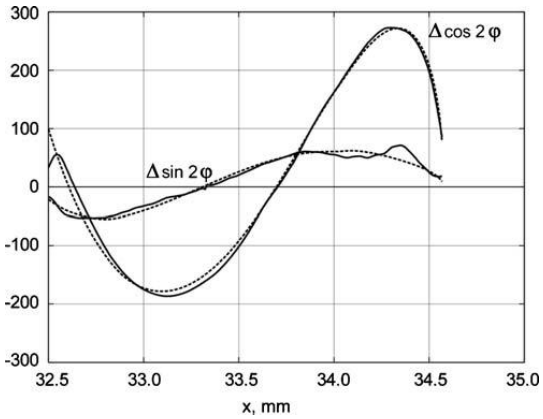

Fig. 14 Experimentally measured (*continuous lines*) and calculated (*dashed lines*), on the basis of the final stress distribution, data in section 2

The second equilibrium equation

$$\frac{\partial \sigma_z}{\partial z}+\frac{\partial \tau_{tz}}{\partial r}+\frac{1}{r}\tau_{rz}=0 \tag{24}$$

permits to eliminate coefficients c''_{2k}. Let us call the coefficients $c'_{2k}, c''_{2k}, d'_{2k-1}$ and d''_{2k-1} stress coefficients s_i (i=1, ..., l). They permit calculation of all the stress components. The set of the stress coefficients is named stress vector $\boldsymbol{S}$, which has l components.

The Differential Evolution Algorithm

Our aim is to find the stress vector, which corresponds best to the measurement data. For that we use the differential evolution (DE) algorithm [34]. Differential evolution is a parallel direct research method for finding optimum values of the components of a vector. The initial population of the vectors is chosen randomly if nothing is known about the system. In case a preliminary solution is available, the initial population can be generated by adding normally distributed random deviations to the nominal solution. The crucial idea behind DE is a scheme for generating trial vectors. DE generates new vectors by adding a weighted difference vector between two population members to a third member. If the resulting vector yields a lower objective function than a predetermined population member, the newly generated vector will replace in the following generation the vector, with which it was compared. The best vector is evaluated for every generation to keep track of the progress that is made during the minimization process. Extracting distance and direction information from the population to generate random deviations results in an adaptive scheme with excellent convergence properties.

For the determination of the stress vector $\boldsymbol{S}$, which corresponds best to the measurement data, the following method was used. First, the parameter of the isoclinic φ_i^m and optical retardation are measured in both sections 1 and 2 on n light rays. For every stress vector $\boldsymbol{S}$ it is possible to calculate for the same light rays i the parameters φ_i^c and Δ_i^c. For example, by modelling the test object on a light ray as a pile of birefringent plates, each of which is described by a Jones' vector [35]. The objective (penalty) function F

$$F=\frac{1}{n}\sum_{i=1}^{n}\left[\left(\frac{\Delta_i^c\cos 2\varphi_i^c-\Delta_i^m\cos 2\varphi_i^m}{\varepsilon}\right)^2+\left(\frac{\Delta_i^c\sin 2\varphi_i^c-\Delta_i^m\sin 2\varphi_i^m}{\varepsilon}\right)^2\right] \tag{25}$$

characterizes how well the stress vector describes the real stress field. Here ε is the measurement error. The penalty function F takes into account all the measurement data on the n light rays.

General algorithm of the method is shown in Fig. 5 and the algorithm of DE in Fig. 6.

In practical application of the algorithm we generated the initial population of 100 stress vectors by adding normally distributed random deviations to the solution of linear photoelastic tomography.

According to Fig. 5, on the basis of the measurement data and of the generated stress vectors, the penalty function F_j for every generated stress vector is calculated. Most important is the smallest penalty function of the population, min F_j. If F_j is sufficiently small, one may have obtained a satisfactory solution, i.e., a stress field that corresponds to the real measurement data well enough. If not, using the differential evolution algorithm, a new population of stress vectors is generated, penalty functions for this population are calculated, etc.

Figure 6 shows how stress vectors $D(d_1, d_2, ..., d_l)$ of the initial population are modified into stress vectors $E(e_1, e_2, ..., e_e)$ of the new generation, using other three stress vectors A, B, and C of the initial population.

Random crossing (Fig. 6) was carried out as follows:

$$e_i=\begin{cases} a_i+\ 0.8(b_i-c_i) & \text{if}\quad r<p,\\ d_i & \text{if}\quad r\geq p,\end{cases} \tag{26}$$

where r is a random number between 0 and 1 and p is a parameter, which can be chosen by the operator. We used p= 0.9, which has proved to be efficient in practical applications [34].

The algorithm, shown in Figs. 5 and 6, was programmed in C^{++}. Implemented on the computer IBM R50E, 400

iterations takes 20 min. With a cluster of computers this time can be shortened to several seconds.

Experiment

As an example, residual stresses near the rim in a rim-tempered drinking glass (Fig. 7) were investigated. In section 1 (z=28.1 mm) optical retardation is less than 100 nm and therefore equations (3) and (4) of the linear approximation are valid. Stresses in section 1 were determined with a linear algorithm of photoelastic tomography [16]. By approximating stresses, in equation (16) we used m=3. Thus the number of the coefficients of the stress vector was l=11. Figure 8 shows the measurement data as well as data that is calculated on the basis of obtained stress distribution, shown in Fig. 9. We see that experimentally measured and calculated data are very close. That indicates that in section 1 linear approximation of photoelastic tomography is valid. In section 1 we obtained $F(1)$=0.4.

In section 2 (z=16.8 mm) optical retardation reached 300 nm. In case of rotation of the principal stress axes that is somewhat more than allowed in linear photoelastic tomography, as mentioned before. Figure 10 shows measured data in section 2.

On the basis of the measurement data in section 2, stresses were calculated using the algorithm of linear photoelastic tomography [16] (Fig. 11). Using measured stresses, theoretical measurement data were calculated (Fig. 10). Figure 10 shows that the difference between measured and calculated data is much bigger than in section 1, especially for $\Delta\sin 2\varphi$. That is expressed also in the value of the penalty function: $F(2)$=59. It is an indication that in section 2 the linear approximation is not valid.

Using the DE method, final stress distribution in section 2 was obtained (Fig. 12). In comparison with Fig. 11 the change of σ_θ is remarkable. The decrease of the penalty function F during the DE procedure is shown in Fig. 13. After the 150*th* generation the penalty function remains about constant, $F\cong 3$.

In Fig. 12 practically $\sigma_\theta \cong \sigma_z$. That was to be expected. In a cylindrical object with weak stress gradient in z direction the classical sum rule

$$\sigma_r + \sigma_\theta = \sigma_z \tag{27}$$

is valid [17]. Since $\sigma_r \cong 0$, it follows from equation (27) that $\sigma_\theta \cong \sigma_z$.

Figure 14 shows a comparison of the experimentally measured and calculated, on the basis of the final stress distribution, data in section 2. Coincidence of the measured and calculated data is considerably better than that shown in Fig. 10, especially for the term $\Delta\sin 2\varphi$.

Conclusions

An algorithm of photoelastic tomography, which is free of limiting assumptions about the value of the birefringence or rotation of the principal stress axes, has been elaborated. Coefficients of the stress polynomials, which fit best the measurement data, are determined with the differential evolution method. Practical application of the method is illustrated by measuring residual stress near the rim of a rim-tempered drinking glass. It is important to underline that photoelastic measurements in the case of the non-linear algorithm of photoelastic tomography are exactly the same as in case of the linear algorithm. No additional measurements are needed.

Acknowledgements Support of the Estonian Science Foundation (grant no. 6881) is gratefully acknowledged. The authors thank Jelena Sanko for consultations concerning the differential evolution method.

References

1. Weller R (1939) A new method for photoelasticity in three dimensions. J Appl Phys 10:266.
2. Srinath LS (1983) Scattered light photoelasticity. Tata McGraw-Hill, New Delhi.
3. Kobayashi AS (ed) (1987) Handbook on experimental mechanics. Prentice-Hall, Englewood Cliffs.
4. Robert A, Guillemet E (1963) Nouvelle méthode d'utilisation de la lumière diffusée en photoélasticimétrie a trois dimensions. Rev Franç Méc 5/6:147–157.
5. Desally R, Lagarde A (1977) Rectilinear and circular analysis of a plane slice optically isolated in a three-dimensional photoelastic model. Mech Res Comm 4:99–107.
6. Bilek A, Brémand F, Dupré JC (2004) Studies of contact problems by 3D photoelasticity, comparison with finite element analysis. In: Proceedings of the 12th International Conference on Experimental Mechanics, pp 24–25, Bari, Italy.
7. Kihara T (2004) Photoelastic model measurement with rotated principal axes by scattered-light photoelasticity. Exp Mech 44:455–460.
8. Herman CT (1980) Image reconstruction from projections. Academic, New York.
9. Natterer F (1986) The mathematics of computerized tomography. Teubner, Stuttgart.
10. Proceedings of 1st World Congress on Industrial Process Tomography (1999), Buxton.
11. Sharafutdinov VA (1994) Integral geometry of tensor fields. VSP, Utrecht.
12. Aben H (1979) Integrated photoelasticity. McGraw-Hill, New York.
13. Sharafutdinov V (1989) On integrated photoelasticity in case of weak birefringence. Proc Est Acad Sci Phys Math 38:379–389.

14. Aben H, Idnurm S, Puro A (1990) Integrated photoelasticity in case of weak birefringence. In: Proceedings 9th International Conference on Experimental Mechanics, pp 867–875, Copenhagen.
15. Aben H, Idnurm S, Josepson J, Kell K-J, Puro A (1991) Optical tomography of the stress tensor field. In: Levin GG (ed) Analytical methods for optical tomography. Proc. SPIE 1843:220–229.
16. Aben H, Errapart A, Ainola L, Anton J (2005) Photoelastic tomography for residual stress measurement in glass. Opt Eng 44:1–8 (093601).
17. Aben H, Guillemet C (1993) Photoelasticity of glass. Springer, Berlin.
18. Aben HK, Josepson JI, Kell K-J (1989) The case of weak birefringence in integrated photoelasticity. Opt Lasers Eng 11:145–157.
19. Dash CJ (1992) One-dimensional tomography: a comparison of Abel, onion-peeling, and filtered backprojection methods. Appl Opt 31:1146–1152.
20. Doyle JF, Danyluk HT (1978) Integrated photoelasticity for axisymmetric problems. Exp Mech 18:156–220.
21. Schupp D (1999) Optische Tensortomographie zur Bestimmung räumlicher Spannungsverteilungen. Tech Mess 66:54–60.
22. Aben H, Errapart A, Ainola L (2006) On real and imaginary algorithms of optical tensor field tomography. Proc Est Acad Sci Phys Math 55:112–127.
23. Mangal SK, Ramesh K (1999) Determination of characteristic parameters in integrated photoelasticity by phase-shifting technique. Opt Lasers Eng 31:263–278.
24. Tomlinson R, Patterson EA (2002) The case of phase-stepping for the measurement of characteristic parameters in integrated photoelasticity. Exp Mech 42:43–50.
25. Aben H, Ainola L, Anton J (1999) Half-fringe phase-stepping with separation of the principal stress directions. Proc Est Acad Sci Eng 5:198–211.
26. Andirenko YA, Dubovikov MS (1994) Optical tomography of tensor fields. J Opt Soc Am A11:1628–1631.
27. Berezhna SYu, Berezhnyi IV, Vlokh OG (1994) Optical tomography of anisotropic inhomogeneous medium. In: Proceedings 10th Int Conf on Exp Mech, vol 1, pp 431–435, Lisboa, Portugal.
28. Wijerathne MLL, Oguni K, Hori M (2002) Tensor field tomography based on 3D photoelasticity. Mech Mater 34:535–545.
29. Puro AE (1996) On tomographic magnetophotoelasticity. Opt Spectrosc 81:119–125.
30. Wijerathne MLL, Oguni K, Hori M (2004) Inverse analysis method for photoelastic measurement of 3D stress state. Key Eng Mater 261(2):753–758.
31. Aben H, Ainola L, Puro A (1996) Photoelastic residual stress measurement in glass articles as a problem of hybrid mechanics. In: Proceedings 17th Symposium on Exp Mech of Solids, pp 1–10, Jachranka, Poland.
32. Ainola L, Aben H (2000) Hybrid mechanics for axisymmetric thermoelasticity problems. J Therm Stress 23:685–697.
33. Ainola L, Aben H (2004) A new relationship for the experimental–analytical solution of the axisymmetric thermoelasticity problem. ZAMM 84:211–215.
34. Price KV, Storn RM, Lampinen JA (2005) Differential evolution, a practical approach to global optimisation. Springer, Berlin.
35. Theocaris PS, Gdoutos EE (1979) Matrix theory of photoelasticity. Springer, Berlin.

Appendix 2: CV

Curriculum Vitae

1. Personal data

Name	Andrei Errapart
Date and place of birth	14th of March, 1978, Rakvere
Nationality	Estonian

2. Contact information

Adress	Õle 35, 10319 Tallinn
Telephone	+372 56 692 469
E-mail	andrei@errapart.com

3. Education

Educational institution	Graduation year	Education (field of study/degree)
Tallinn University of Technology	2007	Engineering physics, MSc
Tallinn University of Technology	2002	Engineering physics, BSc

4. Language competence/skills (fluent; average, basic skills)

Language	Level
Estonian	native
English	fluent

5. Professional employment

Period	Organization	Position
2008 - ...	Institute of Cybernetics at TUT	researcher
2006 - 2008	Institute of Cybernetics at TUT	engineer-technician
2000 - 2005	Institute of Cybernetics at TUT	technician
1998 - 1999	Tradenet Ltd	computer programmer

6. Scientific work

35 published papers. Handling of practice sessions in twelve annual Glass Stress Summer Schools. Lectures of photoelastic tomography in the University of Shiga Prefecture and Nippon Electric Glass Company in Japan.

7. Defended thesis

2007, Technology of photoelastic tomography, Msc, supervisor prof. Hillar Aben, Tallinn University of Technology, Faculty of Science

8. Main areas of scientific work/Current research topics

Photoelastic tomography for the determination of 3D stress fields.

9. Honours and awards

2009, Hillar Aben, Leo Ainola, Johan Anton, Andrei Errapart; Estonian National Award for the outstanding research and development leading to an innovative product: Research and development of the theory, measurement methodology and equipment of integrated photoelasticity and application for the measurement of residual stresses in the glass industry

Elulookirjeldus

1. Isikuandmed

Nimi	Andrei Errapart
Sünniaeg ja -koht	14. märts 1978, Rakvere
Kodakondsus	Eesti

2. Kontaktandmed

Aadress	Õle 35, 10319 Tallinn
Telefon	+372 56 692 469
E-post	andrei@errapart.com

3. Hariduskäik

Õppeasutus (nimetus lõpetamise ajal)	Lõpetamise aeg	Haridus (eriala/kraad)
Tallinna Tehnikaülikool	2007	tehniline füüsika, MSc
Tallinna Tehnikaülikool	2002	tehniline füüsika, BSc

4. Keelteoskus (alg-, kesk- või kõrgtase)

Keel	Tase
Eesti keel	emakeel
Inglise keel	kõrgtase

5. Teenistuskäik

Töötamise aeg	Tööandja nimetus	Ametikoht
2008 - ...	TTÜ Küberneetika Instituut	teadur
2006 - 2008	TTÜ Küberneetika Instituut	insener-tehnik
2000 - 2005	TTÜ Küberneetika Instituut	tehnik
1998 - 1999	AS Tradenet	arvutiprogrammeerija

6. Teadustegevus

35 avaldatud artiklit. Kaheteistkümne iga-aastase klaasipingete suvekooli (Glass Stress Summer School) praktikumi läbiviimine. Loengud fotoelastsustomograafiast Shiga Prefektuuri Ülikoolis ja Nippon Electric Glass Company’s Jaapanis.

7. Kaitstud lõputööd

2007, Fotoelastsustomograafia tehnoloogia, MSc, juhendaja DSc. Hillar Aben, Tallinna Tehnikaülikool

8. Teadustöö põhisuunad

Kolmemõõtmeliste pingeväljade määramine fotoelastsustomograafia abil.

9. Autasud

2009, Hillar Aben, Leo Ainola, Johan Anton, Andrei Errapart; Riiklik teaduspremia innovaatilise tooteni viinud väljapaistva teadus- ja arendustöö eest: Integraalse fotoelastsusmeetodi teooria, mõõtmistehnoloogia ja aparatuuri väljatöötamine ja rakendamine jääkpingete mõõtmisel klaasitööstuses

DISSERTATIONS DEFENDED AT TALLINN UNIVERSITY OF TECHNOLOGY ON *NATURAL AND EXACT SCIENCES*

1. **Olav Kongas**. Nonlinear Dynamics in Modeling Cardiac Arrhytmias. 1998.

2. **Kalju Vanatalu**. Optimization of Processes of Microbial Biosynthesis of Isotopically Labeled Biomolecules and Their Complexes. 1999.

3. **Ahto Buldas**. An Algebraic Approach to the Structure of Graphs. 1999.

4. **Monika Drews**. A Metabolic Study of Insect Cells in Batch and Continuous Culture: Application of Chemostat and Turbidostat to the Production of Recombinant Proteins. 1999.

5. **Eola Valdre**. Endothelial-Specific Regulation of Vessel Formation: Role of Receptor Tyrosine Kinases. 2000.

6. **Kalju Lott**. Doping and Defect Thermodynamic Equilibrium in ZnS. 2000.

7. **Reet Koljak**. Novel Fatty Acid Dioxygenases from the Corals *Plexaura homomalla* and *Gersemia fruticosa.* 2001.

8. **Anne Paju**. Asymmetric oxidation of Prochiral and Racemic Ketones by Using Sharpless Catalyst. 2001.

9. **Marko Vendelin**. Cardiac Mechanoenergetics *in silico*. 2001.

10. **Pearu Peterson**. Multi-Soliton Interactions and the Inverse Problem of Wave Crest. 2001.

11. **Anne Menert**. Microcalorimetry of Anaerobic Digestion. 2001.

12. **Toomas Tiivel**. The Role of the Mitochondrial Outer Membrane in *in vivo* Regulation of Respiration in Normal Heart and Skeletal Muscle Cell. 2002.

13. **Olle Hints**. Ordovician Scolecodonts of Estonia and Neighbouring Areas: Taxonomy, Distribution, Palaeoecology, and Application. 2002.

14. **Jaak Nõlvak**. Chitinozoan Biostratigrapy in the Ordovician of Baltoscandia. 2002.

15. **Liivi Kluge**. On Algebraic Structure of Pre-Operad. 2002.

16. **Jaanus Lass**. Biosignal Interpretation: Study of Cardiac Arrhytmias and Electromagnetic Field Effects on Human Nervous System. 2002.

17. **Janek Peterson**. Synthesis, Structural Characterization and Modification of PAMAM Dendrimers. 2002.

18. **Merike Vaher**. Room Temperature Ionic Liquids as Background Electrolyte Additives in Capillary Electrophoresis. 2002.

19. **Valdek Mikli**. Electron Microscopy and Image Analysis Study of Powdered Hardmetal Materials and Optoelectronic Thin Films. 2003.

20. **Mart Viljus**. The Microstructure and Properties of Fine-Grained Cermets. 2003.

21. **Signe Kask**. Identification and Characterization of Dairy-Related *Lactobacillus.* 2003

22. **Tiiu-Mai Laht**. Influence of Microstructure of the Curd on Enzymatic and Microbiological Processes in Swiss-Type Cheese. 2003.

23. **Anne Kuusksalu**. 2–5A Synthetase in the Marine Sponge *Geodia cydonium*. 2003.

24. **Sergei Bereznev**. Solar Cells Based on Polycristalline Copper-Indium Chalcogenides and Conductive Polymers. 2003.

25. **Kadri Kriis**. Asymmetric Synthesis of C_2-Symmetric Bimorpholines and Their Application as Chiral Ligands in the Transfer Hydrogenation of Aromatic Ketones. 2004.

26. **Jekaterina Reut**. Polypyrrole Coatings on Conducting and Insulating Substracts. 2004.

27. **Sven Nõmm**. Realization and Identification of Discrete-Time Nonlinear Systems. 2004.

28. **Olga Kijatkina**. Deposition of Copper Indium Disulphide Films by Chemical Spray Pyrolysis. 2004.

29. **Gert Tamberg**. On Sampling Operators Defined by Rogosinski, Hann and Blackman Windows. 2004.

30. **Monika Übner**. Interaction of Humic Substances with Metal Cations. 2004.

31. **Kaarel Adamberg**. Growth Characteristics of Non-Starter Lactic Acid Bacteria from Cheese. 2004.

32. **Imre Vallikivi**. Lipase-Catalysed Reactions of Prostaglandins. 2004.

33. **Merike Peld**. Substituted Apatites as Sorbents for Heavy Metals. 2005.

34. **Vitali Syritski**. Study of Synthesis and Redox Switching of Polypyrrole and Poly(3,4-ethylenedioxythiophene) by Using *in-situ* Techniques. 2004.

35. **Lee Põllumaa**. Evaluation of Ecotoxicological Effects Related to Oil Shale Industry. 2004.

36. **Riina Aav**. Synthesis of 9,11-Secosterols Intermediates. 2005.

37. **Andres Braunbrück**. Wave Interaction in Weakly Inhomogeneous Materials. 2005.

38. **Robert Kitt**. Generalised Scale-Invariance in Financial Time Series. 2005.

39. **Juss Pavelson**. Mesoscale Physical Processes and the Related Impact on the Summer Nutrient Fields and Phytoplankton Blooms in the Western Gulf of Finland. 2005.

40. **Olari Ilison**. Solitons and Solitary Waves in Media with Higher Order Dispersive and Nonlinear Effects. 2005.

41. **Maksim Säkki**. Intermittency and Long-Range Structurization of Heart Rate. 2005.

42. **Enli Kiipli**. Modelling Seawater Chemistry of the East Baltic Basin in the Late Ordovician–Early Silurian. 2005.

43. **Igor Golovtsov**. Modification of Conductive Properties and Processability of Polyparaphenylene, Polypyrrole and polyaniline. 2005.

44. **Katrin Laos**. Interaction Between Furcellaran and the Globular Proteins (Bovine Serum Albumin β-Lactoglobulin). 2005.

45. **Arvo Mere**. Structural and Electrical Properties of Spray Deposited Copper Indium Disulphide Films for Solar Cells. 2006.

46. **Sille Ehala**. Development and Application of Various On- and Off-Line Analytical Methods for the Analysis of Bioactive Compounds. 2006.

47. **Maria Kulp**. Capillary Electrophoretic Monitoring of Biochemical Reaction Kinetics. 2006.

48. **Anu Aaspõllu.** Proteinases from *Vipera lebetina* Snake Venom Affecting Hemostasis. 2006.

49. **Lyudmila Chekulayeva**. Photosensitized Inactivation of Tumor Cells by Porphyrins and Chlorins. 2006.

50. **Merle Uudsemaa**. Quantum-Chemical Modeling of Solvated First Row Transition Metal Ions. 2006.

51. **Tagli Pitsi**. Nutrition Situation of Pre-School Children in Estonia from 1995 to 2004. 2006.

52. **Angela Ivask**. Luminescent Recombinant Sensor Bacteria for the Analysis of Bioavailable Heavy Metals. 2006.

53. **Tiina Lõugas**. Study on Physico-Chemical Properties and Some Bioactive Compounds of Sea Buckthorn (*Hippophae rhamnoides* L.). 2006.

54. **Kaja Kasemets**. Effect of Changing Environmental Conditions on the Fermentative Growth of *Saccharomyces cerevisae* S288C: Auxo-accelerostat Study. 2006.

55. **Ildar Nisamedtinov**. Application of ^{13}C and Fluorescence Labeling in Metabolic Studies of *Saccharomyces* spp. 2006.

56. **Alar Leibak**. On Additive Generalisation of Voronoï's Theory of Perfect Forms over Algebraic Number Fields. 2006.

57. **Andri Jagomägi**. Photoluminescence of Chalcopyrite Tellurides. 2006.

58. **Tõnu Martma**. Application of Carbon Isotopes to the Study of the Ordovician and Silurian of the Baltic. 2006.

59. **Marit Kauk**. Chemical Composition of $CuInSe_2$ Monograin Powders for Solar Cell Application. 2006.

60. **Julia Kois**. Electrochemical Deposition of $CuInSe_2$ Thin Films for Photovoltaic Applications. 2006.

61. **Ilona Oja Açik**. Sol-Gel Deposition of Titanium Dioxide Films. 2007.

62. **Tiia Anmann**. Integrated and Organized Cellular Bioenergetic Systems in Heart and Brain. 2007.

63. **Katrin Trummal**. Purification, Characterization and Specificity Studies of Metalloproteinases from *Vipera lebetina* Snake Venom. 2007.

64. **Gennadi Lessin**. Biochemical Definition of Coastal Zone Using Numerical Modeling and Measurement Data. 2007.

65. **Enno Pais**. Inverse problems to determine non-homogeneous degenerate memory kernels in heat flow. 2007.

66. **Maria Borissova**. Capillary Electrophoresis on Alkylimidazolium Salts. 2007.

67. **Karin Valmsen**. Prostaglandin Synthesis in the Coral *Plexaura homomalla*: Control of Prostaglandin Stereochemistry at Carbon 15 by Cyclooxygenases. 2007.

68. **Kristjan Piirimäe**. Long-Term Changes of Nutrient Fluxes in the Drainage Basin of the Gulf of Finland – Application of the PolFlow Model. 2007.

69. **Tatjana Dedova**. Chemical Spray Pyrolysis Deposition of Zinc Sulfide Thin Films and Zinc Oxide Nanostructured Layers. 2007.

70. **Katrin Tomson**. Production of Labelled Recombinant Proteins in Fed-Batch Systems in *Escherichia coli*. 2007.

71. **Cecilia Sarmiento**. Suppressors of RNA Silencing in Plants. 2008.

72. **Vilja Mardla**. Inhibition of Platelet Aggregation with Combination of Antiplatelet Agents. 2008.

73. **Maie Bachmann**. Effect of Modulated Microwave Radiation on Human Resting Electroencephalographic Signal. 2008.

74. **Dan Hüvonen**. Terahertz Spectroscopy of Low-Dimensional Spin Systems. 2008.

75. **Ly Villo**. Stereoselective Chemoenzymatic Synthesis of Deoxy Sugar Esters Involving *Candida antarctica* Lipase B. 2008.

76. **Johan Anton**. Technology of Integrated Photoelasticity for Residual Stress Measurement in Glass Articles of Axisymmetric Shape. 2008.

77. **Olga Volobujeva**. SEM Study of Selenization of Different Thin Metallic Films. 2008.

78. **Artur Jõgi**. Synthesis of 4'-Substituted 2,3'-dideoxynucleoside Analogues. 2008.

79. **Mario Kadastik**. Doubly Charged Higgs Boson Decays and Implications on Neutrino Physics. 2008.

80. **Fernando Pérez-Caballero**. Carbon Aerogels from 5-Methylresorcinol-Formaldehyde Gels. 2008.

81. **Sirje Vaask**. The Comparability, Reproducibility and Validity of Estonian Food Consumption Surveys. 2008.

82. **Anna Menaker**. Electrosynthesized Conducting Polymers, Polypyrrole and Poly(3,4-ethylenedioxythiophene), for Molecular Imprinting. 2009.

83. **Lauri Ilison**. Solitons and Solitary Waves in Hierarchical Korteweg-de Vries Type Systems. 2009.

84. **Kaia Ernits**. Study of In_2S_3 and ZnS Thin Films Deposited by Ultrasonic Spray Pyrolysis and Chemical Deposition. 2009.

85. **Veljo Sinivee**. Portable Spectrometer for Ionizing Radiation "Gammamapper". 2009.

86. **Jüri Virkepu**. On Lagrange Formalism for Lie Theory and Operadic Harmonic Oscillator in Low Dimensions. 2009.

87. **Marko Piirsoo**. Deciphering Molecular Basis of Schwann Cell Development. 2009.

88. **Kati Helmja**. Determination of Phenolic Compounds and Their Antioxidative Capability in Plant Extracts. 2010.

89. **Merike Sõmera**. Sobemoviruses: Genomic Organization, Potential for Recombination and Necessity of P1 in Systemic Infection. 2010.

90. **Kristjan Laes**. Preparation and Impedance Spectroscopy of Hybrid Structures Based on $CuIn_3Se_5$ Photoabsorber. 2010.

91. **Kristin Lippur**. Asymmetric Synthesis of 2,2'-Bimorpholine and its 5,5'-Substituted Derivatives. 2010.

92. **Merike Luman**. Dialysis Dose and Nutrition Assessment by an Optical Method. 2010.

93. **Mihhail Berezovski**. Numerical Simulation of Wave Propagation in Heterogeneous and Microstructured Materials. 2010.

94. **Tamara Aid-Pavlidis**. Structure and Regulation of BDNF Gene. 2010.

95. **Olga Bragina**. The Role of Sonic Hedgehog Pathway in Neuro- and Tumorigenesis. 2010.

96. **Merle Randrüüt**. Wave Propagation in Microstructured Solids: Solitary and Periodic Waves. 2010.

97. **Marju Laars**. Asymmetric Organocatalytic Michael and Aldol Reactions Mediated by Cyclic Amines. 2010.

98. **Maarja Grossberg**. Optical Properties of Multinary Semiconductor Compounds for Photovoltaic Applications. 2010.

99. **Alla Maloverjan**. Vertebrate Homologues of Drosophila Fused Kinase and Their Role in Sonic Hedgehog Signalling Pathway. 2010.

100. **Priit Pruunsild**. Neuronal Activity-Dependent Transcription Factors and Regulation of Human *BDNF* Gene. 2010.

101. **Tatjana Knjazeva**. New Approaches in Capillary Electrophoresis for Separation and Study of Proteins. 2011.

102. **Atanas Katerski**. Chemical Composition of Sprayed Copper Indium Disulfide Films for Nanostructured Solar Cells. 2011.

103. **Kristi Timmo.** Formation of Properties of $CuInSe_2$ and $Cu_2ZnSn(S,Se)_4$ Monograin Powders Synthesized in Molten KI. 2011.

104. **Kert Tamm**. Wave Propagation and Interaction in Mindlin-Type Microstructured Solids: Numerical Simulation. 2011.

105. **Adrian Popp**. Ordovician Proetid Trilobites in Baltoscandia and Germany. 2011.

106. **Ove Pärn**. Sea Ice Deformation Events in the Gulf of Finland and This Impact on Shipping. 2011.

107. **Germo Väli**. Numerical Experiments on Matter Transport in the Baltic Sea. 2011.

108. **Andrus Seiman**. Point-of-Care Analyser Based on Capillary Electrophoresis. 2011.

109. **Olga Katargina**. Tick-Borne Pathogens Circulating in Estonia (Tick-Borne Encephalitis Virus, *Anaplasma phagocytophilum*, *Babesia* Species): Their Prevalence and Genetic Characterization. 2011.
110. **Ingrid Sumeri**. The Study of Probiotic Bacteria in Human Gastrointestinal Tract Simulator. 2011.
111. **Kairit Zovo**. Functional Characterization of Cellular Copper Proteome. 2011.
112. **Natalja Makarytsheva**. Analysis of Organic Species in Sediments and Soil by High Performance Separation Methods. 2011.
113. **Monika Mortimer**. Evaluation of the Biological Effects of Engineered Nanoparticles on Unicellular Pro- and Eukaryotic Organisms. 2011.
114. **Kersti Tepp**. Molecular System Bioenergetics of Cardiac Cells: Quantitative Analysis of Structure-Function Relationship. 2011.
115. **Anna-Liisa Peikolainen**. Organic Aerogels Based on 5-Methylresorcinol. 2011.
116. **Leeli Amon**. Palaeoecological Reconstruction of Late-Glacial Vegetation Dynamics in Eastern Baltic Area: A View Based on Plant Macrofossil Analysis. 2011.
117. **Tanel Peets**. Dispersion Analysis of Wave Motion in Microstructured Solids. 2011.
118. **Liina Kaupmees**. Selenization of Molybdenum as Contact Material in Solar Cells. 2011.
119. **Allan Olspert**. Properties of VPg and Coat Protein of Sobemoviruses. 2011.
120. **Kadri Koppel**. Food Category Appraisal Using Sensory Methods. 2011.
121. **Jelena Gorbatšova**. Development of Methods for CE Analysis of Plant Phenolics and Vitamins. 2011.
122. **Karin Viipsi**. Impact of EDTA and Humic Substances on the Removal of Cd and Zn from Aqueous Solutions by Apatite. 2012.
123. **David Schryer**. Metabolic Flux Analysis of Compartmentalized Systems Using Dynamic Isotopologue Modeling. 2012.
124. **Ardo Illaste**. Analysis of Molecular Movements in Cardiac Myocytes. 2012.
125. **Indrek Reile**. 3-Alkylcyclopentane-1,2-Diones in Asymmetric Oxidation and Alkylation Reactions. 2012.
126. **Tatjana Tamberg**. Some Classes of Finite 2-Groups and Their Endomorphism Semigroups. 2012.
127. **Taavi Liblik**. Variability of Thermohaline Structure in the Gulf of Finland in Summer. 2012.
128. **Priidik Lagemaa**. Operational Forecasting in Estonian Marine Waters. 2012.